

**Investigation of Novel Nanoscale Materials, Methods and Instrumentation for
Sensing Applications**

BY

SOUVIK MUKHERJEE

B.Tech., West Bengal University of Technology, Kolkata, 2012.

THESIS

Submitted as partial fulfillment of the requirements
for the degree of Doctor of Philosophy in Electrical and Computer Engineering
in the Graduate College of the
University of Illinois at Chicago, 2018

Chicago, Illinois

Defense Committee:

Mitra Dutta, Chair and Advisor
Michael A. Strosio
Vitali Metlushko
Alan Nicholls, Research Resource Center, UIC
Sasan Bakhtiari, Nuclear Engineering Division, ANL

To my sister Soumíta and my parents, Mrs. Sumíta Mukherjee and Mr. Jagabandhu Mukherjee.

ACKNOWLEDGEMENTS

First and foremost, I would like to thank my advisor Dr. Mitra Dutta for everything. She provided me the opportunity to work in the Nano Engineering Research Group at UIC and her mentorship helped me to grow as an independent researcher over the years. Dr. Dutta introduced me to the area of experimental solid-state device physics and provided me with all the necessary tools and motivation to conduct research in related areas. I am thankful to Dr. Michael A. Stroscio for sharing his profound knowledge on nanoscale semiconductor device physics and bioelectronics. The work conducted at the Nuclear Engineering division at Argonne National Laboratory would not have been possible without the guidance and help from Dr. Sasan Bakhtiari, Dr. Ryan R. Ahern and Dr. Nachappa Gopalsami and Mr. Eugene R. Koehl. I would like to thank Dr. Bakhtiari for allowing me to work in the Sensors and Instrumentation laboratory and introducing me to various state-of-the-art millimeter wave technologies. I would like to thank Dr. Alan Nicholls, Ms. Olivia Thomson and Dr. Fengyuan Shi of the Research Resource Center at UIC for their help with the acquisition and analysis of SEM, TEM, EDX and XPS data. I would also like to thank Dr. Vitali Metlushko for serving on my defense committee and providing helpful comments on my dissertation.

It was a great pleasure to work with Mr. Thomas W. Elmer at Argonne National Laboratory who introduced me to Matlab and LabVIEW and helped with data acquisition and processing. I would like to thank him for sharing his technical expertise on scientific computing and being such a great friend and role model. I would like to thank Mr. Richard L. Cadogan and Mr. Gerald A. Letizia for their help during the ^{137}Cs irradiation test. I would like to thank Dr. Gary P. Wiederrecht, Dr. Richard D. Schaller, Dr. David J.

ACKNOWLEDGEMENTS (continued)

Gosztola for introducing me to ultrafast time-resolved spectroscopy and allowing me to work in the Center for Nanoscale Materials facility at Argonne National Laboratory. My research accomplishments wouldn't have been possible without the tremendous support from my fellow group members Debopam Datta, Ketaki Sarkar, Sidra Farid, Xenia Meshik, Min Choi, Shripriya Poduri and Mojgan Mazouchi. I am thankful to Sidra for our collaborations on CdTe, ZnO and graphene-FET sensor projects and for introducing me to various optical characterization tools during early days of my research career. Over the years, Ketaki has become an amazing friend and I would like to thank Ketaki for sharing her knowledge on electrical characterization of nanostructure devices and for our ongoing collaborative work on In₂O₃ and ZnO based nanostructures. From the starting days at UIC, Debopam and I have become very close friends, roommates as well as colleagues and I am thankful to him for all the wonderful time we have spent together. I would also like to thank Ching-en, Alvin, Tania, Jennifer, Agniva, Aritra, Arpan, Ritish, Sarasij, Ratul, Chirag, Amrita, Arindam, Subhankar and Debasish for making my stay in Chicago more eventful and fun.

I am forever indebted to my parents who has supported me with everything they had. A special thanks to my extended family members especially Arnab, Kuntal, Subhankar, Anirban, Jyotishman, Neel, Soumyarka and my childhood friend Rhicheek for being there whenever I needed them the most.

SM

CONTRIBUTION OF AUTHORS

All the chapters of this dissertation are adapted from my own published manuscripts as well as from unpublished work. The contributions of all the co-authors are listed below.

Author contributions in chapter 1: The work was conducted in collaboration with University of California, Irvine under the supervision of Dr. Mitra Dutta, Dr. Michael A. Stroschio and Dr. Peter Burke. Mr. Souvik Mukherjee conducted experiments and wrote the manuscript. Dr. Xenia Meshik, Dr. Min Choi and Dr. Sidra Farid helped with data acquisition. All other co-authors participated in discussions and provided helpful comments.

Author contributions in chapter 2 and 3: The work was conducted in collaboration with the Center for Nanoscale Materials of Argonne National Laboratory under the supervision of Dr. Mitra Dutta. Dr. Michael A. Stroschio provided helpful technical insights. Experiments conducted at Argonne National Laboratory was supervised by Dr. Gary P. Wiederrecht, Dr. Richard D. Schaller and Dr. David J. Gosztola. Mr. Souvik Mukherjee conducted experiments and wrote the manuscripts. Dr. Ketaki Sarkar helped with sample preparation and discussions.

Author contributions in chapter 4 and 5: The work was conducted in collaboration with the Nuclear Engineering Division of Argonne National Laboratory under the supervision of Dr. Mitra Dutta and Dr. Sasan Bakhtiari. Dr. Michael A. Stroschio and Dr. Nachappa Gopalsami provided helpful technical insights. Mr. Souvik Mukherjee conducted experiments and wrote the manuscripts. Dr. Ketaki Sarkar and Mr. Eugene R. Koehl helped with sample preparation and discussions. Mr. Thomas W. Elmer helped with data acquisition and analysis.

TABLE OF CONTENTS

<u>CHAPTER</u>	<u>PAGE</u>
1. INTRODUCTION	1
1.1. Nanoscale chemical sensors	1
1.1.1. Metal oxide semiconductor nanowires: choice of In_2O_3 nanowires as sensor material	3
1.2. Real-time detection and monitoring of CBRNE signatures – intended applications and underlying challenges	4
1.3. Overview of detection concepts	5
1.3.1. Millimeter wave stand-off detection of ionizing radiation by probing radiation interaction with sensor material	5
1.3.2. Millimeter wave spectroscopic detection of gas phase compounds	7
1.4. Dissertation outline	10
2. METAL OXIDE SEMIDONDUCTORS: INVESTIGATION OF GROWTH MECHANISM AND MORPHOLOGICAL DEFECTS OF In_2O_3 NANOWIRES	12
2.1. Growth of In_2O_3 nanowires	12
2.1.1. Experimental details.....	16
2.1.2. Influence of synthesis process parameters on the nanostructure morphology	19
2.2. Structural and compositional characterization	23
2.2.1. Analysis on the crystal quality of the as-synthesized nanowires using Raman spectroscopy	24
2.2.2. Nanowire surface modification through faceting and chemisorption.....	27
2.3. Conclusion.....	30
3. DEFECT CHARACTERIZATION USING OPTICAL TECHNIQUES AND INFLUENCE OF PASSIVATION TREATMENT ON In_2O_3 NANOWIRE PROPERTIES	32
3.1. Defects in In_2O_3	33
3.1.1. Identification of nature and position of the defect levels due to surface states using photoluminescence spectroscopy	36
3.1.2. First observation of near-band-edge photoluminescence broadening due to heavy doping.....	40
3.1.3. Ultrafast pump-probe spectroscopy to study the carrier trapping rates due to surface states	43
3.2. Effect of passivation treatment on the nanowire properties	52
3.2.1. Comparison of nanowire structural and luminescence properties post thermal annealing treatment.....	53
3.2.2. Modification of nanowire surface properties post thermal annealing treatment	56
3.3. Conclusion.....	57

TABLE OF CONTENTS (continued)

<u>CHAPTER</u>	<u>PAGE</u>
4. MILLIMETER WAVE STANDOFF MEASUREMENTS OF IONIZING RADIATION IN REAL-TIME USING In_2O_3 NANOWIRES AS SENSOR MATERIAL	59
4.1. Background	60
4.1.1. Microwave and millimeter wave scattering due to radiation induced air ionization.....	62
4.1.2. Interaction of γ -radiation with semiconductor material.....	64
4.2. Experimental setup.....	65
4.2.1. Compact continuous wave homodyne 94 GHz transceiver design for standoff detection.....	65
4.2.2. COMSOL modeling of lens antenna for targeted detection	68
4.3. Experimental observation.....	69
4.3.1. Preliminary investigation using a negative ion generator source – diffusion charging of nanowire surface.....	69
4.3.2. Application of In_2O_3 nanowires for stand-off detection of ^{137}Cs γ -radiation source	77
4.4. Conclusion	80
5. DEVELOPMENT OF FAST SWEEP CHIRPED-PULSE FOURIER TRANSFORM MILLIMETER WAVE SPECTROMETER FOR BROADBAND CHEMICAL SENSING IN REAL-TIME.....	82
5.1. Background on the chirped-pulse Fourier transform technique.....	84
5.2. Design and operation of a prototype 110-140 GHz broadband spectrometer....	88
5.2.1. Chirped pulse excitation source	90
5.2.2. Receiver	91
5.2.3. Gas Cell.....	91
5.3. Preliminary experimental observations.....	92
5.3.1. Demonstration of spectrometer accuracy using marker chemical	94
5.3.2. Analysis of a gaseous mixture – detection of various isotopologues of acetonitrile.....	96
5.4. Conclusion.....	100
6. CONCLUSIONS AND FUTURE WORK.....	102
6.1. Conclusion.....	102
6.2. Future work	105
CITED LITERATURE	108
APPENDICES	120
APPENDIX: A.....	121
APPENDIX: B.....	122

TABLE OF CONTENTS (continued)

<u>CHAPTER</u>	<u>PAGE</u>
VITA.....	130

LIST OF TABLES

<u>TABLE</u>		<u>PAGE</u>
I.	CHARACTERISTICS OF PHONON MODES IN In_2O_3 NANOWIRES BEFORE AND AFTER THERMAL ANNEALING TREATMENT SHOWING DISTINCT INCREASE IN THE PEAK INTENSITY AS WELL AS REDUCED BROADENING POST TREATMENT.	51
II.	EXTRACTED CARRIER RELAXATION TIME CONSTANTS AND RELATIVE AMPLITUDES FROM THE FITTED DATA OF AS-SYNTHESIZED AND ANNEALED SAMPLES AT 700 NM PROBE WAVELENGTH AND $300 \mu\text{W}$ PUMP POWER. THE AMPLITUDE OF THE FAST DECAY COMPONENT REDUCES SIGNIFICANTLY POST THERMAL ANNEALING TREATMENT THEREBY CONFIRMING SIGNIFICANT REDUCTION IN THE TRAP CENTERS. FURTHER THE LONG DECAY COMPONENT ASSOCIATED WITH CARRIER RECOMBINATION IS FOUND TO BE DRASTICALLY INCREASED DUE TO HIGH DENSITY OF ADSORBED OXYGEN SPECIES ON THE SURFACE CREATING A STRONG SURFACE DIPOLE.	56

LIST OF FIGURES

<u>FIGURE</u>	<u>PAGE</u>
1. Schematic representation of liquid gated FET-like aptamer-based nano biosensor with a single layer of graphene deposited on a polydimethylsiloxane (PDMS) substrate acting as the conducting channel; silver paste serves as contacts for both source and drain. Inset showing the immobilized aptamers with a 5' pyrene modification attached to the graphene layer via π - π stacking undergoing conformational change upon addition of ATP [10].	2
2. Schematic representation of a millimeter wave system to detect ionizing radiation effects by interrogating sensor tags deployed in the vicinity of the source.	6
3. Atmospheric EM opacity, Courtesy: National Aeronautics and Space Administration (NASA).....	8
4. Schematic illustration of the chemical vapor deposition (CVD) process for the growth of In_2O_3 nanowires.....	13
5. Schematic illustration of the Au-catalytic and self-catalytic VLS method resulting in the growth of In_2O_3 nanostructures under varied deposition zone temperatures.	14
6. (a) Low resolution FESEM image of dense mesh of In_2O_3 nanowires grown on Si substrate using carbothermal reduction process and VLS technique (b) corresponding high resolution image of a single nanowires with an average diameter of 100 nm (c) shows low resolution image of In_2O_3 nanoparticles with octahedron like morphologies grown using In metal source as the precursor on Si substrate (d) corresponding high resolution image of the substrate background showing the presence of truncated nanowire like features.	16
7. Low resolution SEM images of (a) perfect octahedrons and (b) truncated octahedrons like structures, inset in (a) and (b) shows corresponding computed Wulff shapes where the planes (110), (100) and (111) are represented with colors yellow, purple and cyan respectively.....	18
8. (a) Energy-dispersive X-ray (EDX) mapping of In_2O_3 nanoparticle sample and (b) wide area EDX profile of the background labelled as '1' in the inset which clearly shows the evidence of Au catalyst thereby confirming the growth of truncated nanowire features following the VLS route.....	20
9. (a) TEM image of a single In_2O_3 nanowire, inset shows surface roughness. (b), (c) HRTEM image and SAED pattern of In_2O_3 nanowires which reveals growth along [100] direction and single crystalline properties with cubic crystal structure. (d)	

LIST OF FIGURES (continued)

EDX spectrum shows elemental constituents at and below the tip of the nanowire.	22
10. (a) Low resolution TEM image of In_2O_3 nanoparticles (b), (c) HRTEM image and SAED pattern of In_2O_3 particles which reveals presence single crystalline properties with cubic crystal structure. (d) EDX spectrum shows elemental constituents at the tip of the nanoparticle which shows no evidence of Au catalyst.	24
11. (a) Room temperature non-resonant Raman spectra of In_2O_3 nanowires showing significant broadening of phonon mode at 307 cm^{-1} associated with V_O defects present in the crystal lattice (inset shows corresponding resonant Raman spectra) (b) UV-Visible absorption spectra of In_2O_3 nanowires.	26
12. High resolution XPS spectrum of (a)-(d) C(1s), In (3d) and O(1s). O(1s) spectrum in figure 12(c) and 12(d) shows presence of a minor second peak at higher binding energy associated with chemisorbed oxygen species on the surface of the nanowires.	28
13. XPS valence band photoemission spectra of In_2O_3 nanowires. The separation between the VBM to surface Fermi level was calculated based on linear extrapolation of the leading edge of valence band photoemission spectra.....	29
14. Structural visualization using VESTA of (a) the crystal structure of c- In_2O_3 where the In atoms are labelled with cyan and pink respectively, (b) octahedron morphology dominated by the $\{111\}$ surfaces.	33
15. Low (10 K) and room temperature PL spectra fitted with multiple Gaussian peaks identifying corresponding transition energies.....	35
16. Temperature dependence of the PL (a) NBE and (b) below band edge spectra in In_2O_3 nanowires.	37
17. (a) Temperature dependence of the high energy edge of the NBE peak. (b) Thermal quenching behavior of NBE peak.	39
18. (a) Dependence of NBE peak FWHM on temperature. (b) NBE PL line width as a function of effective carrier concentration based on the impurity band broadening model.....	41
19. (a) Schematic band diagram of In_2O_3 nanowires showing energy transitions due to different charge states of V_O defects and band tailing effect. (b) Upward band bending on the surface due to chemisorbed oxygen species.....	43

LIST OF FIGURES (continued)

20. (a) Schematic showing the pump-probe measurement in transmission mode on a semiconductor nanowire sample [76]. (b) 2D surface plot of the ΔA spectra as a function of probe wavelength and time delay in between pump and probe. 44
21. Experimental setup of the ultrafast TA pump-probe spectroscopy system having a pump wavelength of 310 nm (tunable) and optical probe in the wavelength region 350–700 nm. 45
22. (a) Shows ΔA spectra at various time delays following the 310 nm pump excitation where both probe induced absorption and state-filling could be observed. (b) corresponding carrier kinetics at various probing wavelengths..... 46
23. (a) Carrier kinetics at above band edge (356 nm) and midgap states with corresponding fits showing bi-exponential decay profile where the initial fast component (~ 20 ps) is associated with carrier trapping by lower lying defect levels due to surface states and the longer component (~ 1.5 ns) is attributed to electron-hole recombination process. (b) schematic representation of associated carrier relaxation processes. 47
24. (a)-(b) Pump fluence dependent kinetics at two different probe wavelengths near the band edge and midgap states showing influence of hole trapping at the surface due to adsorbed oxygen species..... 49
25. Comparison of non-resonant Raman spectra before and after annealing at 700 °C for 2 hrs in an oxygen rich environment. 52
26. Room temperature PL spectra showing significant reduction of defect emissions post annealing treatment at 700 °C for 2 hrs in an oxygen rich environment. 53
27. High resolution XPS spectra of O(1s) peak before and after high temperature annealing showing increase in the lattice O^{2-} peak and adsorbed charged oxygen species. 54
28. (a) TA kinetics of In_2O_3 nanowires post thermal annealing treatment and (b) comparative kinetics of as-synthesized and treated nanowires showing significant increase in the carrier relaxation time post treatment. 55
29. Microwave reflection from a semi-infinite plasma medium for different ion density values. 63
30. Schematic representation of the low power 94 GHz transceiver for targeted stand-off measurements of ionizing radiation effects on the nanowire samples. 66

LIST OF FIGURES (continued)

- 31. (a) In-house designed portable low power 94 GHz millimeter wave system for standoff detection of ionizing radiation, (b)-(e) shows different components including NIG (Comtech Research, model IG-133A), Ion counter (Alpha Lab, model AIC20M) and 12” EM lens to focus on an area of $\sim 3 \text{ mm}^2$ 67

- 32. COMSOL modeling and simulation of 94 GHz antenna structure (a) with (b) without teflon dielectric lens for beam focusing. Corresponding electric field patterns are shown in (c) and (d) respectively. 68

- 33. (Top) Scattered millimeter wave signal intensity from as-synthesized nanowires while being exposed to NIG. Measurable changes in the signal intensity could not be observed in this case. (Middle) subplot shows the corresponding differential amplitude and (Bottom) measured ion counts clearly showing the ‘ON’ and ‘OFF’ positions of the NIG. NIG was placed 2 cm away from the sample in the beam path. 70

- 34. (Top) Scattered millimeter wave signal intensity from surface passivated nanowires while being exposed to NIG. Measurable changes in the signal intensity is observed in this case primarily due to diffusion charging of the nanowire surface. NIG was placed 2 cm away from the sample in the beam path. 71

- 35. Control measurement without the nanowires shows no measurable changes due to scattering from ionized air under ambient conditions..... 72

- 36. Scattered signal measured as a function of distance from the NIG where no surface charging effect was seen beyond 10 cm of source and sample separation due to very short lifetime of electrons in ambient atmosphere. 73

- 37. Scattered intensity measured from three different samples spatially separated by 0.5 cm along ‘y-axis’ and 1 cm along ‘x-axis’ as shown in the index showing the ability of the system to perform targeted measurements. 74

- 38. Calibration data showing measured dosage as a function of distance from the source (Hopewell GC-60-A). Dotted arrow line shows for a 200 Ci source, $\sim 40,000$ mr/hr dosage being used in our experiment at a distance of 100 cm from the source. 75

- 39. Actual experimental setup for the ^{137}Cs test where (top) image shows the source, (bottom left) image shows the portable 94 GHz system, (bottom right) the control station located outside the testing facility to monitor and record real-time data during irradiation. 76

LIST OF FIGURES (continued)

40. Shows real-time data collected on two surface passivated samples with 10 and 20 mins of ^{137}Cs irradiation. Approximately 10 mins of data was collected before irradiation which shows near constant response whereas during irradiation, scattering intensity decreases progressively with time due to formation of V_0 defects in the nanowires thereby becoming more lossy. Under post-irradiation condition, again the scattering intensity does not change. 78
41. Shows (top) time domain signal averaged 100,000 times and (bottom) corresponding frequency spectrum. 83
42. Currently available source power from solid-state components in the millimeter wave and terahertz frequency bands. 85
43. Absorption spectra of 100% (a) acetonitrile and (b) ethanol at 20 mTorr. 87
44. Boltzmann distribution of CH_3CN (room temperature 293K, dry ice 195K, liquid nitrogen 77K and liquid helium 4K). 89
45. Schematic of a fast-sweep dual channel 110–140 GHz CP-FTMMW spectrometer for broadband trace gas sensing. 91
46. Time domain signal (top) without and (bottom) with LO leakage being transmitted. 92
47. Segmented measurements using a narrow 20 MHz chirp of $\text{C}_2\text{H}_5\text{OH}$ peaks centered at 119.539 GHz and 120.094 GHz. 93
48. Signal intensity plot at varied FID delay shows the chirp-tailing effect which overwhelms the FID signal. 94
49. Detection of CD_3CN ($J = 8 \leftarrow 7, k = (7 \leftarrow 0)$) and CH_3CN ($J = 7 \leftarrow 6, k = (6 \leftarrow 0)$) simultaneously present in a mixture ratio 1:1 at 20 mTorr pressure with a 200 MHz chirp excitation. 95
50. Detection of isotopologues of CH_3CN at 20 mTorr present in a gas mixture with varied concentration where the ratio of the mixture components ($^{13}\text{CH}_3^{13}\text{CN}/\text{CD}_3\text{CN}/\text{CH}_3\text{CN}$) is 1:4:5. 96
51. Shows real-time averaging capability of the digitizer to reduce the noise in the signal and increase the dynamic limit. 97
52. FID of CH_3CN as a function of cell pressure which shows rapid dephasing at higher pressures. 98

LIST OF FIGURES (continued)

53. Detection of CH_3CN at varied pressure clearly showing the effect of line broadening..... 99

LIST OF ABBREVIATIONS

ATP	Adenosine triphosphate
AWG	Arbitrary waveform generator
BW	Bandwidth
CBRNE	Chemical, biological, radiological, nuclear and explosive
CP-FTMW	Chirped-pulse Fourier transform microwave
CP-FTMMW	Chirped-pulse Fourier transform millimeter wave
CVD	Chemical vapor deposition
CBM	Conduction band minima
Ci	Curie
¹³⁷ Cs	Cesium-137
DFT	Density Functional Theory
EM	Electromagnetic
EW	Electronic warfare
EDX	Energy-dispersive X-ray
FET	Field effect transistor
F.U.	Formula unit
FMC	Frequency multiplier chain
FWHM	Full width at half maximum
FE-SEM	Field-emission scanning electron microscopy
FID	Free induction decay
GHz	Gigahertz
HRTEM	High resolution transmission electron microscopy
IC	Integrated circuits
In ₂ O ₃	Indium oxide
IPA	Isopropyl alcohol
IF	Intermediate frequency
JPL	Jet Propulsion Laboratory
LO	Local oscillator
MoS ₂	Molybdenum disulfide
NIG	Negative ion generator

LIST OF ABBREVIATIONS (continued)

NASA	National Aeronautics and Space Administration
NBE	Near-band-edge
NI	National Instruments
OPA	Optical parametric amplifier
1-D	One-dimensional
PL	Photoluminescence
PNNL	Pacific Northwest National Laboratory
PRC	Power reflection coefficient
PLS	Phase locked synthesizer
PDMS	Polydimethylsiloxane
PA	Power amplifier
RCS	Radar cross section
RF	Radio frequency
SnO ₂	Tin oxide
SNR	Signal-to-noise ratio
SCCM	Standard cubic centimeter per minute
SAED	Selected area electron diffraction
TCO	Transparent conducting oxide
TA	Transient absorption
2-D	Two-dimensional
UV	Ultraviolet
VLS	Vapor-liquid-solid
VBO	Valence band offset
VBM	Valence band maxima
XPS	X-ray photoelectron spectroscopy
ZnO	Zinc oxide

SUMMARY

The importance of sensors and instrumentations capable of detecting chemical, biological, radiological, nuclear and explosive (CBRNE) signatures in real-time intended towards their application in the areas of homeland security, environmental monitoring as well as under various medical and industrial settings cannot be overstated. Further for fieldable applications, the need for alternative detection techniques as well as cheap, low power and cryogen free operation of these sensors and instrumentations are desirable. In this regard, an area of interest which has witnessed insufficient development over the past years is related to the stand-off detection and monitoring of ionizing radiation occurring due to nuclear and radiological events. Traditional ionizing radiation detection methods use semiconductor or scintillator type devices where measurements need to be performed close to the source due to exponential decay of radiation intensity with distance which limits the detection range. One of the current known methods for stand-off detection operate by detecting microwave reflection from elevated ionization region forming a semi-infinite slab with uniform density and an abrupt boundary induced by high power (kW-GW) electromagnetic (EM) sources. A major drawback of these existing stand-off sensing methods arises due to strong dependency of the formed localized plasma density on atmospheric turbulence which can significantly perturb the plasma density often resulting in weak reflection coefficient on the order of 10^{-24} - 10^{-26} which rules out the possibility of any long-range detection. Further due to utilization of high power EM sources, the systems are bulky (not portable) and not suitable for operation under normal environmental settings as the power requirements far exceeds the FCC maximum permissible RF and microwave exposure limit (1.6 W/kg). Limitations of these existing technologies motivated us to

SUMMARY (continued)

investigate into a novel alternative approach by decoupling the sensor material and signal readout electronics. The sensor material is assumed to be coexisting within the target environment which can be part of a covertly or overtly placed tag whereas the readout system could be located at a stand-off distance that interrogates the tag using EM waves at millimeter wave frequencies.

The indium oxide (In_2O_3) nanowire-based sensor material belongs to the family of metal oxide semiconductors which are known to possess excellent chemical sensing properties and has found extensive applications as solid-state gas sensors. In_2O_3 is of interest for chemical sensing due to its high carrier mobility ($>100 \text{ cm}^2/\text{Vs}$) and ability to support very high electron concentrations (10^{20} - 10^{21} cm^{-3}) as compared to closely related materials such as zinc oxide (ZnO) and tin oxide (SnO_2) thereby exhibiting high electrical conductivity and hence superior sensitivity, fast response time as well as low concentration detection capability. Recently metal oxide nanostructures have also been deemed to be promising EM absorbing materials at microwave frequencies due to the occurrence of various defect induced polarization mechanisms. Nanostructures, due to their large surface to volume ratio have promise for novel devices but so far there has not been any in production. Further, recent demonstration of Schottky contacted metal oxide nanostructure based efficient γ -radiation detector provided us with the necessary background as well as motivation to investigate into their application towards stand-off detection of ionizing radiation. Using nanoscale materials also solves the problem of detector size and weight, however adds to the complexity in device design and circuits.

SUMMARY (continued)

Due to cubic crystal structure of In_2O_3 , growth of anisotropic nanostructures such as nanowires becomes challenging, as the surface energy difference among {100}, {110} and {111} facets are minimal. The In_2O_3 nanowires with an average diameter of ~ 100 nm was synthesized via carbothermal reduction technique using a gold-catalyst-assisted vapor-liquid-solid (VLS) method. Attempts to grow In_2O_3 nanowires by directly heating an indium metal source was not successful due to high supersaturation ratio of oxidized indium vapor which essentially facilitates the growth of nanoparticles with octahedron like morphologies and non-uniform dimensions. From the SAED patterns and lattice images, the nanowires were found to be single crystalline in nature and the growth direction of nanowires was determined to be along [100]. Onset of strong optical absorption could be observed at energies greater than 3.5 eV consistent with highly n-type characteristics due to unintentional doping from oxygen vacancy (V_O) defects as confirmed using Raman spectroscopy. A combination of high resolution transmission electron microscopy (HRTEM), x-ray photoelectron spectroscopy (XPS) and valence band analysis on the nanowire morphology and stoichiometry reveals presence of high density of V_O defects on the surface of the nanowires resulting in surface stabilization through the formation of (111) facets which is the overall most stable surface of c- In_2O_3 . The (111) surface is highly sensitive to oxygen chemical potential and as a result, V_O defects can easily form on the surface compared to the bulk.

The nature and position of defect levels due to surface states were further investigated using optical techniques. The origin of the near-band-edge (NBE) peak is believed to be from a series of shallow donor levels formed due to neutral oxygen

SUMMARY (continued)

vacancy (V_O^X). Our data reveals significant broadening of the NBE emission with no excitonic emission features visible even at very low temperatures (10 K) which is clearly an indication of very high doping resulting in the discrete shallow donor levels to merge into an impurity band ultimately leading to a band tail. The effective ionization energies of shallow donor and acceptor like states were calculated to be 6 meV and 75 meV respectively. The width of the band tails, and thus the dependence of the NBE peak line width on carrier concentration, was calculated based on the impurity band broadening model. The calculated electron concentration of $1.2 \times 10^{20} \text{ cm}^{-3}$ at 10 K is higher than the degeneracy limit in In_2O_3 , hence the In_2O_3 nanowires were found to be degenerate with Fermi level lying $\sim 0.05 \text{ eV}$ above the conduction band minima (CBM). The below band edge features are believed to originate from donor levels formed due to singly ionized oxygen vacancies (V_O^+). The surface states were found to have significant influence on carrier trapping process following excitation as revealed through femtosecond resolution time-resolved measurements.

Passivation treatment by performing high temperature annealing in an oxygen rich environment was found to significantly reduce the number of surface V_O defects thereby modulating the nanowire EM absorbing properties as well and hence forming the basis for detector operation. The EM absorbing properties of the In_2O_3 nanowires was interrogated at 94 gigahertz (GHz) millimeter wave frequency for stand-off detection of ionizing radiation. For this purpose, a compact and portable 94 GHz prototype homodyne transceiver was designed for targeted probing. We employed a negative ion generator (NIG) to simulate the ionization effect by electrically producing ion clouds in air near the

SUMMARY (continued)

sample. The as-synthesized nanowires didn't show any detectable change in the scattered 94 GHz signal which was attributed due to damped vibration of surface vacancy defect induced electric dipoles which are repeatedly polarized in an alternating EM field causing strong absorption. However, with the surface passivated nanowires, a detectable change in the scattered signal could be observed when the NIG was turned on with a fast rise time of 0.5 s. The signal intensity gradually decays over 10 s after the NIG was turned off. The enhancement in signal intensity was found to be due to diffusion charging resulting in the formation of concentrated electron plasma effectively jamming the dipoles on the nanowire surface. The surface passivated nanowires were next tested with ^{137}Cs γ -radiation which resulted in strong absorption due to formation of surface defects in the nanowires thereby producing detectable change overtime in the 94 GHz scattered signal.

Taking the next step forward, a fast-sweep chirped-pulse Fourier transform millimeter wave (CP-FTMMW) broadband spectrometer was designed for real-time detection of polar gas molecules intended towards its application in environmental monitoring. Based on the absorption line strength of molecules of interest, available power from solid-state sources and broadening effects at room temperature, the WR-08 band (110–140 GHz) was found to be ideal for detection purposes with high sensitivity and specificity. Ethanol being an asymmetric top molecule has rotational lines distributed throughout the entire frequency band and hence was used as a marker chemical to determine the spectrometer accuracy by comparing the observed transitions with reported data in JPL molecular spectroscopy database. Finally, we were able to successfully detect in real-time different isotopologues of acetonitrile present in a gas mixture thereby

SUMMARY (continued)

demonstrating its importance in chemical analysis. The details about the spectrometer design and performance has been reported and compared with literature reports.

1. INTRODUCTION

(Portion of this chapter is copied from my published manuscript Mukherjee S, Meshik X, Choi M, Farid S, Datta D, Lan Y, Poduri S, Sarkar K, Baterdene U, Huang CE, Wang YY. A graphene and aptamer based liquid gated FET-like electrochemical biosensor to detect adenosine triphosphate. IEEE transactions on nanobioscience. 2015 Dec;14(8):967-72.)

1.1. Nanoscale chemical sensors

Due to an unprecedented growth in the area of device fabrication and processing, researchers have been able to successfully achieve devices in the nanoscale dimension with high precision and reliability. This has revolutionized the area of integrated circuits (IC) manufacturing as more and more transistors are being integrated on a single chip [1] thereby delivering higher computing power and keeping up with the well-known Moore's law. Although, the IC manufacturing industry is still largely dominated by silicon (Si), researchers are looking for alternative solutions for scaling down below 10 nm due to known quantum effects. These solutions include investigation of new materials such as group III-V compound semiconductors with superior electron mobility [2, 3] on Si substrate, one-dimensional (1-D) semiconductor nanowires [4] and two-dimensional (2-D) nanostructures prominent among which are graphene [5] and molybdenum disulfide (MoS₂) [6].

Due to their novel quantum, optoelectronic, physical and chemical properties, 1-D and 2-D nanostructures have also found applications in the areas of photonics [7, 8], chemical and biomolecular sensing [9-14], thermoelectronics [15] and more. In a recent report [10], we have shown successful demonstration of a monolayer graphene-based liquid gated field effect transistor (FET-like) electrochemical nano-biosensor as shown in figure 1 to accurately detect ultralow concentrations of adenosine triphosphate

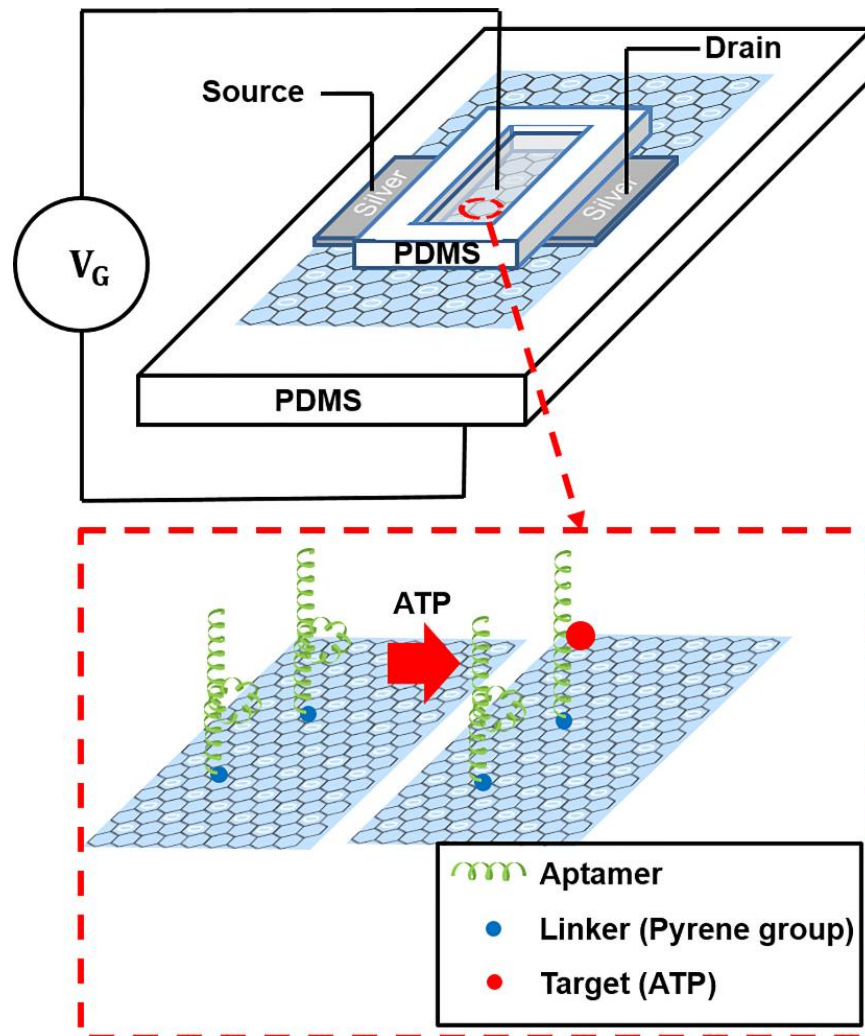


Figure 1: Schematic representation of liquid gated FET-like aptamer-based nano biosensor with a single layer of graphene deposited on a polydimethylsiloxane (PDMS) substrate acting as the conducting channel; silver paste serves as contacts for both source and drain. Inset showing the immobilized aptamers with a 5' pyrene modification attached to the graphene layer via π - π stacking undergoing conformational change upon addition of ATP [10].

(ATP) which is an important biomolecule that is present in all living cells and helps maintain its metabolism. These demonstrations clearly show the tremendous impact that nanostructured-based devices have had in various sensing applications which is

encouraging and calls for further exploration towards their application in new and unexplored areas of research.

1.1.1. Metal oxide semiconductor nanowires: choice of In₂O₃ nanowires as sensor material

Metal oxides are an important class of semiconductors and nanostructures fabricated from these materials have demonstrated excellent chemical sensing properties [16-18] particularly due to their large surface to volume ratio in comparison to their thin-film counterparts on a similar dimensional scale. Among various morphologies of metal oxide nanostructures, nanowires have found most applications however, the growth process have not been well understood. In₂O₃ is of interest for chemical sensing due to its high carrier mobility ($>100 \text{ cm}^2/\text{Vs}$) and ability to support very high electron concentrations (10^{20} – 10^{21} cm^{-3}) as compared to closely related materials such as ZnO and SnO₂ thereby exhibiting high electrical conductivity and hence superior sensitivity, fast response time as well as low concentration detection capability. In₂O₃ is known to be highly n-type due to the presence of large concentrations of intrinsic defects. In a recent study by Yan *et al.* [19] metal oxide nanostructures have also been deemed to be promising EM absorbing materials at microwave frequencies due to the occurrence of various intrinsic defect induced polarization mechanisms arising out of vacancies and dangling bonds. Therefore, the ability to tailor the defect properties in In₂O₃ nanowires thereby modulating its EM absorbing behavior at microwave-millimeter wave frequencies would serve as an effective way to perform stand-off sensing using this nanostructured material as a sensor tag. One such area of application would be to perform covert or overt monitoring of radioactivity from a substantial stand-off distance by deploying such multiple sensor tags

within the target environment. These tags on targeted surfaces for stand-off monitoring could be as simple as sensor paints [20] or more sophisticated designs can be envisioned comprising of a sensor material integrated with a wireless transmitter.

1.2. Real-time detection and monitoring of CBRNE signatures – intended applications and underlying challenges

There is an urgent need for technologies that can detect and analyze CBRNE signatures in real-time for application in the areas of homeland security, environmental monitoring and under various medical and industrial settings. In recent times, the world has seen increasing activities on radioactive materials as well as hazardous chemicals for various energy and defense related applications. While the advancement of technology in these particular areas are of utmost importance for building a better and safer tomorrow, however the risk factor involved, and misuse of any sort can have devastating consequences on the environment. Over the years we have seen many such instances notable among which was the Fukushima Daiichi nuclear disaster in 2011 which has led to widespread radioactive contamination causing multiple deaths and severe detrimental effect on surrounding environment. Two of the areas that needs attention are (a) stand-off detection and monitoring of ionizing radiation in the atmosphere occurring due to nearby nuclear or radiological events and (b) analysis of target atmosphere for identification of chemical signatures with high sensitivity and specificity. Further, it is desirable for the next generation CBRNE detection and monitoring technologies to be small and compact, easily affordable which can be synthesized in large scale and can operate without the requirement of cryogenic cooling unlike bolometer detectors or molecular beam systems. All these

factors have motivated us to investigate into novel materials, detection methods and instrumentations to tackle the stated problems.

1.3. Overview of detection concepts

In the EM spectrum, millimeter wave corresponds to the radio band frequencies of 30–300 GHz ($\lambda = 1–10$ mm) which has only recently gained popularity due to its application in 5th generation wireless systems. This is because research and development efforts on millimeter wave technologies has mostly been limited to military and aerospace applications particularly towards electronic warfare (EW), security and next generation tactical networks to increase connectivity. Another reason for its gaining popularity is the availability of high power and high frequency compact solid-state components such as GaN HEMT-based power amplifiers (PA), GaAs Schottky diode-based frequency multiplier chains (FMC) and mixers that can be easily incorporated into portable transmitter and receiver units without the requirement for cryogenic cooling. Therefore, researchers are exploiting the possibility of scaling down bench top systems for fieldable applications.

1.3.1. Millimeter wave stand-off detection of ionizing radiation by probing radiation interaction with sensor material

Stand-off radar-based detection at microwave and millimeter wave frequencies of chemical signatures including radiation-induced ionization in air has been explored in the past [21-29]. One of approaches explores a method of determining millimeter wave scattering from radioactive plumes under highly humid conditions, mechanism of which has been explained based on the ion-cluster aerosol model [22]. This method has been tested at a stand-off distance of ~ 2 m by simulating an environment where water droplets

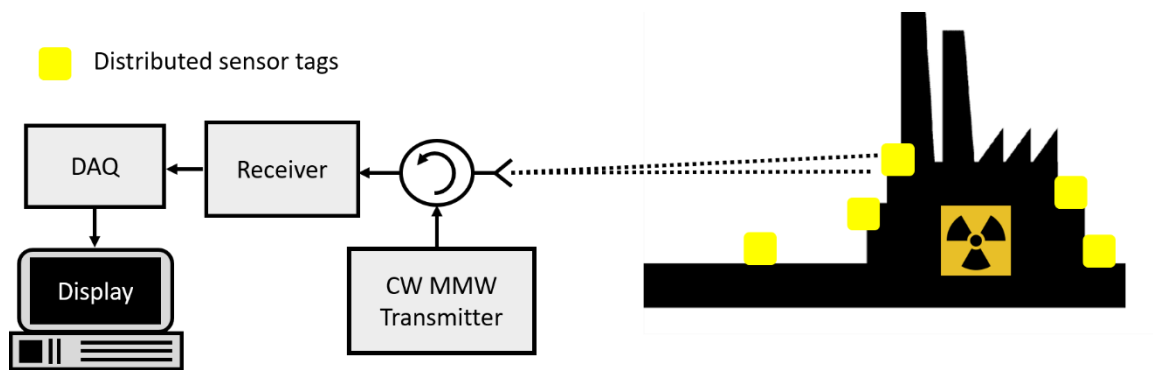


Figure 2: Schematic representation of a millimeter wave system to detect ionizing radiation effects by interrogating sensor tags deployed in the vicinity of the source.

were produced by an ultrasonic atomizer and were subsequently charged and discharged using a NIG and a low energy X-ray source. This method is advantageous in the sense that no high-power component is required thereby bypassing the need for cryogenic cooling. However, a drawback of the system lies within the necessary atmospheric condition of high humidity that needs to be satisfied for detectable backscattering intensities. In another attempt, Sprangle *et al.* [27] theoretically demonstrated γ -radiation induced frequency modulation of a 94 GHz millimeter wave probe beam is possible due to elevated plasma density created by photo-detachment of electrons from O_2^- ions by using a high power pulsed laser having a peak intensity of 160 GW/cm^2 and pulse duration of 1 ns. Further recently, Kim *et al.* [28] proposed that lower power of the incident EM wave is sufficient for plasma breakdown at atmospheric-pressure air and demonstrated experimentally by utilizing a 95 GHz, 30 kW gyrotron source to induce plasma breakdown in the presence of radioactive material. However, all these methods are highly susceptible to atmospheric turbulence which can adversely affect any long-range detection. In addition, all these systems are bench top compatible and the gyrotron EM sources requires additional

cryogenic cooling for proper operation which are not desirable for rapid deployment or fieldable solutions.

The shortcomings motivated us to investigate into a new stand-off detection architecture which is immune to atmospheric turbulence as well as compact and does not require cryogenic cooling. The demonstrated measurement method utilizes metal oxide nanowire-based dielectric material which acts as the sensor material and is assumed to be coexisting within the target environment which can be part of a covertly or overtly placed tag. A schematic of the detection scheme is shown in figure 2. The signal readout electronics uses a compact, low power 94 GHz millimeter wave transceiver for stand-off interrogation of the sensor material in real-time thereby picking up any changes in the signal reflectivity when it is exposed to ionizing radiation. The utilization of 94 GHz millimeter wave frequency is a suitable choice for stand-off sensing due to its relatively high atmospheric transparency as shown in figure 3 and small antenna beam widths which allows the beam to interrogate small distant objects with higher spatial resolution. Though this technique can provide real-time information in detecting radioactivity, however it lacks specificity in determining the nature of the source. To tackle such situations where high specificity is desired, we subsequently investigated into the development of a microwave-millimeter wave spectrometer which can detect chemical effluents in real-time by identifying their rotational signatures. The concept has been introduced and outlined in the following section.

1.3.2. Millimeter wave spectroscopic detection of gas phase compounds

To ensure safety and security of surrounding environment, there is a need for chemical sensing systems for wide-area monitoring of stack gas or effluents that are

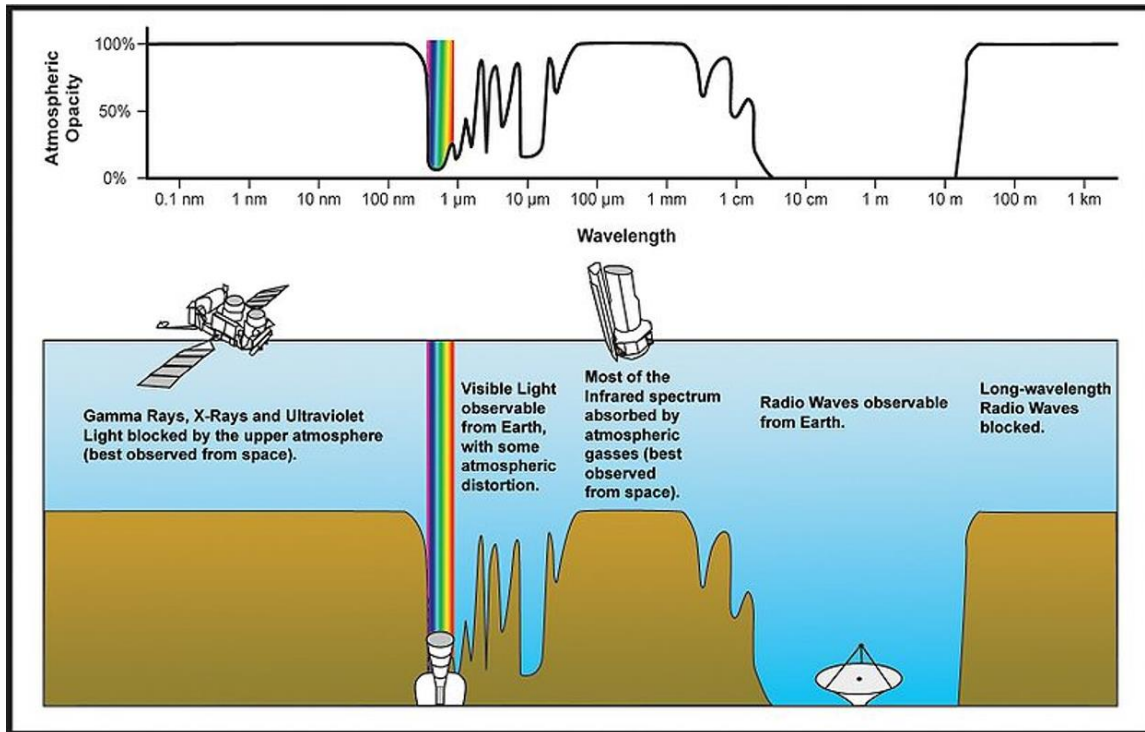


Figure 3: Atmospheric EM opacity, Courtesy: National Aeronautics and Space Administration (NASA).

released from nearby process plants. The requirement for such systems would be to perform trace gas analysis with high sensitivity and resolution. In this regard, millimeter wave rotational spectroscopy is a well-known standard laboratory technique for gas or vapor phase characterization and has found successful applications in areas such as molecular structure and conformation determinations to measurements of dipole moments [29]. In its true sense, remote monitoring of chemical signatures in the environment with high sensitivity and resolution is not feasible. This is partly because, it will require measurements to be performed at ambient atmospheric pressure which can cause significant broadening of the spectral lines and reduction in peak intensity [30]. In this regard, the conventional method is sampling of target airspace followed by detection under

controlled environment such as within a sample gas chamber, where both temperature and pressure can be precisely monitored. However, the size and complexity of such microwave-millimeter wave spectrometers and its accessories along with significant acquisition and processing times has limited their use for in-field real-time applications.

In high resolution millimeter wave spectroscopy, the conventional approach has been simple direct absorption type measurements where a wide frequency window is gradually stepped across single frequency point at a time. With this approach, typically within a second, 1–10 frequency points are acquired having 10–100 kHz of spacing between them. The spectrometer signal output is then detected through a lock-in amplifier, thereby enhancing the signal-to-noise ratio (SNR) of the acquired spectrum. Very high sensitivity can be achieved at the cost of extremely long scanning time for just a single acquisition and may take up to several hours or even days to acquire time averaged data depending on the nature and complexity of the experiment. In recent study, Hays *et al.* [31] demonstrated a fast-sweep direct absorption millimeter wave spectrometer which takes 1.5 ms to acquire single shot of 2 GHz bandwidth (BW). Further it took almost an hour to acquire 10^6 time-averaged data which clearly rules out the possibility of using such technique for wideband spectral coverage in real-time.

Chirped-pulse Fourier transform microwave (CP-FTMW) spectroscopy invention at the University of Virginia by Pate and co-workers was propelled mainly due to considerable advances in high-speed digital electronics for both pulse generation and broadband detection [32-34]. This technique has made possible truly broadband detection in the microwave region of 7–18 GHz with >10 GHz per pulse of Fourier-transform spectra which can now be acquired within a few microseconds thereby having the capability of

real-time detection. We have further investigated this technique and considering recent and ongoing developments of high frequency and relatively high power $\sim(30\text{--}200\text{ mW})$ solid-state components, have determined WR-08 as one of the optimal frequency bands for in-field spectroscopic measurements with high sensitivity and specificity. Here we report on the design and operation of a fast sweep CP-FTMMW spectrometer which can operate within the 110–140 GHz frequency band and is promising for broadband chemical sensing in real-time and suitable for in-field applications because of its compact design.

1.4. Dissertation outline

The experimental growth procedure of the In_2O_3 nanowires has been presented in chapter 2. A detailed analysis on the influence of synthesis process parameters on various nanostructure morphologies is presented and interpreted using Wulff shape construction. Further analysis on the crystal quality of the as-synthesized nanowires and their surface properties has been studied using HRTEM, Raman spectroscopy and XPS.

Chapter 3 discusses on the intrinsic defects present in In_2O_3 and the identification of nature and position of the defect levels due to surface states in the as-synthesized nanowires using optical techniques. A detailed analysis on the very first observation of NBE photoluminescence (PL) broadening due to unintentional heavy doping has been reported. Further the effect of the carrier trapping due to surface states has been studied using ultrafast time-resolved spectroscopy. Lastly, the purpose of performing high temperature passivation treatment has been discussed and its effect in modifying the nanowire surface properties has been studied.

We have presented in chapter 4 the very first application of In_2O_3 nanowires as sensor material for stand-off detection of ionizing radiation. The theory behind the interaction of

γ -radiation with semiconductor material and EM wave-plasma interaction has been discussed. Further, here we report on the design and modeling of a compact 94 GHz transceiver and related components for targeted stand-off measurements. Finally, we report on the experimental observation on as-grown and surface passivated samples under simulated and realistic scenarios by using a NIG and ^{137}Cs source.

Chapter 5 discusses the design, operation and characteristics of a state-of-the-art WR-08 (110–140 GHz) fast sweep CP-FTMMW spectrometer for broadband chemical sensing in real-time. The choice for the selected frequency band along with various design aspects has been discussed in detail. Finally, we report on the successful identification of various isotopologues of acetonitrile by analyzing a sample gas mixture.

Chapter 6 summarizes the results presented in the dissertation and identifies relevant areas for future work.

2. METAL OXIDE SEMICONDUCTORS: INVESTIGATION OF GROWTH

MECHANISM AND MORPHOLOGICAL DEFECTS OF In_2O_3 NANOWIRES

(Portion of this chapter is copied from my published manuscript
Mukherjee S, Sarkar K, Wiederrecht GP, Schaller RD, Gosztola DJ, Stroscio MA, Dutta M. Defect induced structural inhomogeneity, ultraviolet light emission and near-band-edge photoluminescence broadening in degenerate In_2O_3 nanowires. *Nanotechnology*. 2018 Mar 1;29(17):175201.)

We have investigated here the growth mechanism and defect induced changes on the morphology and surface properties of In_2O_3 nanowires. In_2O_3 nanowires with cubic crystal structure (c- In_2O_3) were synthesized via carbothermal reduction technique using a gold-catalyst-assisted VLS method. The structural and compositional characterization results are presented next where onset of strong optical absorption was observed at energies greater than 3.5 eV consistent with highly n-type characteristics due to unintentional doping from oxygen vacancy (V_O) defects as confirmed using Raman spectroscopy. A combination of HRTEM, XPS and valence band analysis on the nanowire morphology and stoichiometry reveals presence of high-density of V_O defects on the surface of the nanowires. As a result, chemisorbed oxygen species can be observed leading to upward band bending at the surface which corresponds to a smaller valence band offset (VBO) of 2.15 eV.

2.1. Growth of In_2O_3 nanowires

Oxide semiconductor nanostructures are well known due to their novel physical, chemical and optoelectronic properties which finds applications in areas including nanoelectronics, sensing and nanophotonics. Among oxide materials, In_2O_3 nanostructures have been found to be an interesting candidate for a variety of technological applications including transparent conducting oxides (TCO) [35-37], gas sensors [38], light-emitting

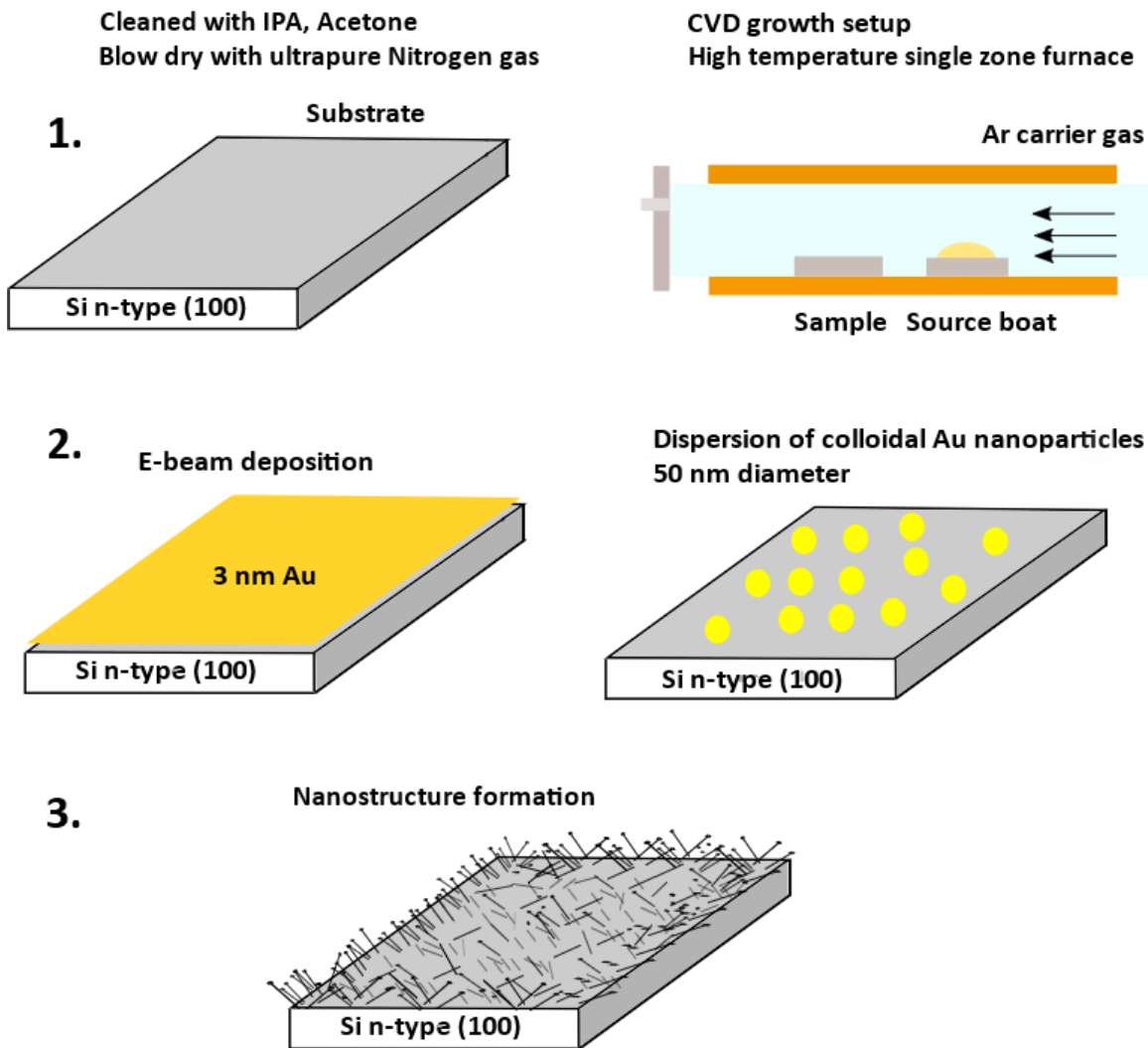


Figure 4: Schematic illustration of the chemical vapor deposition (CVD) process for the growth of In_2O_3 nanowires.

devices [39] and field-emission devices [40]. However, unlike other oxides, the nature of the electronic band structure (direct or indirect) and energy gap values (2.9 – 3.75 eV) in In_2O_3 are not well understood [41]. Also, contrary to the surfaces of the closely related materials such as ZnO and SnO_2 , the surfaces of In_2O_3 have been studied to a much lesser extent by means of electronic structure calculations [42]. Further, the variations in morphology and stoichiometry exhibited by the surfaces as a function of the growth

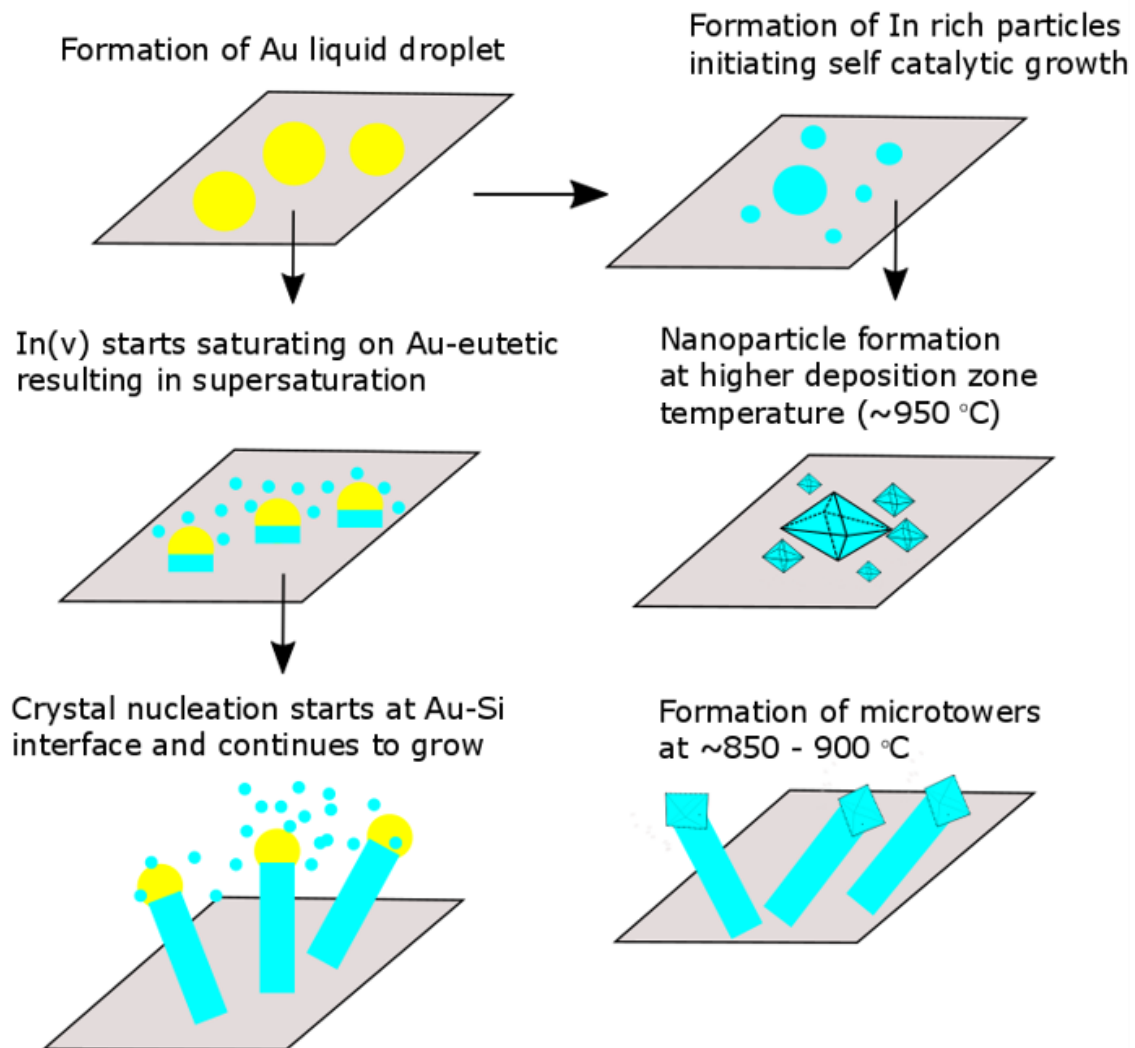


Figure 5: Schematic illustration of the Au-catalytic and self-catalytic VLS method resulting in the growth of In_2O_3 nanostructures under varied deposition zone temperatures.

environment are not well understood. Most of the efforts have been focused on optimizing the material fabrication and studying the electrical properties. The present work is aimed to address this deficiency and a comprehensive analysis based on experimental observations has been reported.

Most of the band gap values for In_2O_3 as reported in the literature were obtained either by transmittance or optical absorption measurements. In_2O_3 has strong optical absorption in the ultraviolet (UV) region (~ 3.75 eV) which has been widely interpreted as a direct band gap [43], until recently a revised fundamental gap of ~ 2.67 eV has been revealed through first-principles calculations and XPS measurements [44,45]. Presence of a pronounced indirect fundamental gap in In_2O_3 has also been controversial and recent reports have proposed either the presence of a parity forbidden direct gap or an indirect gap with valence band maxima (VBM) away from the Γ -point by only 50 meV [46] and is still being discussed. In_2O_3 crystal structure can form cubic (c- In_2O_3), hexagonal (h- In_2O_3) and rhombohedral (rh- In_2O_3) type depending on the nature of precursor being used as well as growth conditions [47]. The cubic crystalline phase is found to be the most stable and commonly occurring [46]. Due to cubic crystal structure of In_2O_3 , growth of anisotropic nanostructures such as nanowires becomes challenging, as the surface energy difference among $\{100\}$, $\{110\}$ and $\{111\}$ facets are minimal [48]. Variation in growth environment and associated process parameters such as source and deposition zone temperatures, oxygen partial pressure, carrier gas flow rate, introduction of catalyst, etc. can create significant structural defects in In_2O_3 which can alter the surface energies of various crystallographic planes [48]. This can modify the external morphology and hence the properties of the formed In_2O_3 nanostructures, thereby forming the basis for their broad range of applications [40]. Understanding the nanostructure morphology, nature of the surface states and their influence on the electronic band structure are the key factors to optimize device performance fabricated from these nanostructures for various optoelectronic and sensing applications.

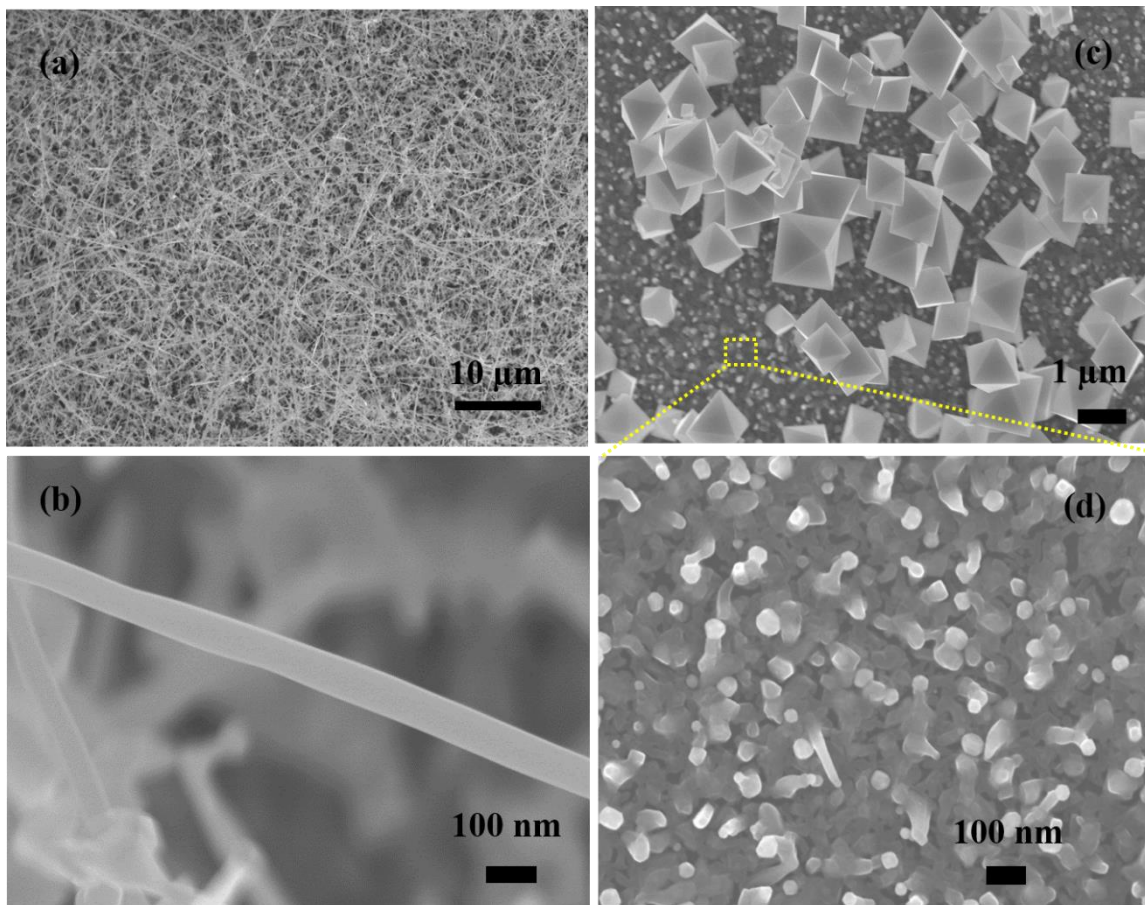


Figure 6: (a) Low resolution FESEM image of dense mesh of In_2O_3 nanowires grown on Si substrate using carbothermal reduction process and VLS technique (b) corresponding high resolution image of a single nanowires with an average diameter of 100 nm (c) shows low resolution image of In_2O_3 nanoparticles with octahedron like morphologies grown using In metal source as the precursor on Si substrate (d) corresponding high resolution image of the substrate background showing the presence of truncated nanowire like features.

2.1.1. Experimental details

In_2O_3 nanowires were synthesized on silicon substrates coated with ~ 3 nm Au catalyst deposited using e-beam evaporation. A mixture of In_2O_3 and graphite at a weight ratio of 4:1 was used as a source to prepare the In_2O_3 nanowires. The mixture was then transferred into a ceramic boat and placed inside a 2'' diameter quartz tube in a single zone furnace. The boat was positioned in the center of the quartz furnace tube and the Au coated

Si substrate with $\langle 100 \rangle$ crystal orientation was placed downstream from the mixed powders [37]. Figure 4 represents a schematic illustration of the CVD process steps. The source was heated up to 950 °C in about 35 mins and the temperature of the deposition zone was adjusted by varying the distance of the substrates from the source. The nanowire growth was carried out at a deposition zone temperature of 900 °C which is ~6 cm downstream from the center of the furnace for 45-50 min duration at a constant flow of 300 standard cubic centimeter per minute (sccm) of Argon as a carrier gas. Nanoparticles with octahedron like morphologies were synthesized using Indium metal shots of 2-5 mm diameter as the source. The nanoparticle growth was performed at a higher deposition zone temperature of 950 °C with the substrates placed adjacent to the source boat at the center of the furnace. The growth duration was varied in between 30-60 min keeping other experimental conditions same as that used during the nanowire growth. A schematic illustration of the VLS growth model is presented in figure 5.

Low resolution images of randomly assembled nanostructures were obtained using a JEOL JSM7500F field emission scanning electron microscope (FE-SEM). HRTEM images of the nanostructures were obtained using a JEOL JEM 3010 electron microscope. XPS measurements were performed using a Kratos AXIS-165 spectrometer equipped with a monochromatic Al K α source (1486.6 eV). The take-off angle of the spectrometer was zero with respect to the sample surface and the 20 eV pass energy was used with a step size of 0.1 eV. Optical properties were investigated using Raman spectroscopy using Renishaw inVia Confocal Microscope with 633 nm non-resonant and 325 nm resonant excitation wavelengths, PL spectroscopy at room temperature with 290 nm excitation from a xenon lamp and collected using Horiba Jobin-Yvon Nanolog Spectrofluorimeter

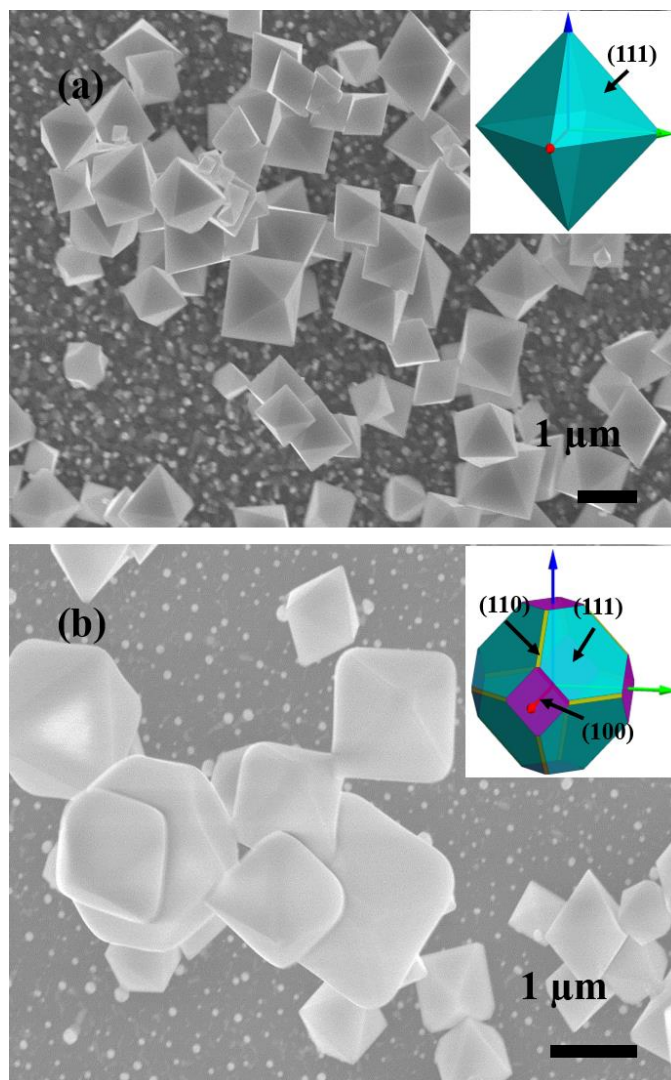
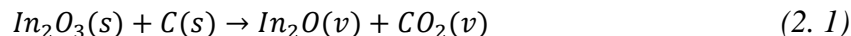


Figure 7: Low resolution SEM images of (a) perfect octahedrons and (b) truncated octahedrons like structures, inset in (a) and (b) shows corresponding computed Wulff shapes where the planes (110), (100) and (111) are represented with colors yellow, purple and cyan respectively.

while low temperature PL investigation was done in a closed cycle helium cryostat capable of reaching down to 10 K. All experiments were repeated over multiple samples for reproducibility.

2.1.2. Influence of synthesis process parameters on the nanostructure morphology

Figure 6(a) shows SEM image of a dense mesh of In₂O₃ nanowires synthesized via the carbothermal reduction technique. In₂O₃ powder couldn't evaporate by itself due to its very high melting point (1910 °C). As a result, there are intermediate reaction steps involved at both the source and deposition sites. Redox reactions at the source generate In₂O(v) which possesses a very high vapor pressure and is transported downstream to the Au coated silicon substrates where it gets absorbed by the Au-catalytic droplets and decomposes to In(l) and In₂O₃(s). The In(l) further reacts with Au clusters to form an Au-In eutectic which becomes the preferred absorption site for incoming In₂O(v). Supersaturation of the eutectic results in the precipitation of In(s) at the liquid-solid interface where it reacts with oxygen to form In₂O₃(s). Au-catalyst assisted 1-D growth continues as long as there is sufficient supply of In₂O(v). The possible reactions steps can be described by the following [49]:



The nanowires were found to have an average diameter of ~100 nm as shown in figure 6(b). Attempts to grow In₂O₃ nanowires by directly heating an indium metal source was not successful. From figure 6(c) and figure 6(d), we observe that the 1-D growth appears to have stopped intermittently. This might be due to high supersaturation ratio of oxidized indium vapor which essentially facilitates the growth of nanoparticle like structures [48]. The computed Wulff shape based on the ratio of growth rate (r) perpendicular to different low-index crystallographic planes reveals perfect

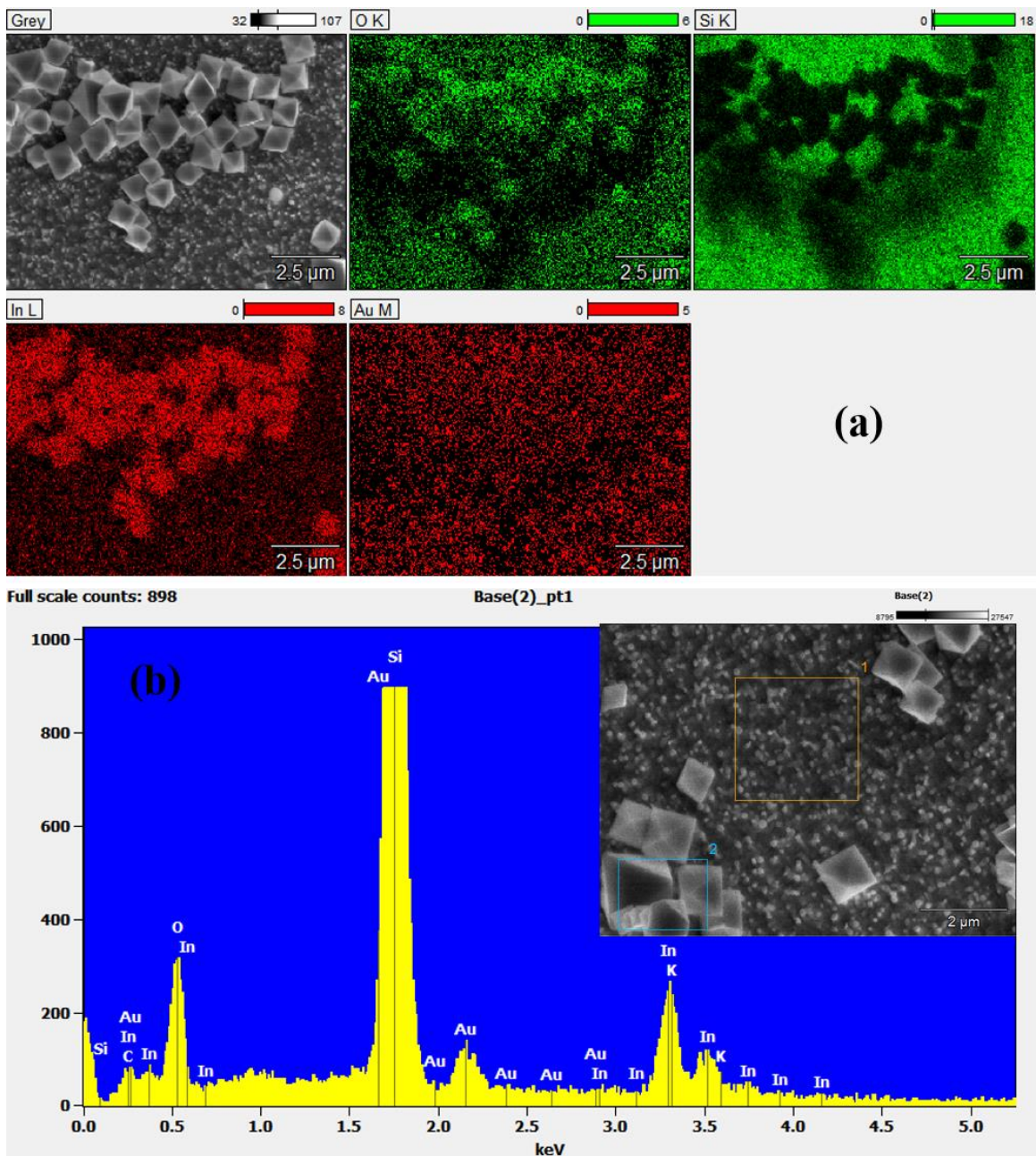


Figure 8: (a) Energy-dispersive X-ray (EDX) mapping of In_2O_3 nanoparticle sample and (b) wide area EDX profile of the background labelled as ‘1’ in the inset which clearly shows the evidence of Au catalyst thereby confirming the growth of truncated nanowire features following the VLS route.

octahedron formation when $r_{\{100\}}:r_{\{111\}} \approx 1.73$ as shown in figure 7(a). We also observed truncated octahedron like features shown in figure 7(b) which could be due to

environmental disturbances inside the quartz tube. Formation of these structures corresponds to $r_{\{110\}}:r_{\{100\}}:r_{\{111\}} \approx 1.2:1.2:1$, which agrees well with the experimental observations and with literature reports [48, 50]. Unlike the growth of uniform diameter nanowires, the size of the nanoparticles with octahedron like morphologies varied considerably ranging from 200 nm to 1.5 μm in diameter. This variation in the size of the nanoparticles could be due to their uncontrolled growth from self-catalytic nucleation sites as no evidence of Au catalyst was found from corresponding elemental mapping as shown in figure 8(a).

Nanoscale features present in the background of the nanoparticle samples labelled as region 1 in the inset of figure 8(b) were found to be truncated nanowires whose growth had stopped intermittently. EDX wide area measurement on region 1 as shown in figure 8(b) reveals presence of Au catalyst which confirms growth of these features were initiated from Au-catalytic nucleation sites. The In_2O_3 nanoparticles are believed to be growing from self-catalytic nucleation sites instead of Au catalyst assisted growth while using indium metal as the source. Low melting point of indium which is 156.6 $^\circ\text{C}$ at 1 atm, leads to the formation of oxidized indium vapor at a much faster rate. $\text{In}_2\text{O}(v)$ is the dominating evaporating component and is transported downstream by the carrier gas which gets adsorbed by Au-catalytic droplets and decompose into $\text{In}(l)$ and $\text{In}_2\text{O}_3(s)$. Due to high supersaturation ratio of oxidized indium vapor to saturated oxidized indium vapor, $\text{In}(l)$ droplets with high surface energy becomes preferred absorption sites where similar growth rates perpendicular to $\{100\}$, $\{110\}$ and $\{111\}$ facets leads to the formation of octahedron like morphologies. Unlike 1D growth, here the growth occurs laterally through side surfaces and any small variation in the size of the initial nucleation

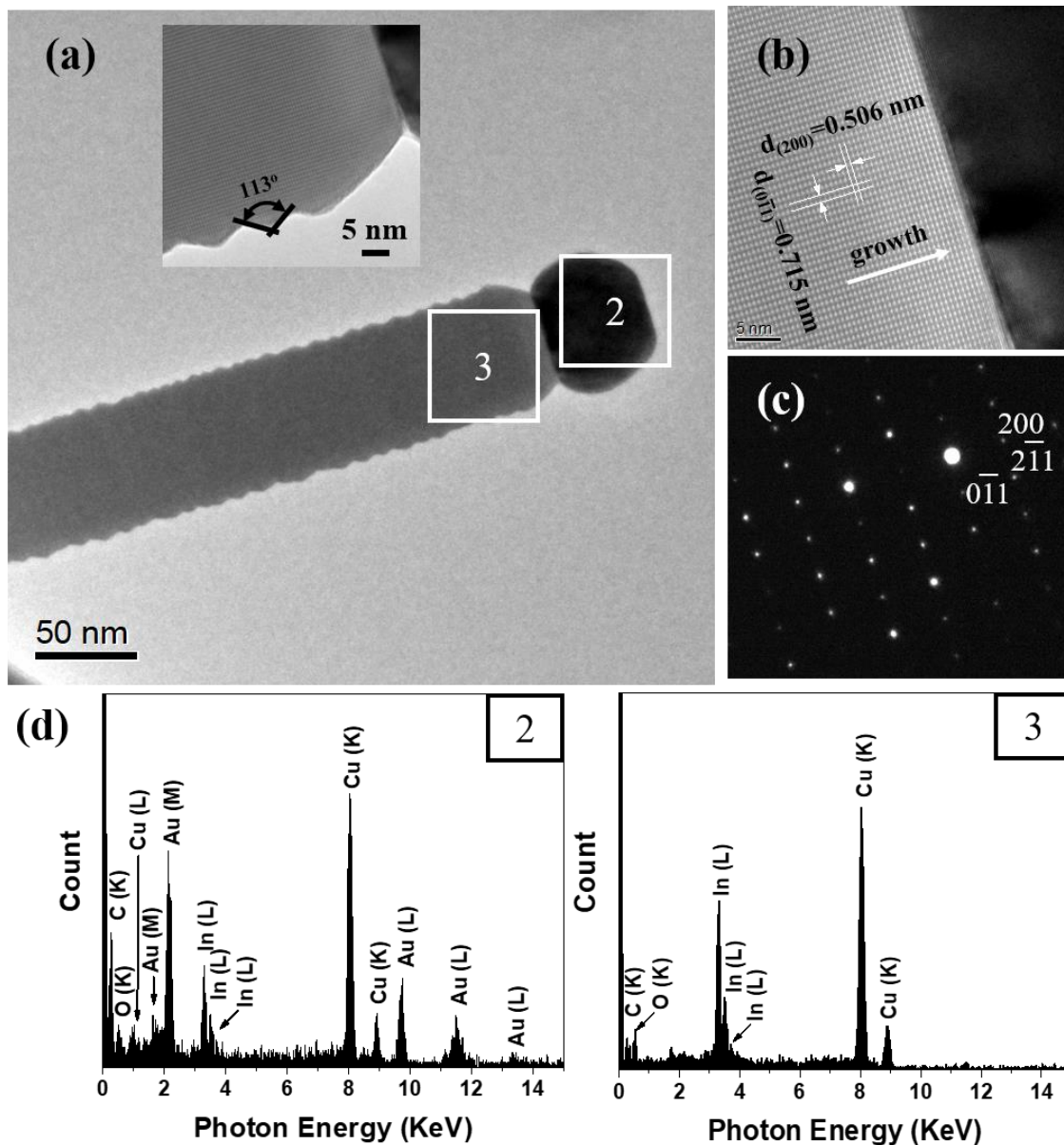


Figure 9: (a) TEM image of a single In₂O₃ nanowire, inset shows surface roughness. (b), (c) HRTEM image and SAED pattern of In₂O₃ nanowires which reveals growth along [100] direction and single crystalline properties with cubic crystal structure. (d) EDX spectrum shows elemental constituents at and below the tip of the nanowire.

site could have a remarkable effect on the overall nanoparticle size depending on the growth time.

2.2. Structural and compositional characterization

HRTEM, selected area electron diffraction (SAED) and EDX characterization were performed on individual In_2O_3 nanostructures to gain insight regarding the morphology and the representative results are shown in figure 9 and figure 10. The nanostructures were found to be single crystalline in nature with body-centered cubic (bcc) crystal structure as observed from the HRTEM and corresponding SAED images shown in figure 9(b)-9(c) and figure 10(b)-10(c). The interplanar spacing of the lattice fringes along the longitudinal and transverse directions was measured to be 0.506 nm and 0.715 nm which correspond to (200) and (0 $\bar{1}$ 1) planes respectively [49]. From the SAED patterns and lattice images, the growth direction of the nanowires was determined to be along [100]. Point EDX measurements performed at two different sites on a single nanowire as numerically labeled in figure 9(d), reveals that the tip of the nanowire is rich in Au-In, thereby confirming the nanowires have grown following the Au-catalytic VLS route as discussed earlier. Consistent with our EDX mapping results shown in figure 8(a), point EDX measurement on the tip of a nanoparticle as shown in figure 10(a) and figure 10(d) which provides higher resolution, also didn't reveal any traces of Au catalyst thereby reaffirming that the growth occurred through a self-catalytic VLS route. HRTEM images taken at the edge of the nanowires reveals a rugged morphology on the nanoscale where the angle between the two consecutive edge planes was determined to be $\sim 113^\circ$ and appears to be symmetric with respect to the edge normal as shown in the inset of figure 9(a). Since the inclusion angle between (100) and (111) planes is 54.7° , the edges are believed to be {111} planes and has been previously reported by Jean *et al.* [49] which was observed during In_2O_3 nanotower formation.

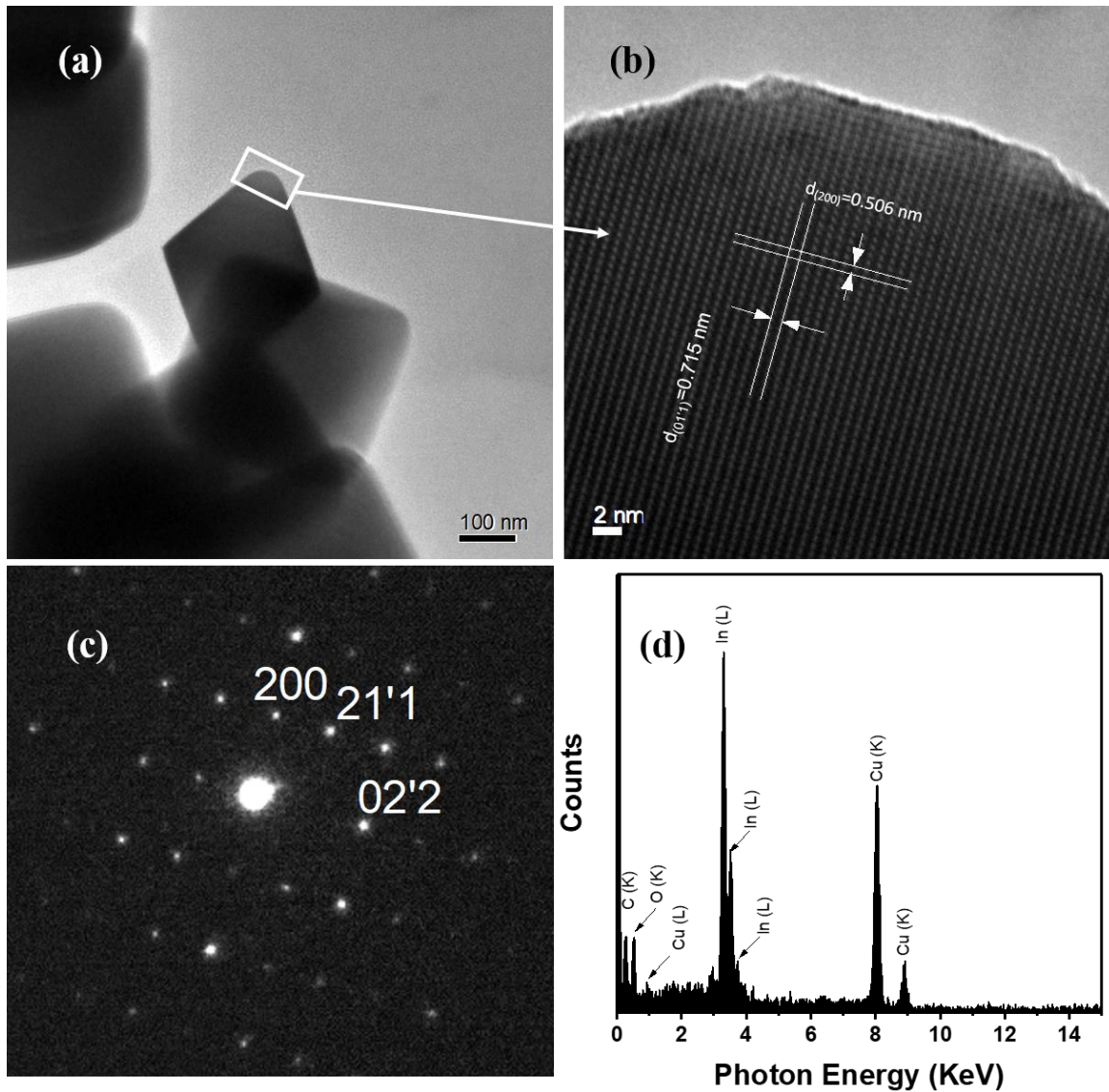


Figure 10: (a) Low resolution TEM image of In_2O_3 nanoparticles (b), (c) HRTEM image and SAED pattern of In_2O_3 particles which reveals presence single crystalline properties with cubic crystal structure. (d) EDX spectrum shows elemental constituents at the tip of the nanoparticle which shows no evidence of Au catalyst.

2.2.1. Analysis on the crystal quality of the as-synthesized nanowires using Raman spectroscopy

Raman spectroscopy analysis was carried out at room temperature to study the crystal quality of the In_2O_3 nanowires as shown in figure 11(a). From the Raman spectrum,

we see in total 11 modes of A_g , E_g and T_g symmetry that are ascribed to typical modes in $c\text{-In}_2\text{O}_3$. Phonon modes having weak scattering intensities however can be expected to be visible with resonant excitation as shown in the inset of figure 11(a), where the phonon mode at 307 cm^{-1} is resolved into two constituent modes of E_g (306 cm^{-1}) and T_g (319 cm^{-1}) symmetry respectively. However, with resonant excitation, a significant fluorescence background was present and needed to be subtracted which resulted in the overall spectra to appear noisier. A breakdown of the usual $\vec{q} = 0$ selection rule occurs if defects due to doping, impurities or lattice disorder are introduced into the crystal, thereby resulting in asymmetry as well as broadening of the Raman line shape. We observe significant broadening of the phonon mode centered at 307 cm^{-1} having an FWHM of $\sim 12\text{ cm}^{-1}$. This mode corresponds to the stretching mode in In_2O_3 and is very sensitive to V_O [40]. V_O defects are expected to be present in very high concentration because of significantly lower formation energies [46] and correlates well with our absorption measurements. Comprehensive optical analysis has revealed that strong optical transitions occur only from $\sim 0.8\text{ eV}$ below the top of the valence band [44]. From optical absorption measurements as shown in figure 11(b), we observed the onset of strong absorption at energies between $3.5\text{--}3.75\text{ eV}$. However, a well-defined value of the optical gap could not be ascertained by analyzing a long-section wavelength of the absorption edge. The observed characteristic could arise due to the presence of additional energy states near the conduction band edge because of V_O defects formed mostly on the surface of the nanowires [41]. These surface states can trap electrons from the valence band and make a contribution to the absorption. Unintentional doping because of V_O defects results in an n-type characteristic as two free electrons are added to the crystal lattice every time a vacancy is

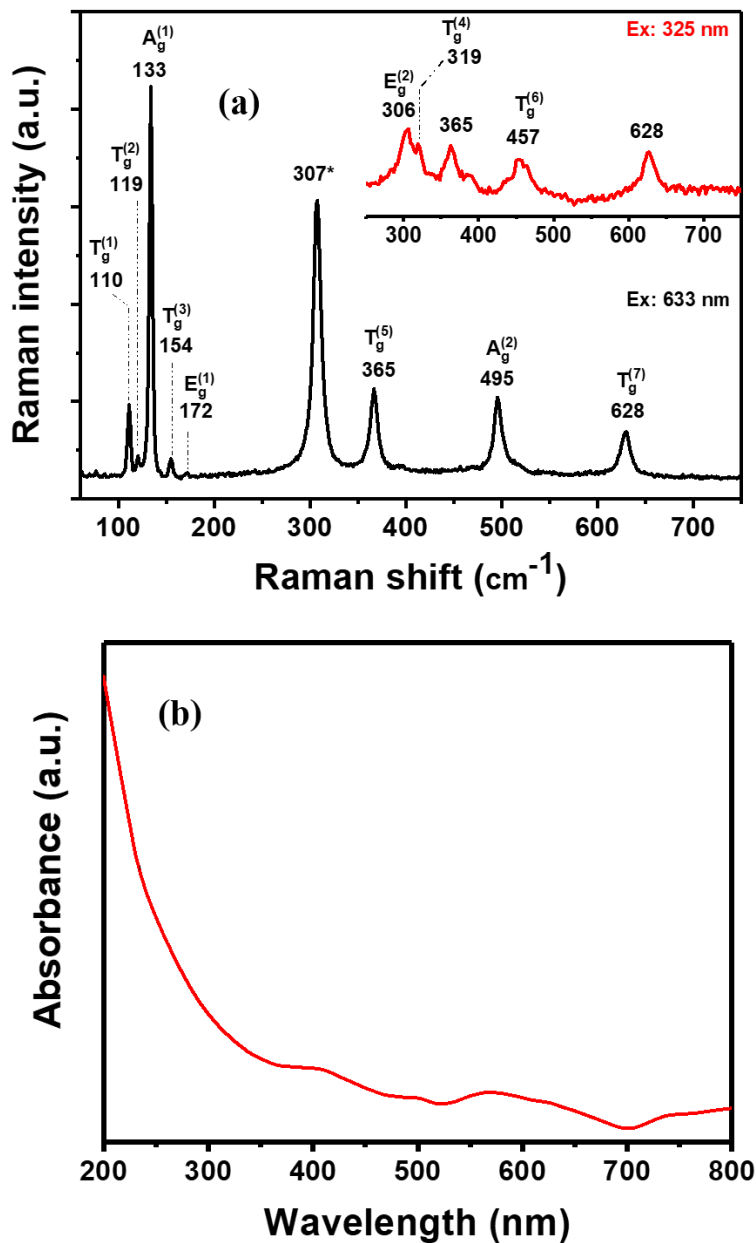


Figure 11: (a) Room temperature non-resonant Raman spectra of In₂O₃ nanowires showing significant broadening of phonon mode at 307 cm^{-1} associated with V_O defects present in the crystal lattice (inset shows corresponding resonant Raman spectra) (b) UV-Visible absorption spectra of In₂O₃ nanowires.

created. High density of V_O defects thereby may shift the Fermi level close to the conduction band edge resulting in the In_2O_3 nanowires to become highly n-type semiconductor.

2.2.2. Nanowire surface modification through faceting and chemisorption

It is well known that stabilization of surfaces with a resultant non-zero dipole moment perpendicular to the surface occurs through rearrangement of surface charges or through introduction of compensating charges into the outermost surface planes. Such reconstruction can significantly affect the surface geometric structure as well as stoichiometry and often has been associated with surface roughening or adsorption of foreign atoms [51]. The bcc-structure of In_2O_3 is related to a $2 \times 2 \times 2$ supercell of fluorite and its bixbyite surfaces are very similar in appearance to those of the parent fluorite structure [46]. The (001) surface of fluorite is a “Type III” ionic surface within the Tasker classification and contains alternating cation and anion planes thereby giving rise to a surface dipole [52]. This may be stabilized in a simple manner through faceting [52] as can be observed in figure 9(a) where (111) facets have formed, which is the overall most stable surface of c- In_2O_3 followed by the (011) surfaces. The (111) surface is highly sensitive to oxygen chemical potential. As a result, V_O defects can easily form on the surface compared to the bulk which might result in chemisorption of oxygen species on the In_2O_3 surface as well as band bending effects due to surface states [53].

High resolution XPS measurements were performed and the binding energies were corrected with respect to the well-known C(1s) peak at 284.6 eV as shown in figure 12(a). The In $3d_{5/2}$ peak and O(1s) peak are observed at 444.85 eV and 530.3 eV respectively, suggesting that the major constituent phase is In_2O_3 as shown in figure 12(b). Background

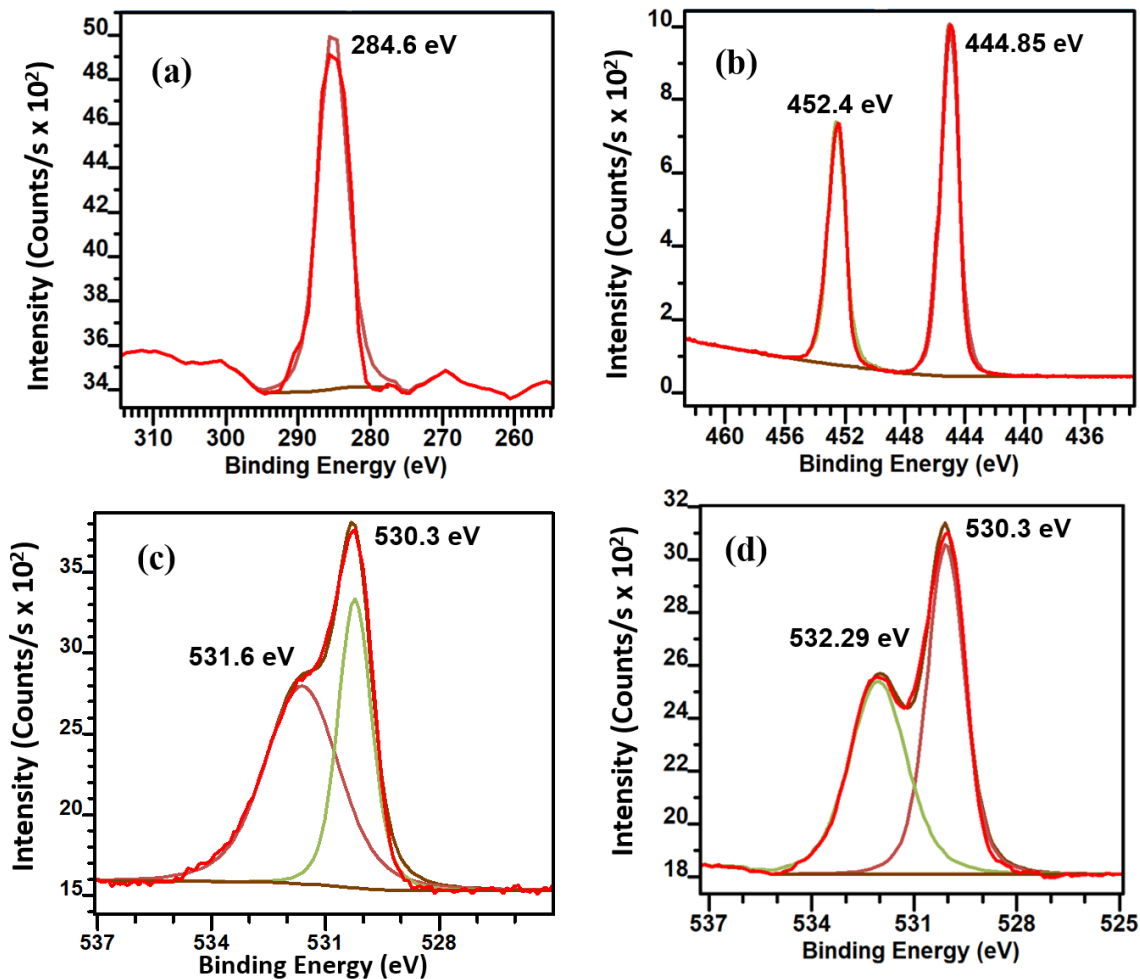


Figure 12: High resolution XPS spectrum of (a)-(d) C(1s), In (3d) and O(1s). O(1s) spectrum in figure 12(c) and 12(d) shows presence of a minor second peak at higher binding energy associated with chemisorbed oxygen species on the surface of the nanowires.

subtraction was performed using the Tougaard function. The atomic concentration of indium and oxygen were calculated to be 33% and 67% respectively providing evidence of a significant amount of chemisorbed oxygen species on the surface. The asymmetric O(1s) peak shown in figure 12(c) was deconvoluted using a Gaussian function and a reasonably good fit with the experimental data was obtained. Two peaks were required to fit the measured O(1s) spectra with resolved peak positions at 530.3 eV and 531.6 eV

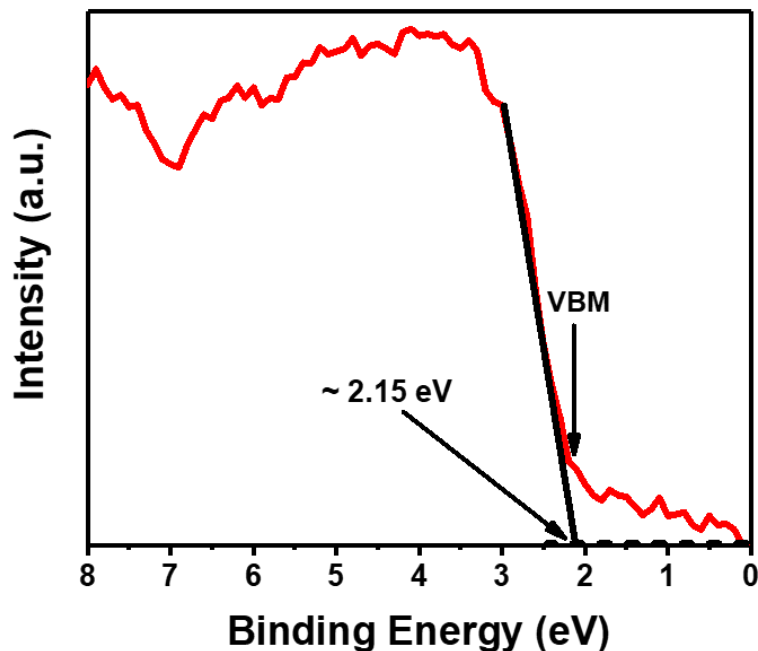


Figure 13: XPS valence band photoemission spectra of In_2O_3 nanowires. The separation between the VBM to surface Fermi level was calculated based on linear extrapolation of the leading edge of valence band photoemission spectra.

respectively. In figure 12(c), the feature at 530.3 eV is the lattice oxygen O^{2-} on the surface whereas the feature at 531.6 eV is believed to be from chemisorbed oxygen species [54, 55]. Occasionally we also observed a minor peak at 532.29 eV as shown in figure 12(d) due to the hydroxyl and/or oxy-hydroxyl oxygen species, possibly from water as the (111) and (011) surfaces in In_2O_3 are known to adsorb water and promote dissociation of molecules [42]. At high temperatures (> 200 °C), oxygen molecules dissociate into atomic form which can reside on the surface either as neutral $\text{O}_{(ads)}$ or charged $\text{O}_{(ads)}^-$ upon trapping an electron from the semiconductor [55]. Due to adsorbed species on the surface of the In_2O_3 nanowires, the surface Fermi level can vary by up to 1.5 eV depending on the sample preparation [56]. It is known that the combination of core level and valence band XPS constitutes a useful method of determining VBOs in a rather direct fashion [55]. The

VBM to surface Fermi level separation was determined to be 2.15 ± 0.2 eV as shown in figure 13 based on the linear method [56]. The value obtained for VBO is smaller compared to values reported in the literature mostly for thin-film samples [57] and could be attributed to upward band-bending due to negatively charged oxygen species residing on the surface. This puts the surface Fermi level below the CBM which makes the surface less n-type. The carrier concentration (n) is given by [58]

$$n = 2 \left[\frac{2\pi m_e^* K_B T}{h^2} \right]^{\frac{3}{2}} \exp\left(\frac{E_F - E_C}{K_B T}\right) \quad (2.4)$$

where $m_e^* = 0.3 m_0$ [46] is the effective electron mass. Taking $T = 300$ K, the net electron concentration at the surface was estimated to be $1.65 \times 10^{15} \text{ cm}^{-3}$. Hence, our XPS measurements confirm the presence of a high-density of V_O defects on the surface of the nanowires. Depending on the nature of the surface states in nanostructures, a strong influence on the optoelectronic [53, 59] and chemical sensing [55] properties can be observed. This has been further investigated using optical techniques as discussed in the next chapter.

2.3. Conclusion

This chapter discusses on the synthesis and growth mechanism of In_2O_3 nanowires using a carbothermal reduction process where the nanowire growth occurs through a Au-catalytic VLS route. Non-uniform diameter nanoparticles with octahedron like morphologies were found to grow when In metal was used as the precursor. Wulff shape construction was used to analyze the growth rates among various low indexed crystallographic planes which could lead to the formation of such morphologies. The nanowire samples were found to have an average diameter of ~ 100 nm and micron scale in length. TEM-EDX characterization revealed presence on Au catalyst on the tip and the

growth of the nanowires was determined from the HRTEM data to be along $\langle 100 \rangle$. SAED pattern reveals single crystalline properties however, Raman characterization and absorption measurements showed presence of high density of V_O defects present in the crystal lattice. The V_O defects were found to be mostly present on the surface of the nanowires which resulted in nanoscale faceting as well as adsorption of foreign oxygen derivatives leading to an upward band bending as confirmed using high resolution XPS and valence band measurements.

3. DEFECT CHARACTERIZATION USING OPTICAL TECHNIQUES AND INFLUENCE OF PASSIVATION TREATMENT ON In_2O_3 NANOWIRE PROPERTIES

(Portion of this chapter is copied from my published and unpublished manuscripts
Mukherjee S, Sarkar K, Wiederrecht GP, Schaller RD, Gosztola DJ, Stroschio MA, Dutta M. Defect induced structural inhomogeneity, ultraviolet light emission and near-band-edge photoluminescence broadening in degenerate In_2O_3 nanowires. *Nanotechnology*. 2018 Mar 1;29(17):175201.
Mukherjee S, Sarkar K, Wiederrecht GP, Gosztola DJ, Stroschio MA, Dutta M. Influence of surface states and passivation treatment on the carrier dynamics of In_2O_3 nanowires, *under preparation*.
Mukherjee S, Sarkar K, Wiederrecht GP, Gosztola DJ, Stroschio MA, Dutta M. Morphology dependent carrier dynamics in In_2O_3 nanostructures, *under preparation*.)

In (**Section 3.1**) is discussed on the commonly occurring V_O defects in In_2O_3 surfaces. The nature and position of the surface states were investigated using temperature dependent PL spectroscopy which shows broadened NBE emission even at very low temperatures indicating very high doping. A quantitative analysis of the doping concentration was performed based on the impurity band broadening model. Further, the role of surface states in carrier trapping which can lead to enhanced dielectric behavior in nanostructures was studied using ultrafast time-resolved transient absorption (TA) pump-probe spectroscopy. Next is discussed the effect of passivation treatments to tune the density of the surface states, by performing high temperature annealing. XPS characterization shows increased concentration of lattice oxygen atoms as well as negatively charged hydroxyl and/or oxy-hydroxyl oxygen species on the surface. Raman and PL characterization revealed significant improvement of the crystal quality which directly correlates with time-resolved measurements and shows large relaxation time constants of carriers following excitation in comparison to the as-synthesized nanowires indicating significant reduction in carrier trapping due to surface states.

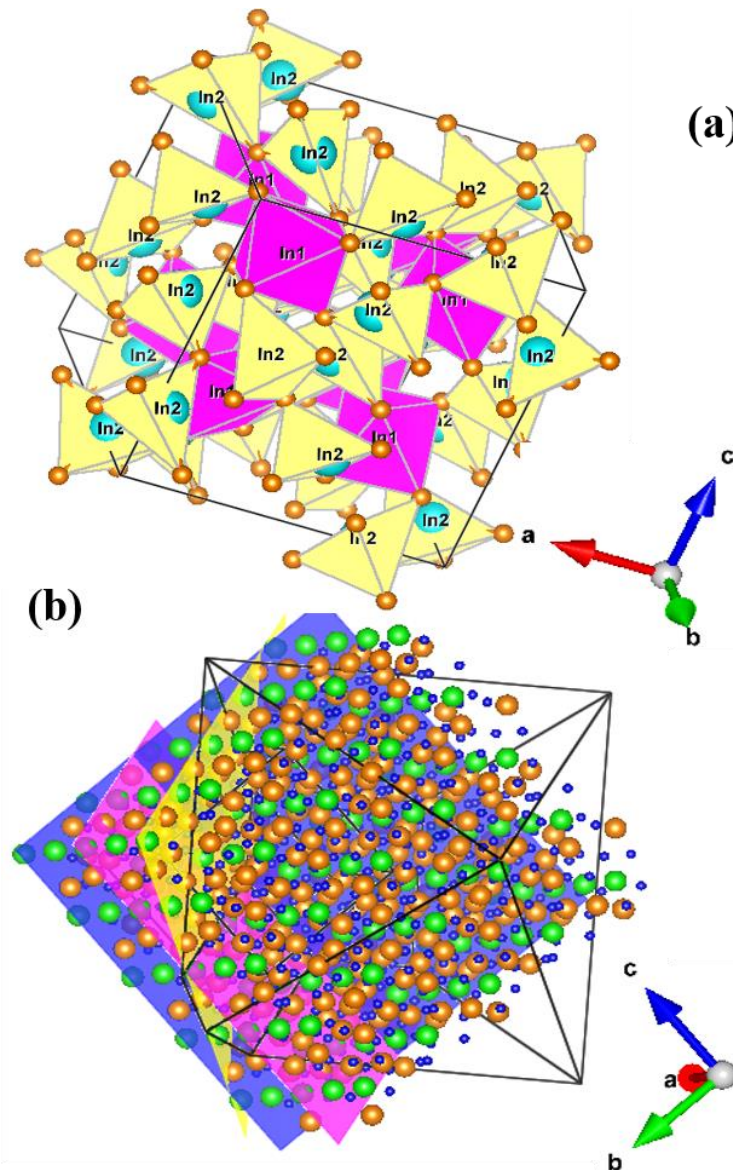


Figure 14: Structural visualization using VESTA of (a) the crystal structure of $c\text{-In}_2\text{O}_3$ where the In atoms are labelled with cyan and pink respectively, (b) octahedron morphology dominated by the $\{111\}$ surfaces.

3.1. Defects in In_2O_3

In_2O_3 is known to crystallize in three different phases belonging to the space group symmetries $I2_13$ (no. 199, cubic bixbyite structure), $Ia\bar{3}$ (no. 206, cubic bixbyite structure), and $R\bar{3}$ (no. 167, rhombohedral structure) respectively [60]. The stable phase

belonging to space group 206 has 8 formula units (f.u.) per unit cell (40 atoms in the primitive unit cell and 80 atoms in a conventional cell). Distinct from the first cubic bixbyite structure, it has different bond lengths and arrangements of atoms. It consists of two types of In atoms and one type of O atom which are located at Wyckoff positions 8b, 24d, and 48e, respectively [61, 62]. The two types of In atoms are surrounded by oxygen in the octahedral and trigonal prismatic coordinations alternatively, as shown in figure 14(a) [47]. It is well known that the most common defects occurring in nano- and polycrystalline oxides are oxygen vacancies which can significantly modify the band structure creating additional energy levels within the band gap itself [63]. These defects can exist in three different charge states. A neutral charge state (V_o^x) is formed when from an otherwise perfect crystal lattice, an oxygen atom is missing which leaves behind two electrons in a defect state which is a symmetric coordination of four In dangling bonds [61]. The singly ionized (V_o^+) state is when one electron has been captured and the (V_o^{++}) state is doubly positively charged relative to the lattice as it has not captured any electrons [64].

The structure of In_2O_3 surface has recently been addressed in a combination of computational and experimental investigation where the (111) terminated structure was found to be the lowest in energy and therefore under thermodynamic equilibrium, constitutes the most abundant crystal face [65]. Consequently, synthesis of nanostructures often results in the formation In_2O_3 nanoparticles with octahedron like geometry where the external morphology is dominated by the {111} planes as shown in figure 14(b). It has been recently demonstrated for In_2O_3 using density functional theory (DFT) calculations that due to lowering of the coordination environment, the energy required for the formation

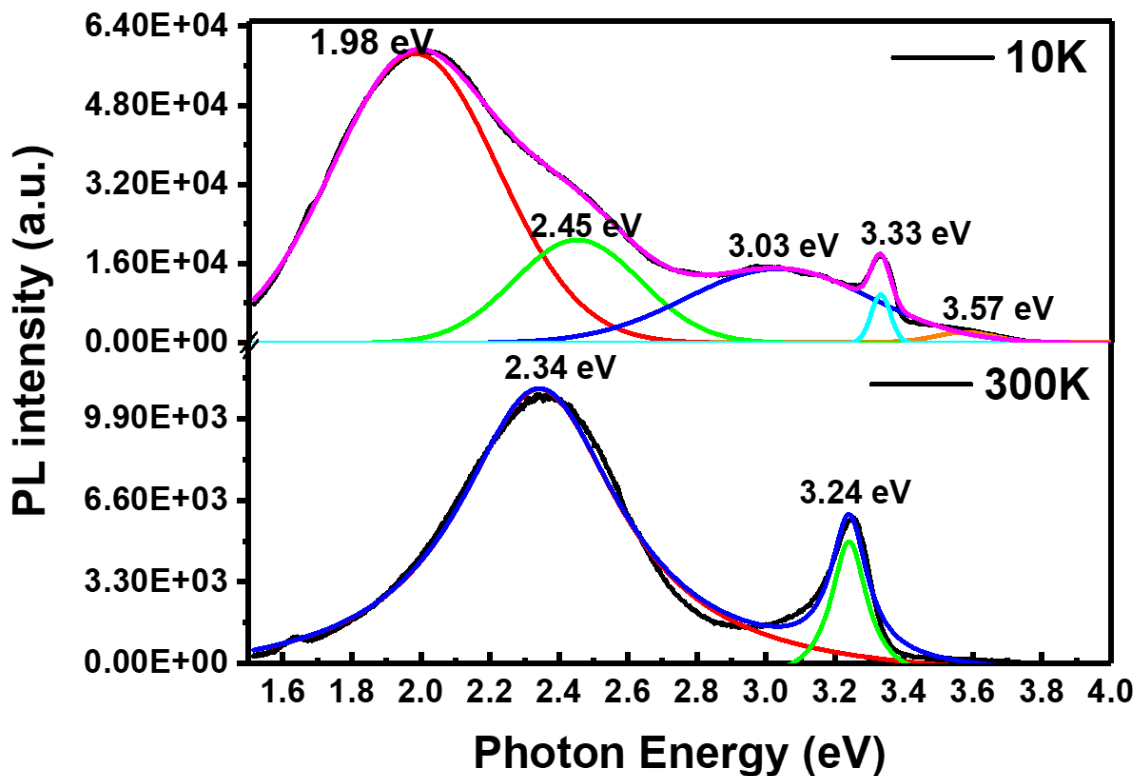


Figure 15: Low (10 K) and room temperature PL spectra fitted with multiple Gaussian peaks identifying corresponding transition energies.

of a V_o defect rapidly decreases towards the (111) surface [65, 66]. As a result, donors are produced at chemically reduced extended defects often resulting in an insulator-metal transition which is commonly observed in most metal oxide systems. We have experimentally demonstrated this behavior in In_2O_3 nanowires where we observed nanoscale faceting of {111} surfaces as well as adsorption of foreign atoms resulting in surface band bending [67]. High density of surface defects has been associated with enhanced dielectric behavior in oxide nanostructures thereby forming the basis for various sensing applications [55]. The nature and position of these surface states are further studied using various optical techniques.

3.1.1. Identification of nature and position of the defect levels due to surface states using photoluminescence spectroscopy

Figure 15 shows the PL spectrum in an extended wavelength range taken at 10 K and at room temperature. Both spectra show strong UV emission but an even stronger peak in the visible part of the spectrum can be observed. Let's first focus on the observed UV emission from In_2O_3 nanowires at room temperature which has been rarely reported [39, 41, 68]. It is interesting to note that the observed NBE peak centered at 3.24 eV at room temperature is a broad peak with full width at half maximum (FWHM) of ~ 160 meV and does not get resolved into expected narrow emission peaks even at very low temperatures as can be observed from the 10 K spectra. To the best of our knowledge, this type of observation has not been reported before for In_2O_3 . The origin of the NBE peak is believed to be from a series of shallow donor levels formed due to V_o^x defects present on the surface of the nanowires [41]. Broadened NBE emission with no excitonic emission features even at very low temperatures is clearly an indication of very high doping which causes the discrete shallow donor levels to merge into an impurity band. The feature at 3.57 eV arises due to the presence of a weak fluorescence background signal from the quartz coverslip on which the nanowires were transferred for low temperature PL measurements. Control measurements were performed on the substrate and subtracted from the overall spectra that does correct most if not all the background features which can be due to experimental fluctuations. In the experimental setup, we have utilized a 320 nm long pass filter to block the tail of the 290 nm excitation. The effect of the filter can be observed from the 10 K spectra in figure 15 where the background signal at ~ 3.8 eV (320 nm) and higher energies goes down to zero whereas at energies lower than 3.8 eV, a weak

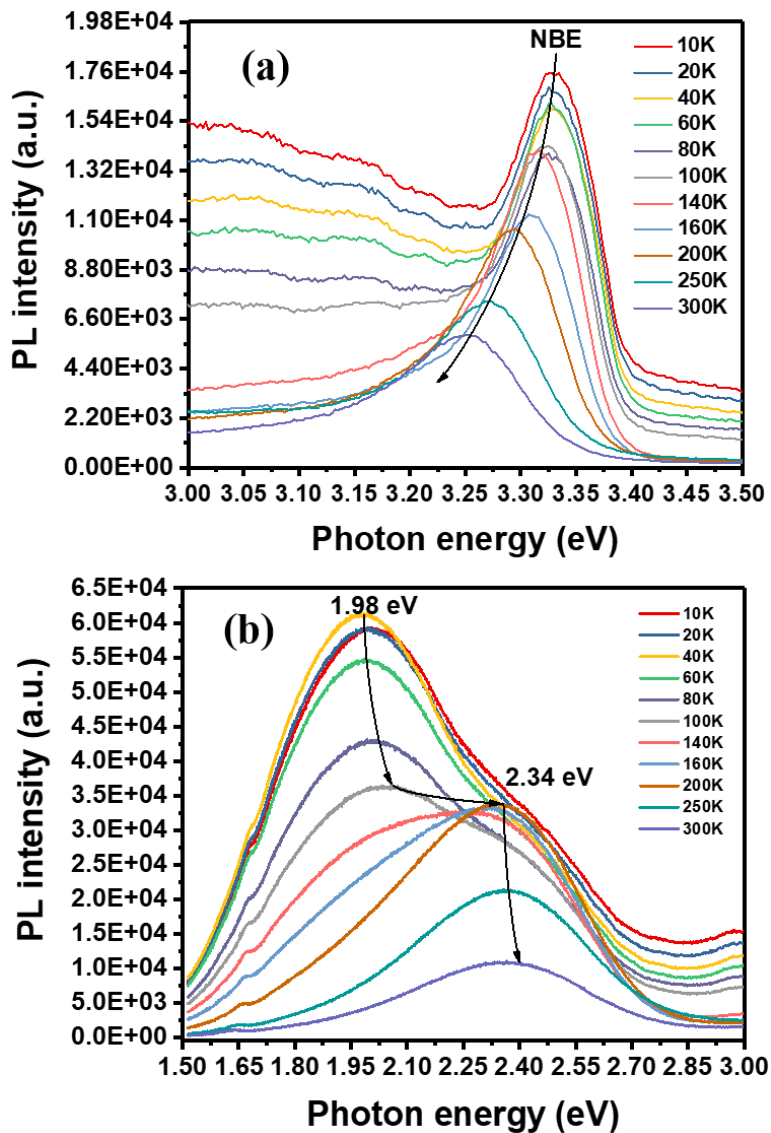


Figure 16: Temperature dependence of the PL (a) NBE and (b) below band edge spectra in In_2O_3 nanowires.

fluorescence from the substrate persists creating an impression of a broad Gaussian peak like feature. The fitting function identifies this feature as an additional peak while performing deconvolution of the overall spectra to extract individual components and associated peak positions.

Figure 16(a) and figure 16(b) shows the temperature dependent PL spectrum (10 K–300 K) of the NBE and midgap defect peaks. The intensity of the broad NBE peak decreases progressively with increasing temperature and shows a characteristic red-shift of 90 meV at room temperature relative to the 10 K spectra and merges into a broader peak possibly due to phonon scattering effects. From the 10 K spectra in figure 15, we also observe an emission peak centered at 3.03 eV, which is below the band-edge and appears to have merged with the NBE peak at temperatures above 140 K. The below band edge peak at 3.03 eV is believed to originate from donor levels formed due to V_O^+ defects. It can be observed from figure 17(a) that the high energy edge of the NBE peak defined as 1% of the peak intensity point decreases monotonically with increasing temperature and can be described by the well-known Varshni equation [69].

$$E(T) = \left[E(0) - \frac{\alpha T^2}{T + \beta} \right] \quad (3.1)$$

where $E(0)$ is the excitonic band gap at 0 K, and α , β are the corresponding fitting parameters. A good fit was obtained (red curve) with the experimental data (black squares) and the value of $E(0)$ was found to be 3.41 eV which can be considered as the lower bound of the optical gap and is in close agreement with previously reported values for highly n-type In_2O_3 nanostructures [41]. The extracted fitting parameters $\alpha = 3.507 \times 10^{-4}$ eV/K and $\beta = 140 \pm 20$ K are consistent with previously reported values by Wei *et al.* [60]. A smaller value of the parameter β [69] indicates in general poor lattice thermal conductivity of the nanowires and has previously been observed for highly doped n-type semiconductor [70]. However, most literature reports have shown doped materials to have high thermal conductivity and thus our observation calls for further investigation. From the temperature

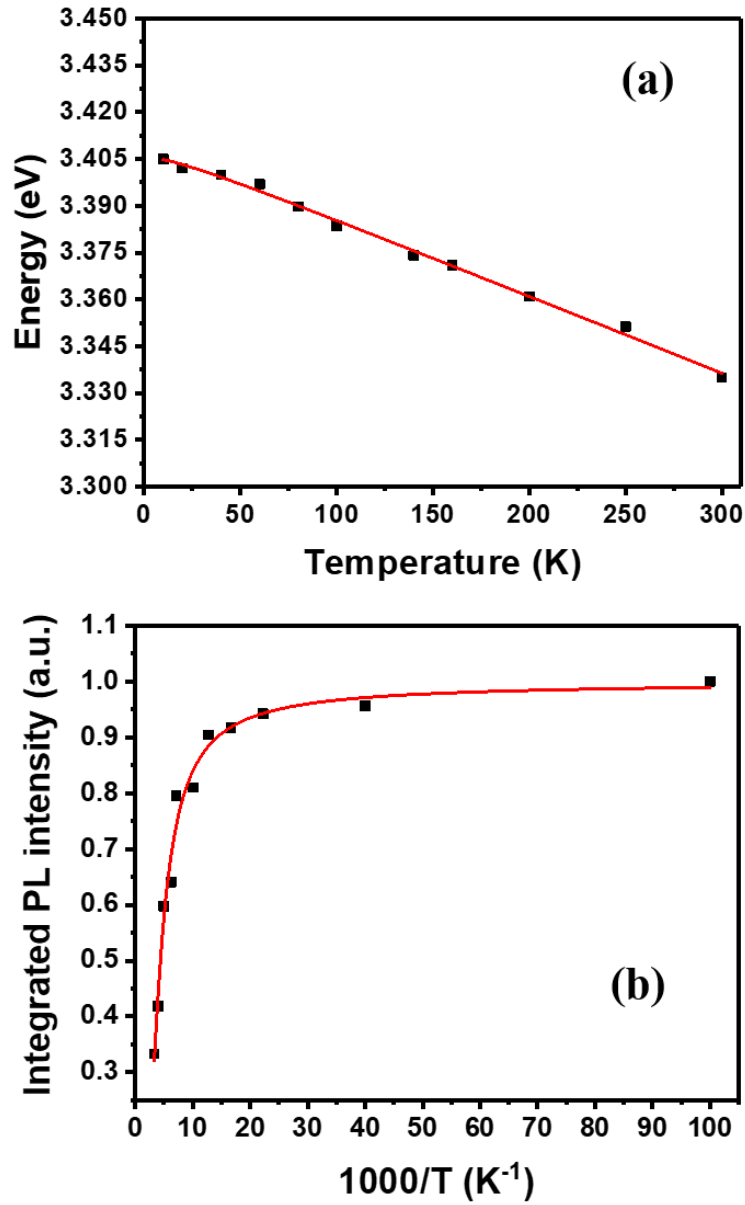


Figure 17: (a) Temperature dependence of the high energy edge of the NBE peak. (b) Thermal quenching behavior of NBE peak.

dependence of the NBE peak, we estimate the nature of the quenching channels present as shown in figure 17(b) which is described by the modified Arrhenius equation: [37]

$$I(T) = \left[\frac{I(0)}{\left(1 + A_1 \exp\left(-\frac{E_1}{k_B T}\right) + A_2 \exp\left(-\frac{E_2}{k_B T}\right)\right)} \right] \quad (3.2)$$

where, $I(T)$ and $I(0)$ are the PL intensities at temperature T and 10 K, respectively; E_i is the activation energy, K_B is the Boltzmann constant, and A_i is a constant. By using a two-channel fit and considering both A_1 and A_2 constants, we found E_1 and E_2 to be 6 meV and 75 meV, respectively. These correspond to effective ionization energy of donors and acceptor like states respectively. The acceptor like states may be a series of shallow oxygen-indium vacancy pairs (V_O-V_{In}) or deeper indium vacancies (V_{In}) which act as compensating centers [41] and can significantly contribute towards defect emissions from below the band-edge resulting in broad visible emission peaks centered at 2.45 eV and 1.98 eV in the 10 K PL spectra. Due to thermal ionization effects at higher temperatures, these peaks ultimately merge into a single broad peak centered at 2.34 eV as observed from the temperature dependent PL spectra in figure 16(b).

3.1.2. First observation of near-band-edge photoluminescence broadening due to heavy doping

The Burstein-Moss effect and impurity band broadening are the two proposed mechanisms for such modified NBE emission spectrum [71]. The Burstein-Moss effect is a result of band edge shift to higher energies when doping exceeds the degeneracy limit ($\sim 2.5 \times 10^{19}$ for In_2O_3) and is frequently observed in heavily-doped semiconductors whereas impurity band broadening occurs because of potential fluctuations due to randomly distributed impurities which can cause discrete donor levels to evolve into impurity bands ultimately leading to a band tail. For heavily doped samples, the FWHM predicted by the Burstein-Moss model is expected to be significantly higher than what we observe here (~ 95 meV at 10 K) [71]. We also do not observe a sharp cutoff on the high energy side of the NBE peak which is the characteristic of momentum non-conserving indirect transitions

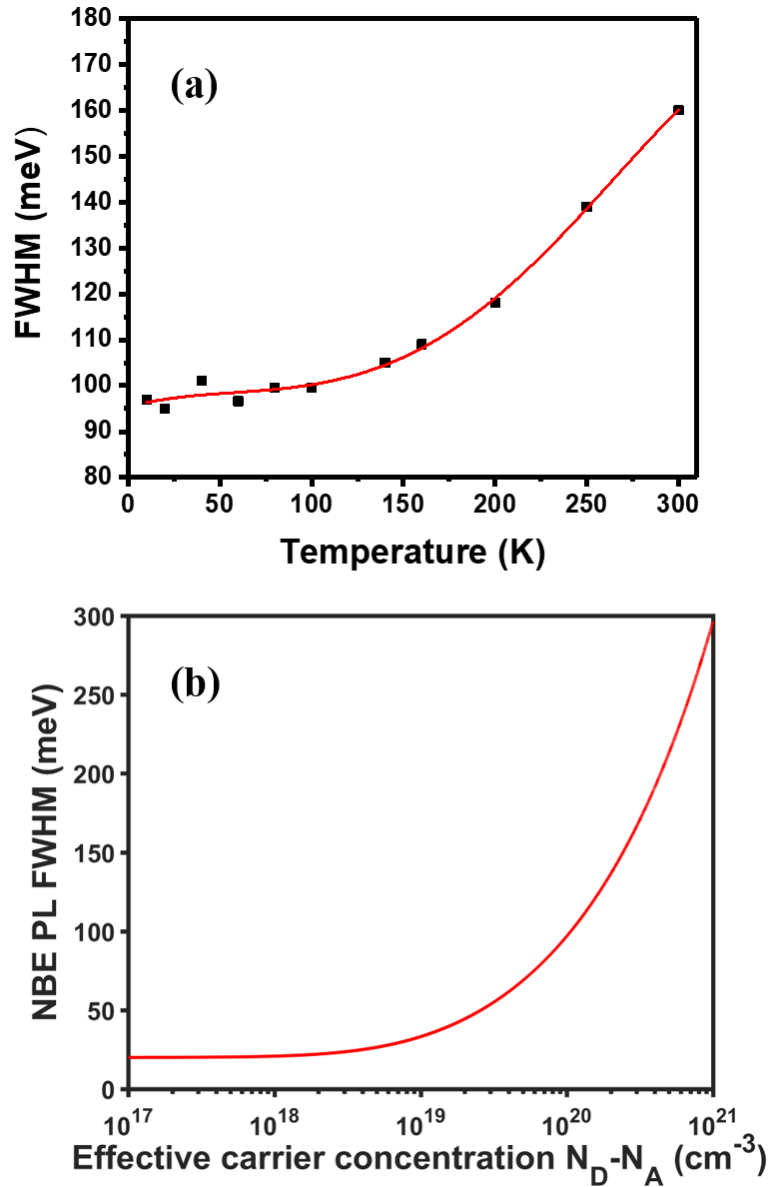


Figure 18: (a) Dependence of NBE peak FWHM on temperature. (b) NBE PL line width as a function of effective carrier concentration based on the impurity band broadening model.

[72] which leads us to believe that broadening of the impurity band plays a major role in the observed PL. The width of the band tails, and thus the dependence of the NBE peak line width on carrier concentration, can be calculated based on the impurity band broadening model proposed by Morgan *et al.* [73].

Figure 18(a) shows the FWHM of the NBE peak as a function of temperature, where the red curve is a guide to the eyes. V_o^x defect levels expand into a defect band which overlaps with the conduction band thereby shifting the edge to the low energy side and a band tail is formed [74]. The FWHM of the PL line width can be expressed as [71]

$$FWHM = \left[\Gamma_T^2 + \left(2^{\frac{3}{2}} \ln 2 \sigma_i \right)^2 \right]^{\frac{3}{2}} \quad (3.3)$$

Γ_T is the broadening due to thermal and lattice disorder (typical ~20 meV) and can be ignored in this case. σ is the second moment of the Gaussian-shaped potential fluctuation distribution function [71] and is given by,

$$\sigma^2 = \left[C_1 c n^{\frac{5}{6}} \exp \left(-C_2 \sqrt{\frac{2}{c+1}} n^{-\frac{1}{4}} \right) \right]^{\frac{3}{2}} \quad (3.4)$$

where $c \sim 1$ is the compensation ratio, n is the net electron concentration and C_1 and C_2 are constants as derived by Ilipoulos *et al.* [75]. We thus estimate an electron concentration of $1.2 \times 10^{20} \text{ cm}^{-3}$ at 10 K and the corresponding plot of equation (3.3) is shown in figure 18(b). The calculated electron concentration is higher than the degeneracy limit in In_2O_3 , hence the In_2O_3 nanowires were found to be degenerate with Fermi level lying ~0.05 eV above the CBM. A representative schematic of the flat-band structure, probable energy transitions and the effect of band tailing in In_2O_3 nanowires is shown in figure 19(a) whereas figure 19(b) shows representative upward band bending (~0.51 eV) on the surface of the nanowires due to presence of chemisorbed oxygen species. Absorption occurs from the valence band to the Fermi level whereas luminescence occurs from the band tail to acceptor like states. Similar observations of remarkable PL broadening have previously been observed for n-GaN films [75] and indium doped n-type ZnO nanowires [71].

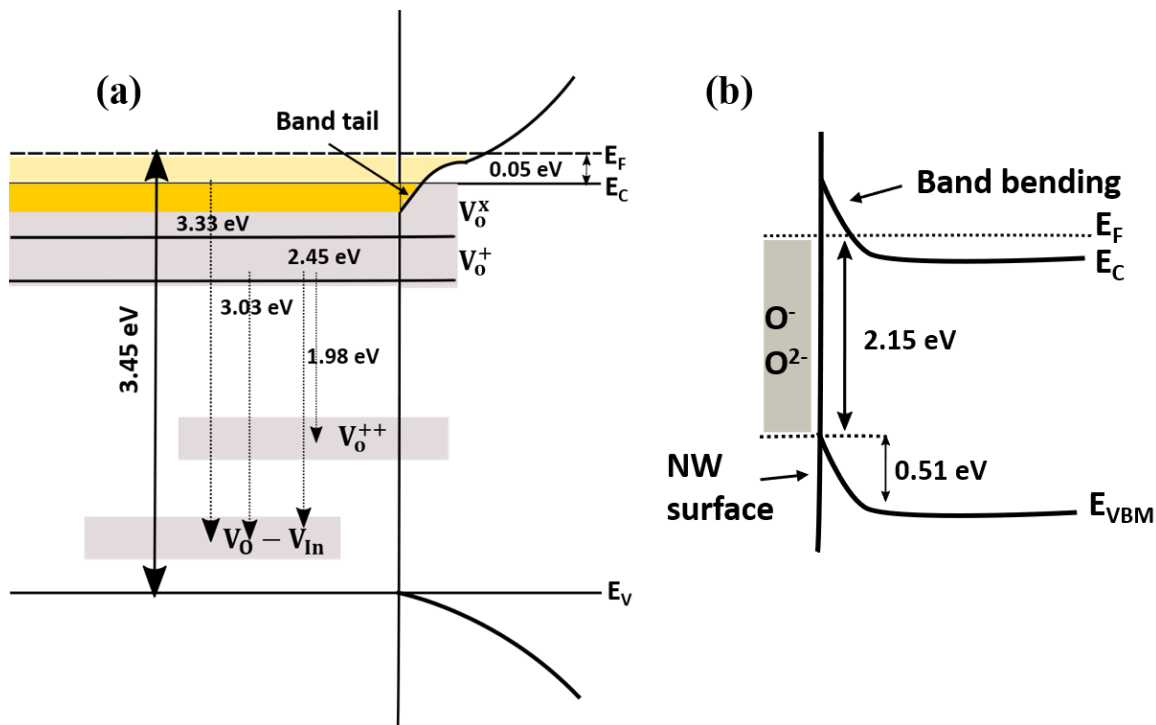


Figure 19: (a) Schematic band diagram of In₂O₃ nanowires showing energy transitions due to different charge states of V_O defects and band tailing effect. (b) Upward band bending on the surface due to chemisorbed oxygen species.

3.1.3. Ultrafast pump-probe spectroscopy to study the carrier trapping rates due to surface states

The influence of surface states in carrier trapping has been studied using ultrafast TA spectroscopy based on a pump-probe technique. TA spectroscopy is an extension of absorption spectroscopy which measures the absorbance at a range of wavelengths of a sample following excitation by a short light pulse. Generally, an intense femtosecond laser pulse is used as the ‘pump’ to excite carriers within the sample into a non-equilibrium state. The pump-induced changes are then measured by a weak ‘probe’ pulse as a function of time delay in between the pump and probe beams. The recorded data is usually represented as normalized differential absorption or transmission given by [76]

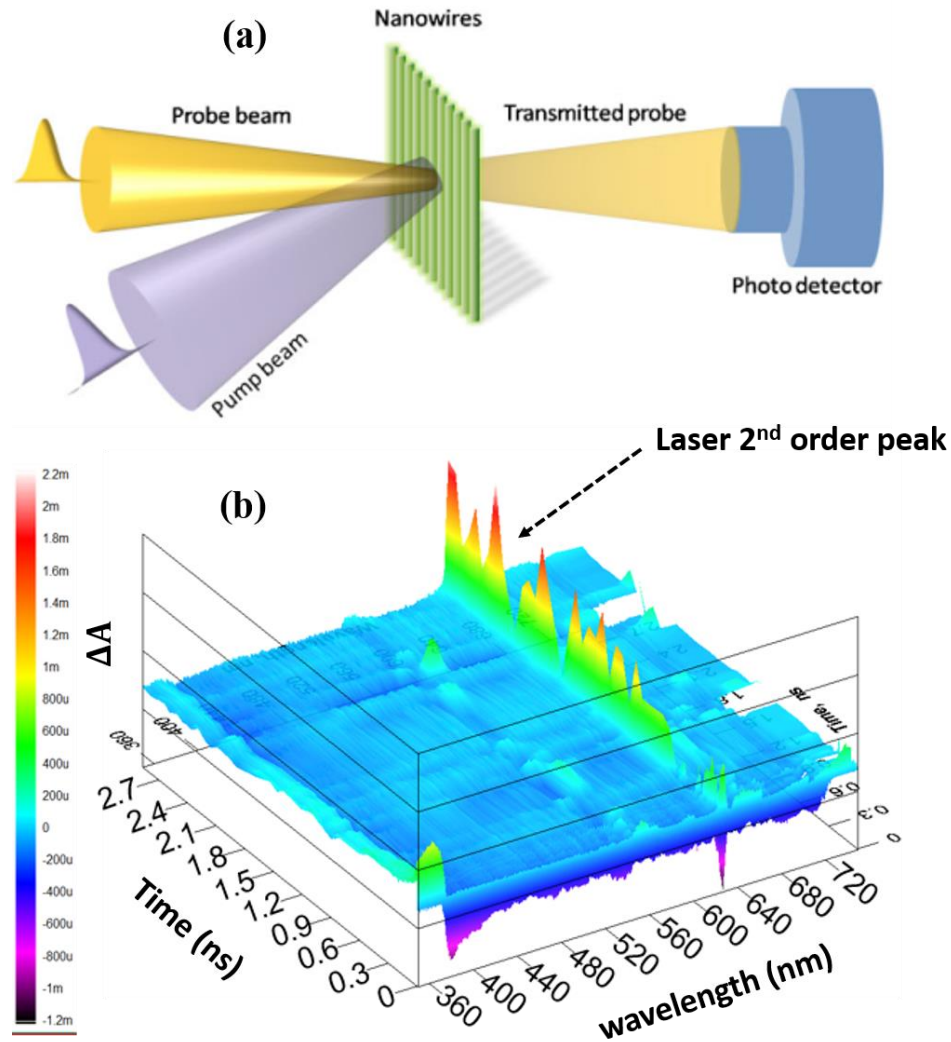


Figure 20: (a) Schematic showing the pump-probe measurement in transmission mode on a semiconductor nanowire sample [76]. (b) 2D surface plot of the ΔA spectra as a function of probe wavelength and time delay in between pump and probe.

$$\frac{\Delta T}{T_0} = \left[\frac{(T_E - T_0)}{T_0} \right] \quad (3.5)$$

where, T_0 and T_E represents the probe pulse transmission in the absence and presence of the pump pulse respectively. Therefore, while there is no pump pulse present, only the linear transmission of the sample is measured by the probe pulse. Cross-correlation between the pump and probe pulses spatially overlapping on the sample ultimately

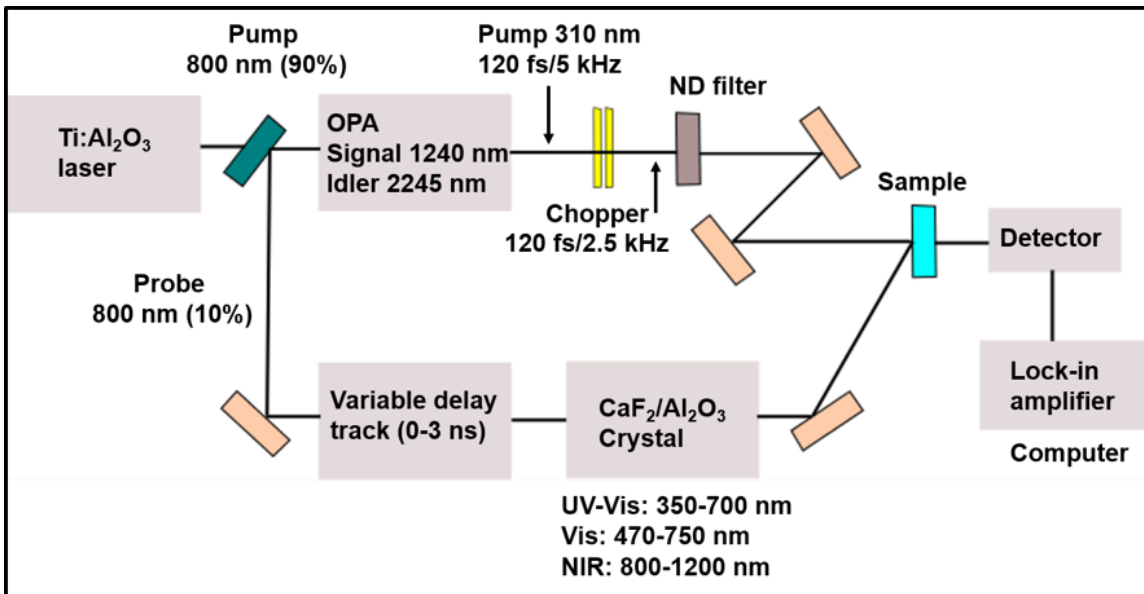


Figure 21: Experimental setup of the ultrafast TA pump-probe spectroscopy system having a pump wavelength of 310 nm (tunable) and optical probe in the wavelength region 350–700 nm.

determines the temporal resolution of the system. A schematic representation of the pump-probe technique is shown in figure 20(a). Figure 20(b) shows a representative 2D surface plot after background subtraction where the differential absorption ($\Delta A = 1 - \Delta T$) spectrum is plotted on the vertical axis.

The experimental setup is shown in figure 21. A 120 fs pulse at 800 nm was produced by a regenerative amplification process using a Ti:sapphire (Al_2O_3) laser system (SpitFire Pro low power pulse/800 nm/120 fs/ 75 MHz and Newport Tsunami – high power pulse/800 nm/100 ns/5 kHz) with a repetition rate of 5 kHz. In the regenerative amplification process, the low power pulse is dispersed (stretched) by a factor of thousands for safe amplification by a pair of grating. Using an optical switch (polarizer), the low and high-power pulses are trapped inside a cavity until the low power pulse is adequately amplified by extracting the energy stored in the gain medium. A second pair of grating

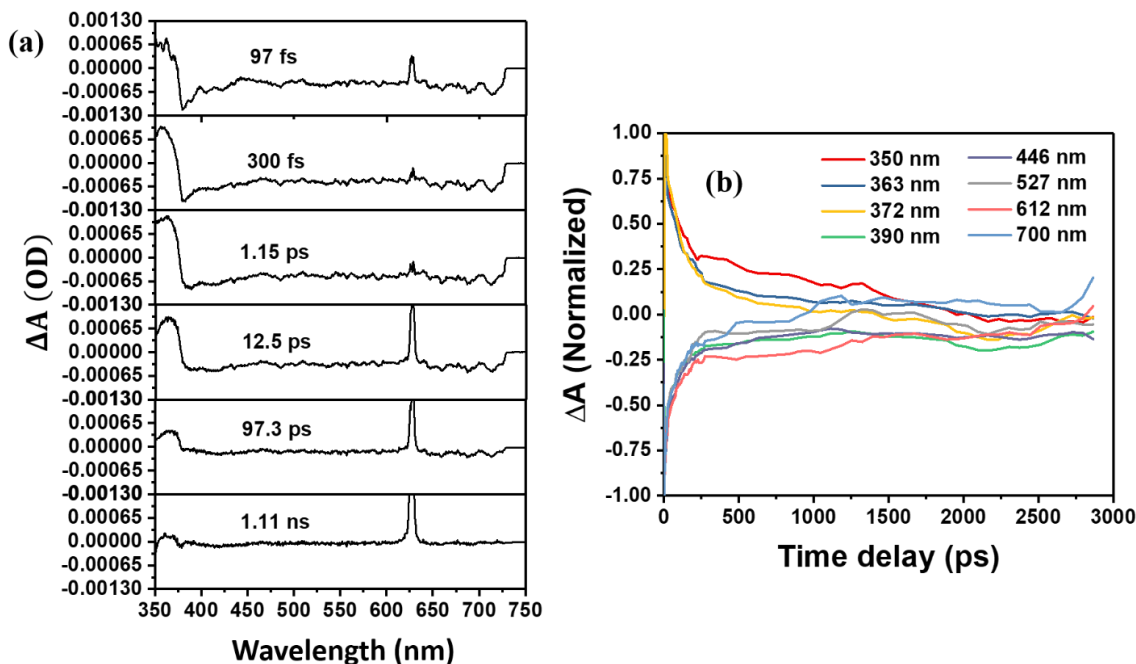


Figure 22: (a) Shows ΔA spectra at various time delays following the 310 nm pump excitation where both probe induced absorption and state-filling could be observed. (b) corresponding carrier kinetics at various probing wavelengths.

recompresses the pulses which are now high power and of ultrashort duration. The intense light pulse is split into two components, 90% of which is used to drive an optical parametric amplifier (OPA) that generates a 120 fs pulse at 310 nm thereby serving as the pump beam. The remainder of the amplified beam is passed through a variable delay track (0–3 ns) and is used to excite a calcium fluoride (CaF_2) crystal to generate a white light continuum having wavelength from 350–750 nm. This white light continuum acts as the probe pulse, fluence of which is <10% of the pump. A mechanical chopper synchronized with the regenerative amplifier was used to modulate the pump pulse at 2.5 kHz [8]. This ensures that the spectrometer alternatively measures the probe transmittance in the presence (T_E) and absence (T_0) of the pump pulse respectively. The pump and the probe pulses were focused

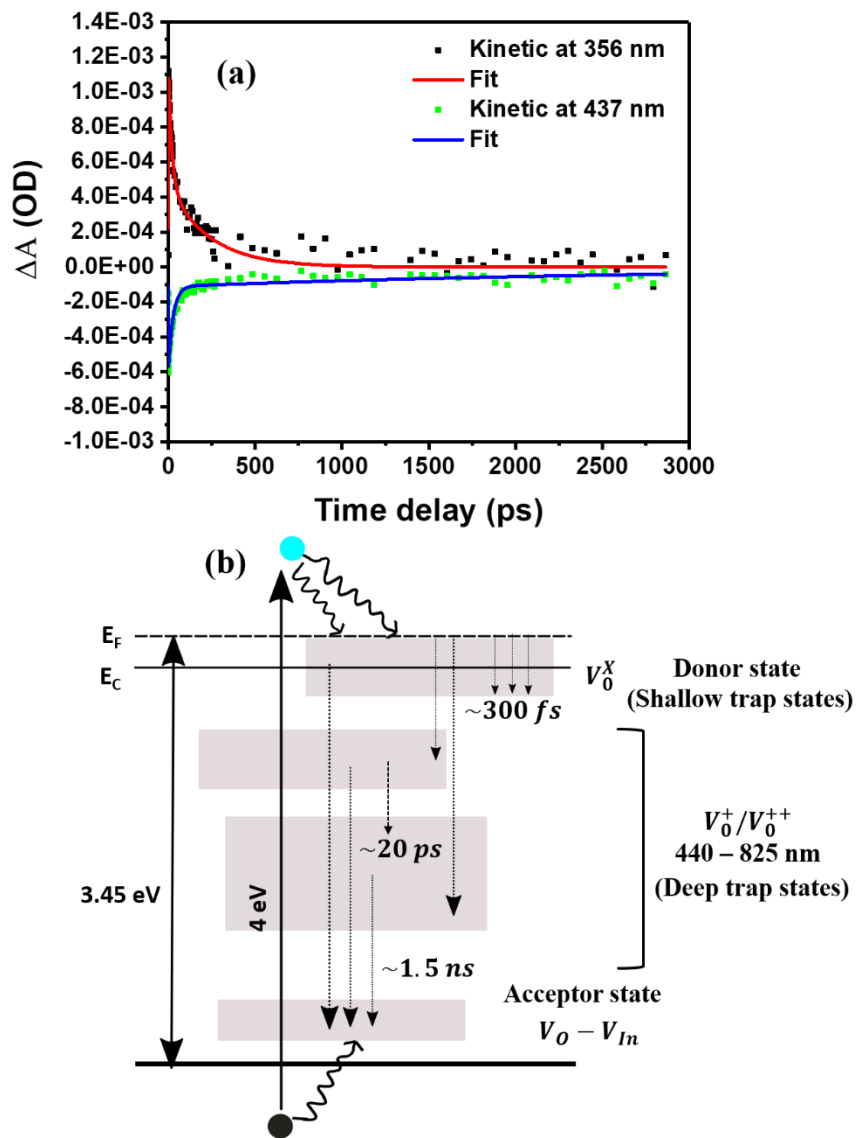


Figure 23: (a) Carrier kinetics at above band edge (356 nm) and midgap states with corresponding fits showing bi-exponential decay profile where the initial fast component (~ 20 ps) is associated with carrier trapping by lower lying defect levels due to surface states and the longer component (~ 1.5 ns) is attributed to electron-hole recombination process. (b) schematic representation of associated carrier relaxation processes.

onto the sample using macro optics for them to spatially overlap. All measurements were performed under ambient conditions.

TA measurements were performed on as-synthesized In_2O_3 nanowires using optical excitation at 310 nm and different probing wavelength in the UV-Vis region. Figure 22(a) and figure 22(b) shows the differential absorption spectra and kinetics at various time instances and probe wavelengths respectively following excitation. We observed complex behaviour over the entire probing spectral range. In some cases, especially near the conduction band edge, positive change in the ΔA spectra was observed due to secondary carrier excitation to higher energy states by the probing pulses. Negative change in the ΔA spectra could be observed throughout the midgap states due to occupation of energy levels by photogenerated carriers which is otherwise known as state filling. Throughout the probing wavelengths, we observed both effects to be present, while the dominant effect ultimately determines the sign. It is well known that above band gap excitation will generate free carriers in the conduction and valence band respectively which would occupy states resulting in state-filling. Thus, state-filling is expected to be the dominant mechanism at energy levels higher than the band gap as has been previously observed for In_2O_3 nanocrystals [77] and nanowires [78]. However, this behaviour is not observed in our as-synthesized nanowires. The band gap of our as-synthesized In_2O_3 nanowires is 3.41 eV [67] and near the band edge, the dominant effect was observed to be probe induced secondary carrier absorption determined by the carrier density in the initial states and interband coupling coefficient [78]. As observed from figure 22(a), the defect levels due to surface states within the band gap are bleached within 300 fs after excitation. We observed two competing process to occur thereafter where (a) the carriers move out of the shallow defect levels and subsequently gets trapped by the underlying deep level traps

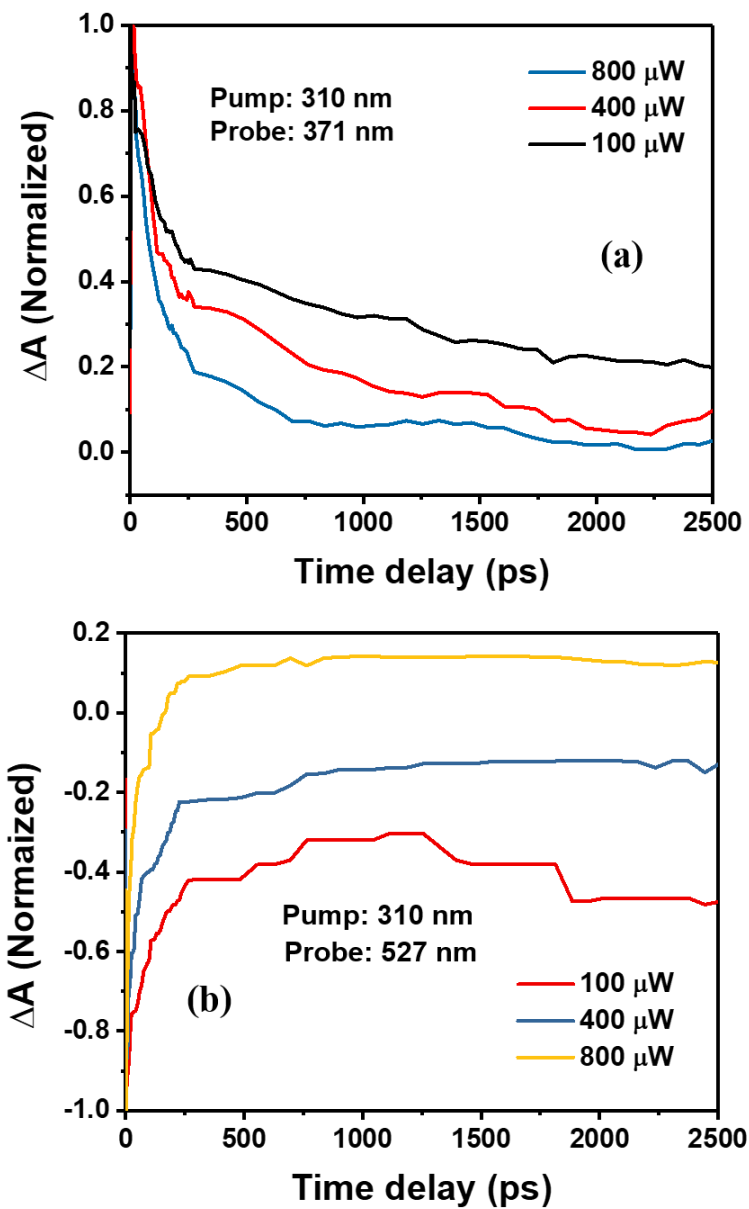


Figure 24: (a)-(b) Pump fluence dependent kinetics at two different probe wavelengths near the band edge and midgap states showing influence of hole trapping at the surface due to adsorbed oxygen species.

within the midgap states and (b) carriers recombine with holes from the valence band localized in acceptor trap states.

The carrier kinetics at various probe wavelengths above and below the band gap as shown in figure 22(b) were fitted with biexponential decay functions to extract the carrier relaxation time constants. The raw data and corresponding fit at two probe wavelengths is shown in figure 23(a), where a fast component of 10–40 ps and a slow component of 500 ps–2.8 ns could be observed. The initial fast component could be assigned to the phenomenon where carrier trapped in the defect levels move out and subsequently gets trapped by underlying defect states and has been previously observed in defect induced SnO₂ nanowires [79, 80]. The longer time constant is believed to be due to relaxation of carriers towards equilibrium where they recombine with holes producing UV and visible luminescence as confirmed previously using PL measurements [67]. A schematic representation of various defect levels at the nanowire surface and proposed relaxation pathways are shown in figure 23(b).

Pump fluence dependent kinetics as shown in figure 24(a) and figure 24(b), shows faster carrier relaxation with increasing pump fluence. Different mechanisms can be responsible for such behaviour. The as-synthesized nanowires were found to have high density of surface V_o defects which caused chemisorption of oxygen and formation of a space charge layer where the holes were trapped near the surface to maintain overall charge neutrality in the nanowires [55]. The negative electric field spatially separates electrons and holes at the surface of the nanowires. It is well known that photodesorption occurs on the nanowire surface upon excitation with UV light [64, 55]. This leads to a reduction of the surface electric field. As a result, with increasing pump fluence, the photodesorption process is significantly enhanced leading to faster recombination of electrons and holes. This type of behaviour has previously been observed in as-synthesized SnO₂ nanowires

TABLE I: CHARACTERISTICS OF PHONON MODES IN In_2O_3 NANOWIRES BEFORE AND AFTER THERMAL ANNEALING TREATMENT SHOWING DISTINCT INCREASE IN THE PEAK INTENSITY AS WELL AS REDUCED BROADENING POST TREATMENT.

Phonon mode	Samples	Area under the phonon peaks (a.u.)	Peak intensity (a.u.)	FWHM (cm^{-1})
T_g mode at 110 cm^{-1}	As-grown	10689.196	1873.647	4.171
	Annealed	12883.895	2622.036	3.436
T_g mode at 119 cm^{-1}	As-grown	2285.926	835.665	3.472
	Annealed	2823.588	991.851	3.179
A_g mode at 133 cm^{-1}	As-grown	46518.298	8472.482	3.478
	Annealed	60018.376	11007.24	3.321
T_g mode at 154 cm^{-1}	As-grown	4725.522	809.634	5.825
	Annealed	5689.835	1043.912	4.93
E_g mode at 172 cm^{-1} (weak)	As-grown	357.9	533.66	3.55
	Annealed	411.98	578.06	3.26
Overlap modes at 307 cm^{-1} ($2T_g, A_g, E_g$)	As-grown	83700.847	6091.473	9.386
	Annealed	110344.928	7851.151	9.504
T_g mode at 365 cm^{-1}	As-grown	24656.815	2243.763	9.518
	Annealed	33259.762	2699.2	9.988
A_g mode at 495 cm^{-1}	As-grown	25251.203	2077.048	10.904
	Annealed	31343.033	2477.301	10.762
T_g mode at 628 cm^{-1}	As-grown	13790.633	1370.86	9.994
	Annealed	13817.408	1448.039	9.086

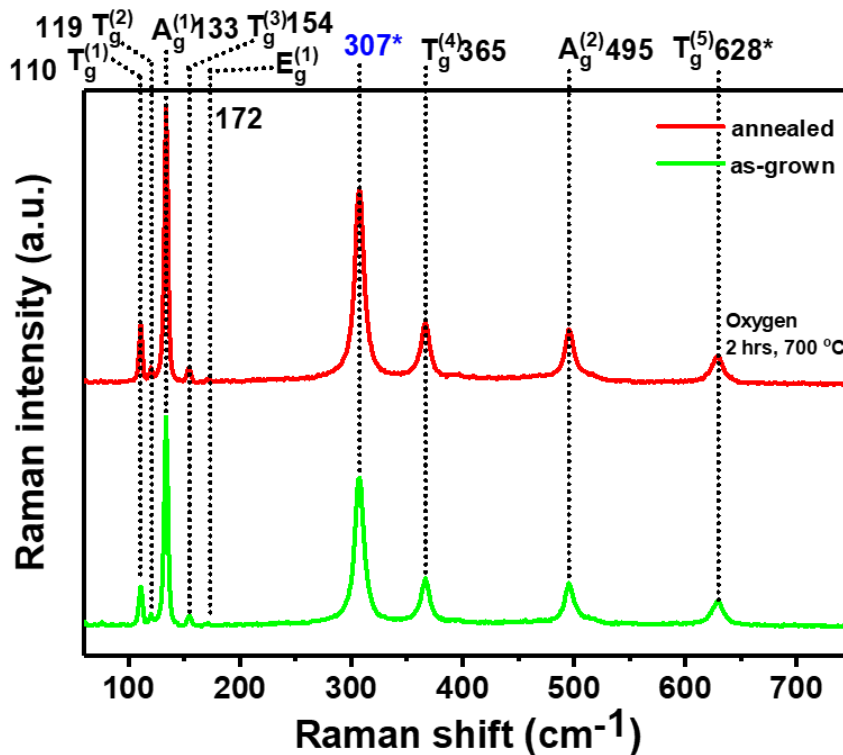


Figure 25: Comparison of non-resonant Raman spectra before and after annealing at 700 °C for 2 hrs in an oxygen rich environment.

[55]. Unlike the data reported by Kar *et al.* [55] here we observed distinct changes in the pump fluence dependent relaxation kinetics when probing near the band edge and midgap states due to the presence of very high density of surface defects.

3.2. Effect of passivation treatment on the nanowire properties

Due to large surface to volume ratio in nanostructures, surface and near-surface defects and adsorbates offers alternative relaxation pathways for carriers following excitation as demonstrated under subsection 3.1.3. Thus, carrier transport in semiconductors are often dominated by surface and interface states which can create unexpected high mobilities in nanoscale silicon-on-insulator (SOI) structures [80] or enhanced carrier trapping in oxide [81] and nitride [76] based nanostructured devices. Carrier trapping by surface defects

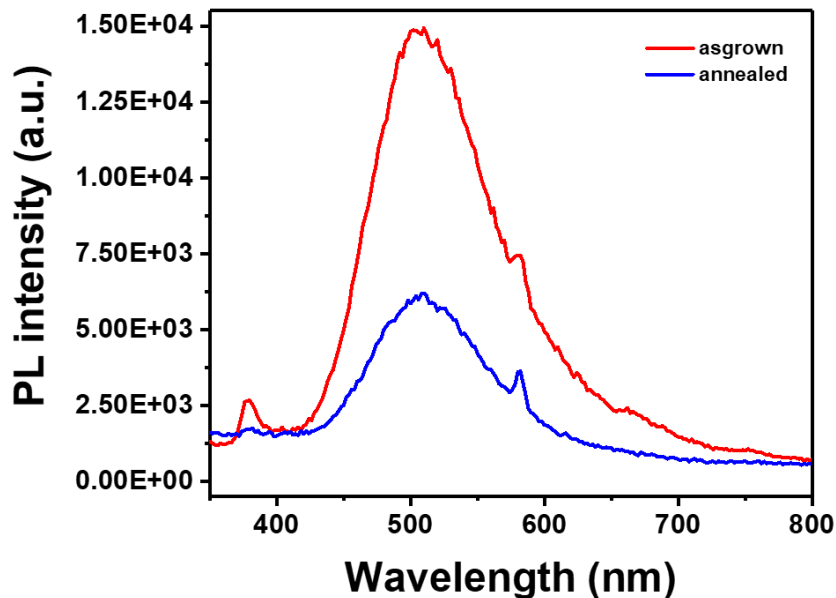


Figure 26: Room temperature PL spectra showing significant reduction of defect emissions post annealing treatment at 700 °C for 2 hrs in an oxygen rich environment.

such as vacancies and dangling bonds are prone to polarization in an EM field thereby contributing to the nanostructure dielectric properties [19]. Post-synthesis of the nanostructures, thermal annealing treatments in an oxidizing or reducing environment can be used to tune these intrinsic defects thereby modifying the surface states which can be exploited for various chemical sensing purposes [55]. Here, we have investigated the change in the nanowire properties post thermal annealing treatment in an oxygen rich environment.

3.2.1. Comparison of nanowire structural and luminescence properties post thermal annealing treatment

It is well known for oxide semiconductors that high temperature annealing (> 400 °C) can significantly improve the crystal quality due to reduction of vacancy clusters whereas low temperature annealing may provide some relaxation at the interfaces but is

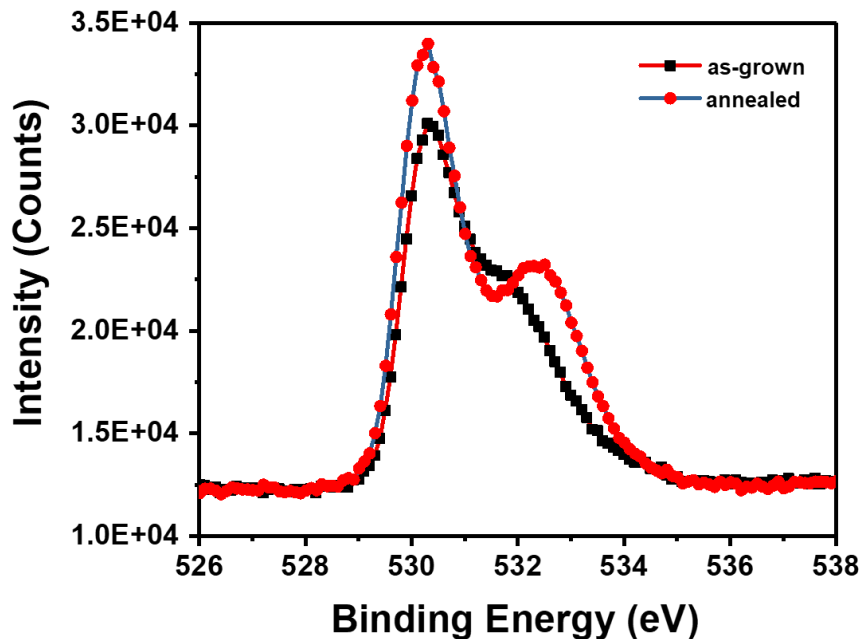


Figure 27: High resolution XPS spectra of O(1s) peak before and after high temperature annealing showing increase in the lattice O^{2-} peak and adsorbed charged oxygen species.

unable to remove any lattice disorders [82]. The as-synthesized samples were annealed at 700 °C for 2 hrs under constant flow of 300 sccm of oxygen in a KSL-1100X high temperature muffle furnace. Figure 25 shows the Raman spectra of In_2O_3 nanowires pre and post thermal annealing treatment. We do not observe any change in the phonon frequencies which lies within the experimental errors ($<1\text{ cm}^{-1}$) or asymmetric broadening as no phonon confinement effect is expected due to relatively larger diameter of the nanowires. However, we do see an increase in the peak intensities of the phonon modes as well as reduction in the FWHM post thermal annealing treatment as reported in table I. Figure 26 shows the room temperature PL spectra of the sample excited by a 290 nm wavelength from a Xenon lamp before and after thermal annealing treatment which shows

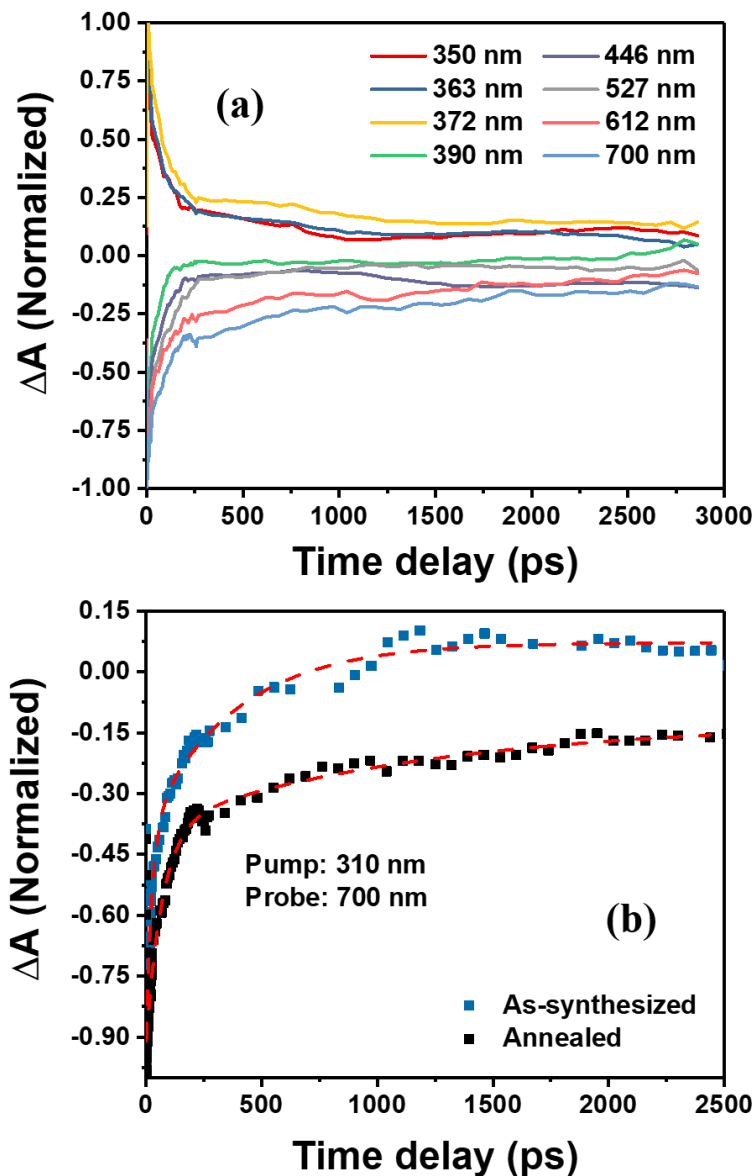


Figure 28: (a) TA kinetics of In_2O_3 nanowires post thermal annealing treatment and (b) comparative kinetics of as-synthesized and treated nanowires showing significant increase in the carrier relaxation time post treatment.

significant reduction of the NBE and visible luminescence peaks arising out of different V_o defects.

TABLE II: EXTRACTED CARRIER RELAXATION TIME CONSTANTS AND RELATIVE AMPLITUDES FROM THE FITTED DATA OF AS-SYNTHEZIZED AND ANNEALED SAMPLES AT 700 NM PROBE WAVELENGTH AND 300 μ W PUMP POWER. THE AMPLITUDE OF THE FAST DECAY COMPONENT REDUCES SIGNIFICANTLY POST THERMAL ANNEALING TREATMENT THEREBY CONFIRMING SIGNIFICANT REDUCTION IN THE TRAP CENTERS. FURTHER THE LONG DECAY COMPONENT ASSOCIATED WITH CARRIER RECOMBINATION IS FOUND TO BE DRASTICALLY INCREASED DUE TO HIGH DENSITY OF ADSORBED OXYGEN SPECIES ON THE SURFACE CREATING A STRONG SURFACE DIPOLE.

Sample	τ_1 (ps)	A_1 (%)	τ_2 (ps)	A_2 (%)
As-grown	22.81	57	303.8	43
Annealed	53.5	37.8	3860	62.2

3.2.2. Modification of nanowire surface properties post thermal annealing treatment

We performed XPS analysis on the as-grown and annealed samples and the comparative plots of the high-resolution O(1s) peak is shown in figure 27. A clear increase in the lattice oxygen O²⁻ peak at 530.3 eV on the surface is observed along with an increase in the hydroxyl and/or oxy-hydroxyl oxygen species occurring at 532.29 eV. Increase of the 532.29 eV peak indicates water adsorption possibly present in the surrounding environment [83]. These hydroxyl and/or oxy-hydroxyl oxygen species are bound to In atoms thereby forming strong surface dipoles [84]. To further confirm the reduction of the density of surface states, we performed time resolved measurements on the annealed samples as shown in figure 28(a). Two components were needed to fit the kinetics as we have previously observed for as-synthesized samples. However, relative to the as-synthesized samples, we observed significant increase in carrier relaxation time constants

following excitation as shown in figure 28(b) and the values are reported in table II. The decrease of the carrier trapping rates clearly signifies that post thermal annealing treatment, less number of defects are present and as a result, it takes longer time for the carriers to get trapped.

3.3. Conclusion

In summary, the defects present in In_2O_3 nanowires particularly V_o defects on the surface and its influence on the nanowire properties were studied using optical techniques. The nature and position of the defect levels were identified using temperature dependent PL spectroscopy. We observed UV emission from the band-edge and significant NBE PL line width broadening associated with formed V_o^X impurity band at the surface which merges with the conduction band forming a band tail. The optical gap was calculated to be 3.41 eV and activation energies of 6 meV and 75 meV were obtained and related to ionizing energies of donor and acceptor like defects respectively. An electron concentration of $1.2 \times 10^{20} \text{ cm}^{-3}$ at 10 K was estimated which is above the degeneracy limit of In_2O_3 , hence positioning the Fermi level 0.05 eV above the CBM.

The influence of the surface states in carrier trapping was studied next using ultrafast time resolved TA spectroscopy based on a pump-probe technique. Ultrafast TA measurements reveals that the shallow and midgap states are bleached within 300 fs following excitation. Thereafter, two competing processes dominate while the carriers relax towards equilibrium. A faster component of ~ 20 ps associated with carrier trapping by underlying defect levels and a slow component of ~ 1.5 ns was attributed to recombination of electron-hole pairs. Pump-fluence dependent measurements reveals significant hole trapping at the surface due to surface states. With increasing fluence,

carriers were found to relax faster towards equilibrium due to rapid photodesorption. Finally, the effect of passivation treatment by performing high temperature annealing at 700 °C for 2 hrs in an oxygen rich environment on the nanowire properties were studied. The crystal quality was drastically improved as evident from the comparative Raman and PL spectra. XPS results revealed increase in the concentration of lattice oxygen atoms post thermal annealing revealing the surface states have been modified. Time-resolved measurements showed a slow recovery towards equilibrium further indicating that the carrier trapping process has been significantly reduced. Thus, we show here that high temperature thermal annealing could be used to tailor the surface properties of In_2O_3 nanowires which could be used in an effective way towards chemical sensing applications.

4. MILLIMETER WAVE STANDOFF MEASUREMENTS OF IONIZING RADIATION IN REAL-TIME USING In_2O_3 NANOWIRES AS SENSOR

MATERIAL

(Portion of this chapter is copied from my unpublished manuscript Mukherjee S, Sarkar K, Elmer TW, Bakhtiari S, Gopalsami N, Koehl ER, Stroschio MA, Dutta M. Stand-off detection of ^{137}Cs γ -radiation using In_2O_3 nanowires based on a millimeter wave technique, *under preparation*.)

The present work provides a method and system of performing standoff measurements of ionizing radiation using millimeter wave technology by interrogating changes in the dielectric properties of a co-existing tag which is covertly or overtly placed within the target environment. This method is based on an alternate detection architecture where the detector and signal read-out electronics are decoupled as opposed to the conventional ionization [85] or scintillation type detectors [86] and therefore has the potential to perform long-range measurements. The sensor material in this case belongs to the family of oxide semiconductor nanostructures which has recently been demonstrated as efficient γ -radiation detector [87]. Here we have utilized surface passivated In_2O_3 nanowires as the detection element. **(Section 4.1)** provide a background on various types of ionizing radiation, challenges associated with direct detection of microwave-millimeter scattering due to ionization induced changes in the background atmosphere and interaction of γ -radiation with semiconductor material. Subsequently in **(section 4.2)**, we discuss on the design and implementation of a 94 GHz portable low power transceiver for targeted standoff measurements of ionizing radiation. A 12'' lens antenna has been used for targeted detection purposes having a spatial resolution of $\sim 1\lambda$ at the focal point as shown using COMSOL simulation. We present our experimental observations under **(section 4.3)** where

we at first investigated the detection concept by utilizing a NIG and observed the mechanism of diffusion charging to be occurring on the nanowire surface thereby resulting in increased transmission of the millimeter waves. Various embodiments of detection scheme are presented here. Finally, we present preliminary results regarding the very first standoff detection of ^{137}Cs γ -radiation by recording changes in the scattered signal intensity due to irradiation defects created in surface passivated In_2O_3 nanowires.

4.1. Background

There has been considerable amount of work utilizing EM waves to remotely track weather and earth resources such as oil and minerals. Another area of interest is to remotely detect radiation from nuclear or radiological sources which is theoretically possible as ionization of air caused by these radiation events can modulate radar reflectivity and has been previously explored to detect radioactive plumes from nuclear power plants [22, 88]. Experimental demonstration includes, a Russian X-band radar which was able to successfully detect radioactivity at the 1986 Chernobyl accident site [89]. Despite these experimental demonstrations, the underlying physics is not well established and further these efforts could not be successfully reproduced [90]. As a result, these results are not well acknowledged within the scientific community.

Differing from these initial experimental correlations, it has been found that existing simple plasma models under-predict the radar cross section (RCS) by several orders of magnitude. In addition to the lack of understanding surrounding the correlation between radioactivity and RCS, current radiation detectors based on air sampling (e.g. ionization counters, scintillators, and semiconductors) are not effective from long distances because of dilution and atmospheric dispersion. For example, a typical Geiger–Muller counter

might be able to measure 1 milliCurie (mCi) of Cobalt-60 (^{60}Co) having a γ -radiation energy of 47 keV, with a resolution of $\sim 1 \text{ mSv h}^{-1}$ at a maximum distance of $\sim 3.5 \text{ m}$ away from the source. Specifically, the limited range of conventional detectors is because of small penetration lengths of alpha and beta particles in air and a decrease of neutrons and γ -rays with the inverse of the square of the distance from the source. Consequently, such systems are limited to a detection range of approximately 100 meters.

In recent efforts, a South Korean team of researchers were able to remotely detect radioactivity by inducing plasma breakdown using high power pulsed EM radiation [28]. However, the maximum focal location is limited by air turbulence and depending upon this condition, the detection range can significantly vary from 50 m to 1 km. Thus, although the impact of radiation on EM waves in air has been generally understood, there is a need for a method and system for utilizing such a relationship without the need for close proximity to the radiation, i.e. a true standoff detection mechanism. In this regard, an alternate strategy was proposed by a team of researchers from Pacific Northwest National Laboratory (PNNL) which discusses on covertly or overly placing a sensor tag near the source and interrogate changes in its EM properties as a function of radiation dosage remotely using a microwave-millimeter wave radar [91, 92]. Changes in dielectric permittivity, magnetic permeability, or electrical conductivity and their effects on resonant cavities were thus explored. The resonant cavity circuit was envisioned as being remotely placed on a radio-frequency identification (RFID) tag, near a radioactive source that was desired to be monitored remotely. Microwave or low millimeter wave EM radiation would be used to interrogate the device through a simple power reflection change or other more sophisticated designs.

4.1.1. Microwave and millimeter wave scattering due to radiation induced air ionization

Atoms consist of relatively large particles comprised of protons and neutrons, orbited by negatively charged electrons. Under normal circumstances, atoms consist of equal numbers of protons and electrons, so the atom is neutrally charged. An ion is any atom or molecule that does not have the normal number of electrons, which means it is not neutrally charged. Ionizing radiation has sufficient energy to kick electrons out of the atoms, thereby creating free electrons and ions. Radiation, specifically ionizing radiation, will result in changes to air that is contacted by the same. Put differently, the radiation-induced ionization of air consists of a progression of mechanistic steps, from the formation of (a) plasma to (b) molecular aerosols to (c) microdroplet clouds. Previous work has investigated and estimated the RCS of these models where the molecular aerosol and microcloud droplet model were found to work only under highly humid and saturated environmental conditions. Under ambient conditions, the plasma model provides measurable RCS at radiowave to low microwave frequencies for electron plasma. Considering the plasma to be ‘cold’ which assumes that only a fraction of the gas molecules are being ionized, the plasma wave equation is given by

$$\gamma^2 = -\epsilon_r \frac{\omega^2}{c^2} \quad (4.1)$$

where γ is the complex propagation constant ($\gamma = \alpha + j\beta$), α being the attenuation constant and β is the phase coefficient, ω is the oscillation frequency and ϵ_r is the complex dielectric constant of cold collisional plasma

$$\left[(\epsilon_r - 1) = \left(\frac{\omega_e^2}{\omega^2 + f^2} + \frac{\omega_i^2}{\omega^2 + f^2} \right) - \frac{j}{\omega} \left(\frac{\omega_e^2 f}{\omega^2 + f^2} + \frac{\omega_i^2 f}{\omega^2 + f^2} \right) \right] \quad (4.2)$$

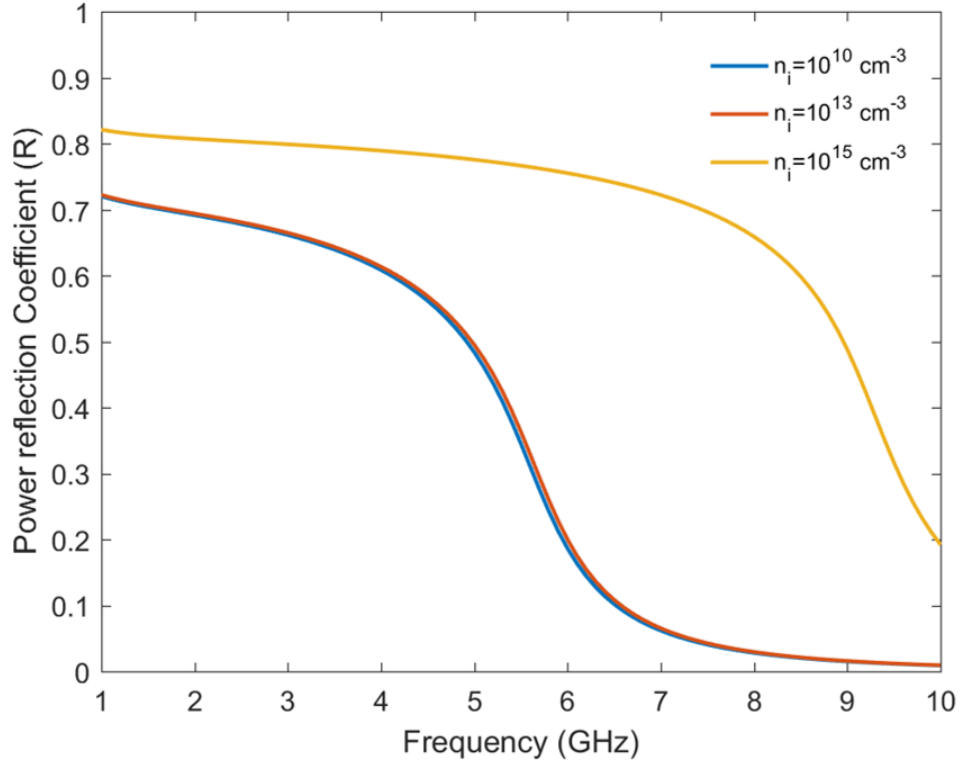


Figure 29: Microwave reflection from a semi-infinite plasma medium for different ion density values.

f being the collision frequency, ω_e and ω_i are frequencies of electrons and ions plasma respectively. $\omega_{e,i} = \sqrt{\left(\frac{n_{e,i}e^2}{\epsilon_0 m_{e,i}}\right)}$ are the Langmuir plasma frequencies where $n_{e,i}$ represents electron and ion densities, $m_{e,i}$ represents electron and ion masses, e is electron charge and ϵ_0 is the permittivity of free space. Hence for a semi-infinite plasma medium, the power reflection coefficient (PRC) at normal incidence can be written as

$$R = \left| \frac{1 - \sqrt{\epsilon_r}}{1 + \sqrt{\epsilon_r}} \right|^2 \quad (4.3)$$

The RCS for an incident beam of area $A = \pi a^2$ is related to the PRC as,

$$RCS = A * PRC = \frac{AP_r}{P_i} \quad (4.4)$$

where P_i and P_r are the incident and reflected power. Since the ions are heavier than electrons, the plasma frequency due to ions are much lower than that of electrons and hence has negligible contribution on the PRC and hence the RCS. This is evident from figure 29 where the PRC is plotted showing negligible change even for very high ion densities considering typical values of $n_e = 10^{10} \text{cm}^{-3}$ and $f = 10^9 \text{s}^{-1}$. However, the plasma cloud effects are not sustainable, because free electrons in the air produced by the radioactive sources quickly attach to the O_2 molecules. Further, for targeted detection, where spatial resolution is a key factor, smaller incident beam area would lead to even lower RCS values. Hence, standoff detection of radiation induced air ionization solely based on scattering events are less likely to produce measurable changes in the microwave-millimeter wave signal.

4.1.2. Interaction of γ -radiation with semiconductor material

Depending on the source strength and energy level, nuclear radiation in the form of α , β or γ rays ionizes the air, creating a certain amount of ion pairs/ cm^3/s that particulate matter sticks to in an effect similar to static electricity. γ -radiation typically have frequencies above 10^{19} Hz, are photons emitted from an unstable nucleus with energies in the (\sim KeV/MeV) range depending on the source and almost always less than 10 MeV [93]. Since they are not particles, unlike α or β radiation, they can travel long distances from the source typically losing only half of its energy per 150 meters. For narrow beam of γ -radiation, the decrease of intensity with material thickness generally follows an exponential decay curve. However, for wider beams, absorption is drastically reduced due to scattering from the side surfaces and is written as $I_d = I_0 e^{-\mu d}$, where $\mu = n\sigma$ is the absorption coefficient measured in cm^{-1} , σ the absorption cross section in cm^2 , n is the number of

atoms per cm^3 in the material, and d is the material thickness in cm. Compton scattering, photoelectric effect and pair production are the three main processes by which γ -radiation ionizes while passing through matter.

The photoelectric effect occurs when a γ -photon ejects an electron out of an atom because of energy transfer mechanism. The resulting kinetic energy of the electron is equal to the energy difference in between the incident γ -photon and the electron binding energy. This process is mainly dominant for energies less than 50 keV. Compton scattering on the other hand, is believed to be the most dominant interaction mechanism for γ -photon energies > 50 keV to 10 MeV. In this process, at first the incident γ -photon loses most of its energy to eject an atomic electron while the rest of the incident photon energy is remitted in the form of a secondary lower energy γ -photon where it has a different emission direction relative to the incident γ -photon. For very high energies of γ -photon (> 1.02 MeV), pair production can become a dominant mechanism where interaction occurs with electric field of a nucleus ultimately resulting in the formation of two γ -photons with each having at least 0.51 MeV of energy.

4.2. Experimental setup

4.2.1. Compact continuous wave homodyne 94 GHz transceiver design for standoff detection

A fieldable test setup is illustrated in figure 30. A millimeter wave sensor at 94 GHz measures radiation-induced changes in the sensor material at short standoff distances. A Gunn diode oscillator generates 94 GHz continuous millimeter wave radiation at a power level of ~ 100 mW. An isolator can be added to shield the input equipment. A 20 dB directional coupler transmits 99% percent of the millimeter wave power which is radiated

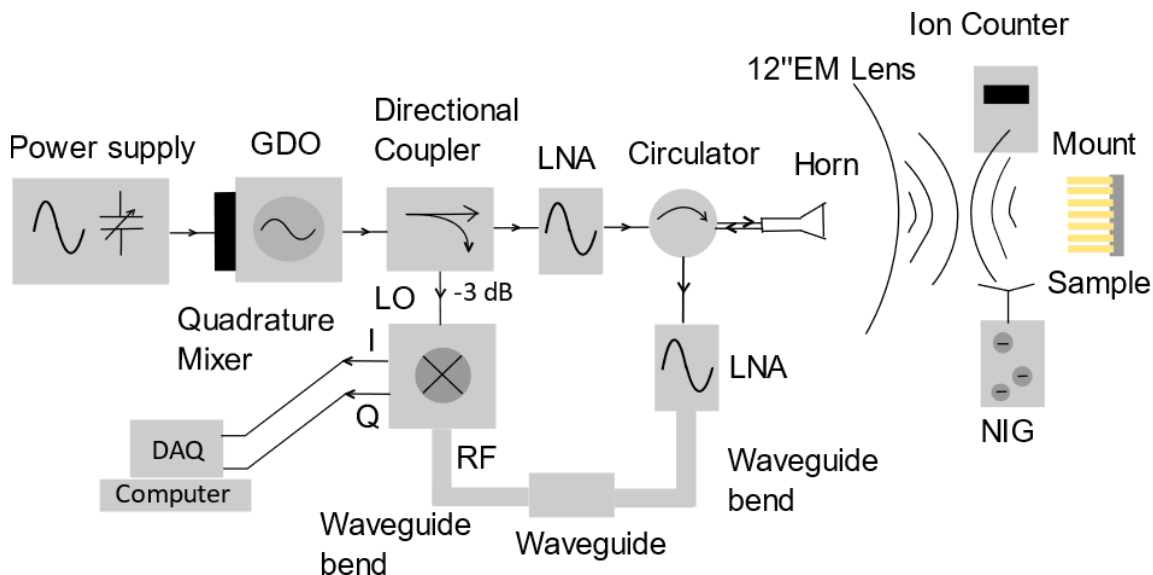


Figure 30: Schematic representation of the low power 94 GHz transceiver for targeted stand-off measurements of ionizing radiation effects on the nanowire samples.

out by a 12" lens antenna and directed at the target. The remaining 1% of the power is fed to the reference channel of a homodyne mixer. A 94 GHz circulator is used at the output such that it enables the reflected signal from the target to be collected by the same lens antenna. The received signal is amplified using a low noise amplifier and fed to the measurement channel of the homodyne mixer. A processing component, such as a computer, was used for signal analysis and processing. The target signal is converted into in-phase (I) and quadrature-phase (Q) components with respect to the reference signal. The I and Q components of the target signal may be used to measure amplitude and phase of backscattered signals from the target as well as Doppler frequency shift if the target is moving relative to the millimeter wave beam. All data were acquired through 4 channel 24 bit acquisition board from National Instruments. Figure 31 shows the experimental setup and all relevant components.

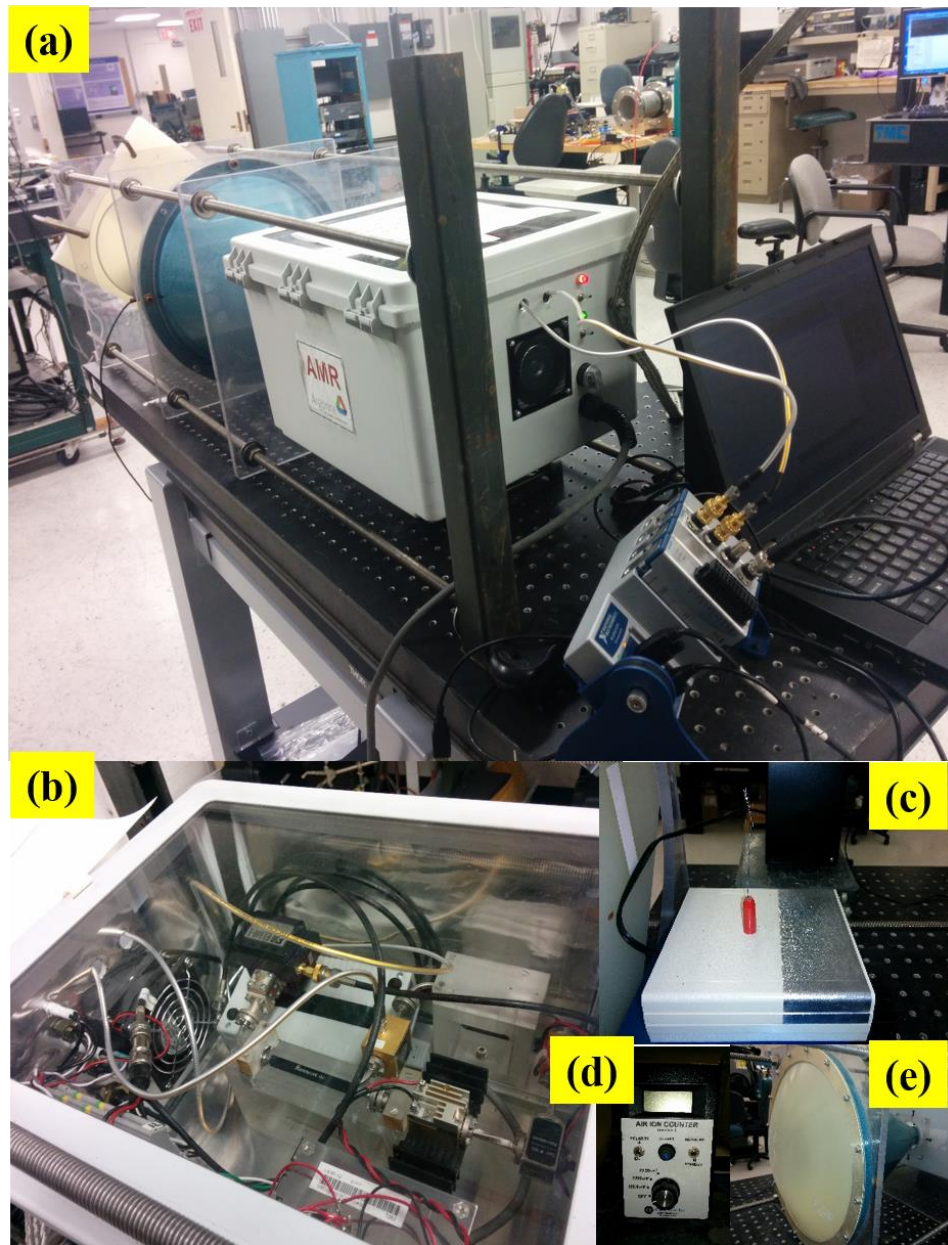


Figure 31: (a) In-house designed portable low power 94 GHz millimeter wave system for standoff detection of ionizing radiation, (b)-(e) shows different components including NIG (Comtech Research, model IG-133A), Ion counter (Alpha Lab, model AIC20M) and 12'' EM lens to focus on an area of $\sim 3 \text{ mm}^2$.

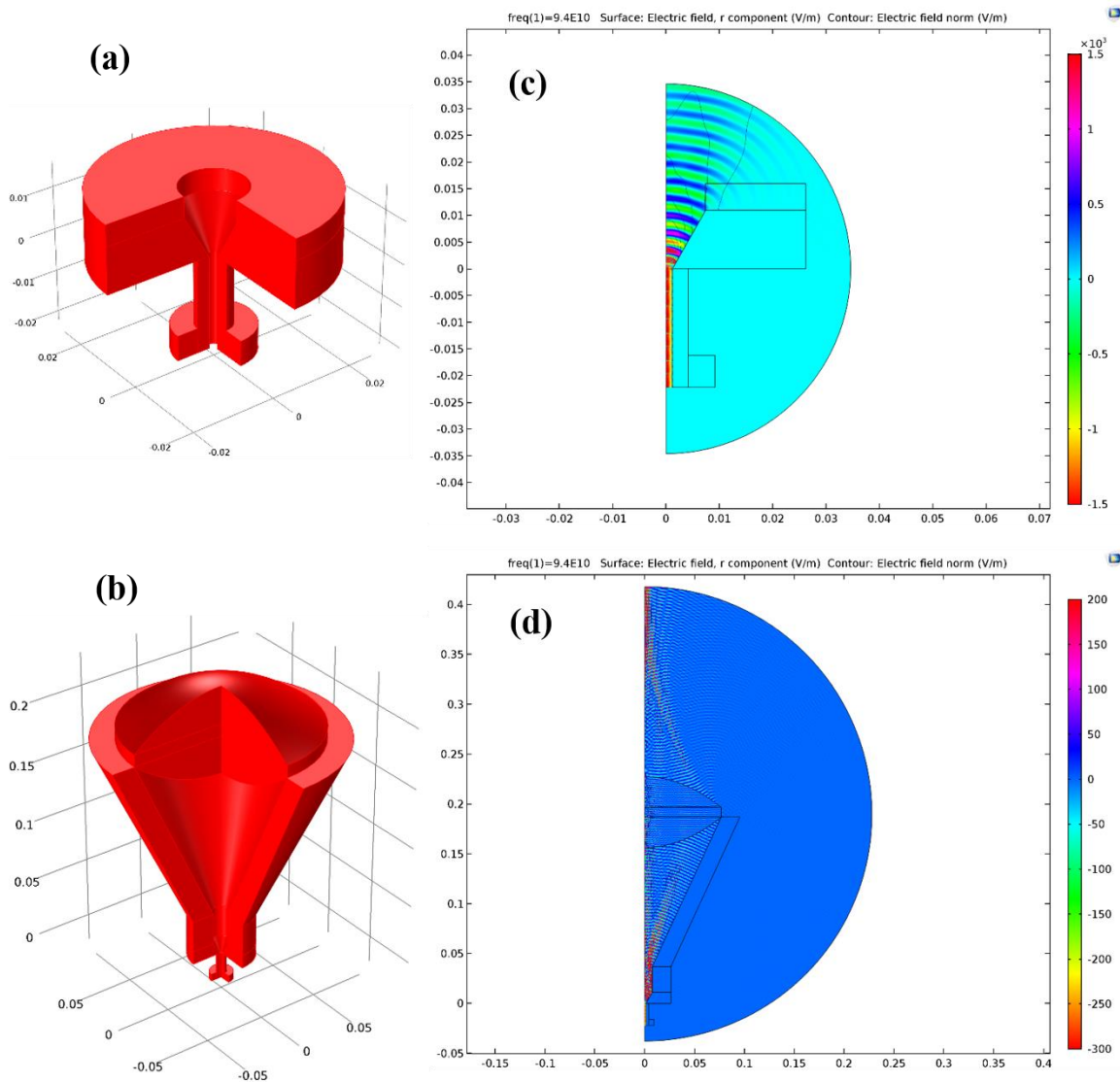


Figure 32: COMSOL modeling and simulation of 94 GHz antenna structure (a) with (b) without teflon dielectric lens for beam focusing. Corresponding electric field patterns are shown in (c) and (d) respectively.

4.2.2. COMSOL modeling of lens antenna for targeted detection

A series 857 spot-focusing horn lens antenna from Alpha Industries, Inc. was used for targeted detection. The antenna consists of a conical feed horn and two equal plano-convex dielectric lenses mounted back to back. The combination of lenses refracts the microwave signal in either direction. The dielectric constant and the loss tangent of the lens

material at millimeter wave frequencies are 2.53 and ~ 0.001 , respectively. Advantages of the spot-focus design include small size for energy concentration and near-field operation. The spot width at the 3 dB point is $\sim 1\lambda$ and the depth of focus is $\sim 10\lambda$. The spot is located in front of the lens at a distance equal to the diameter of the lens (i.e. $F/D = 1$). Figure 32 shows the real part (\vec{E}_r) and the norm contour of the electric field which shows the 94 GHz EM wave propagating towards the horn aperture and subsequently being focused by the dielectric lens. The lens antenna can be modified by removing the second refracting lens to focus the beam at infinity for long distance measurements. This type of lens antenna are suitable for measuring plasma densities, bulk dielectric materials and temperature.

4.3. Experimental observation

4.3.1. Preliminary investigation using a negative ion generator source – diffusion charging of nanowire surface

The first experiment was performed by simulating the effect of a real nuclear radiation source using a NIG. A NIG from Comtech Research (model IG-133A) which can produce 20×10^6 ions/cm³/s was used to generate negative ions in the surrounding atmosphere. A high negative voltage is applied to a bunch of very sharp needle like structures. The high electric field at the tip of the needles ionizes the surrounding air where needles collectively repels the electrons/ions into the atmosphere [21]. An ion counter was placed in tandem which measures the ion density by drawing air ions into a Faraday plate and recording the change in voltage. The NIG and the ion counter are shown in figure 31(c) and figure 31(d) respectively. The NIG was placed in the millimeter wave beam path and measurements were performed while periodically turning it 'ON' and 'OFF'. Figure 33 shows a typical measurement of millimeter wave scattering from as-synthesized In₂O₃

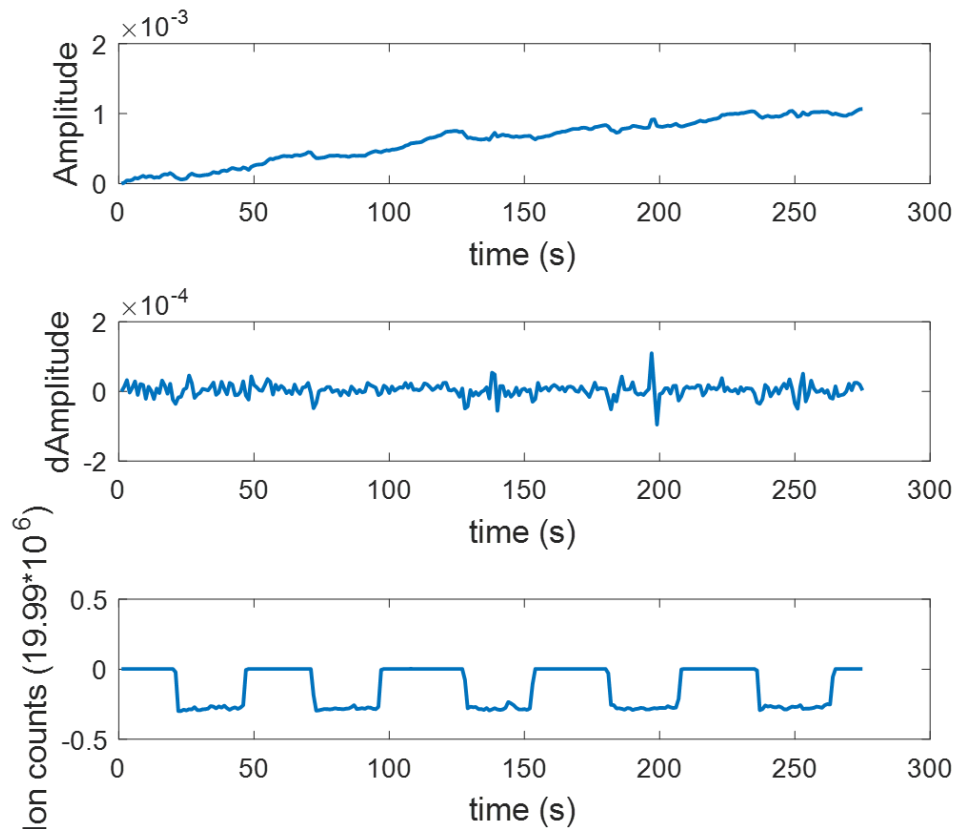


Figure 33: (Top) Scattered millimeter wave signal intensity from as-synthesized nanowires while being exposed to NIG. Measurable changes in the signal intensity could not be observed in this case. (Middle) subplot shows the corresponding differential amplitude and (Bottom) measured ion counts clearly showing the ‘ON’ and ‘OFF’ positions of the NIG. NIG was placed 2 cm away from the sample in the beam path.

nanowires where the NIG was modulated over five cycles. The data was collected in a reflection mode where the sample was mounted on a teflon block which is transparent to EM waves. The acquired data was subtracted from the first data point while the NIG was off in order to eliminate any background effects. We observed a gradual increase in the scattered signal intensity, but any measurable fast temporal changes could not be observed and could be due to enhanced low frequency EM wave absorption in the as-synthesized nanowires due to high density of intrinsic surface defects which was confirmed previously

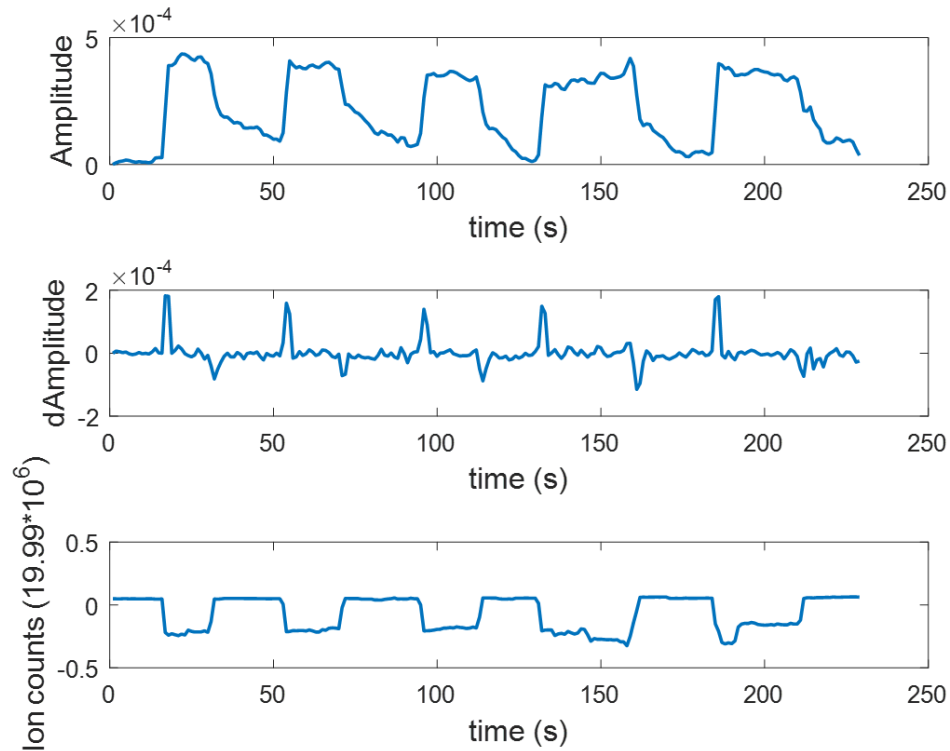


Figure 34: (Top) Scattered millimeter wave signal intensity from surface passivated nanowires while being exposed to NIG. Measurable changes in the signal intensity is observed in this case primarily due to diffusion charging of the nanowire surface. NIG was placed 2 cm away from the sample in the beam path.

using HRTEM, XPS and optical characterization [67]. Point defects in nanostructures such as vacancies or vacancy clusters are known to be present in very high densities which can be several orders of magnitude higher than those generally present in micron-sized particles, and are susceptible to polarization under the influence of an EM field [94]. As reported by Mo *et al.* [95], there are mainly three kinds of polarization that may contribute towards the dielectric properties of nanostructures. They are (a) space charge polarization which is caused by the trapping of charge carriers in point defects and generally originates from high density of surface states, (b) rotation direction polarization arising due to ion vacancies and (c) electronic relaxation polarization which mainly occurs in compact

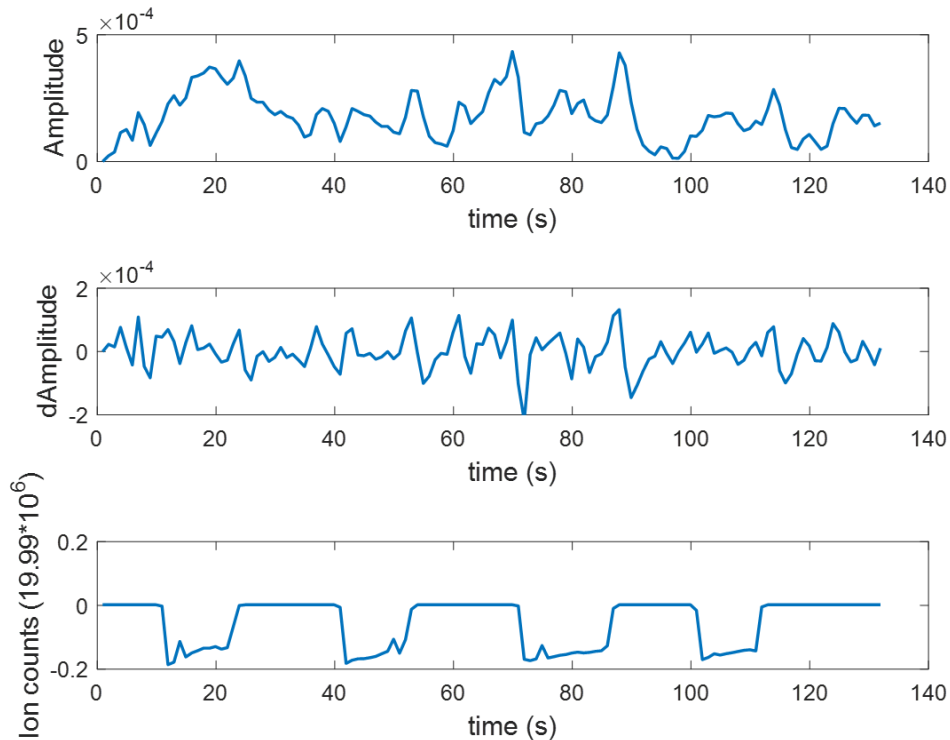


Figure 35: Control measurement without the nanowires shows no measurable changes due to scattering from ionized air under ambient conditions.

textured materials. However, due to the complex nature of various polarization mechanisms occurring in nanostructures, it is often difficult to isolate and identify contribution due to each mechanism [96] and as a result, the total contribution is generally measured. Under the influence of an alternating EM field, damped vibration of dipoles occurring due to repeated polarization of the surface states in the as-synthesized nanowires, can result in strong absorption of the EM energy.

However, while using the surface passivated nanowire samples, we observed measurable changes in the scattered signal intensity as shown in figure 34 with a fast rise time of ~ 0.5 s when the NIG is turned on and slow decay time of ~ 10 s after the NIG is turned off. We propose that there are two possible mechanism for this type of observation. Firstly, there

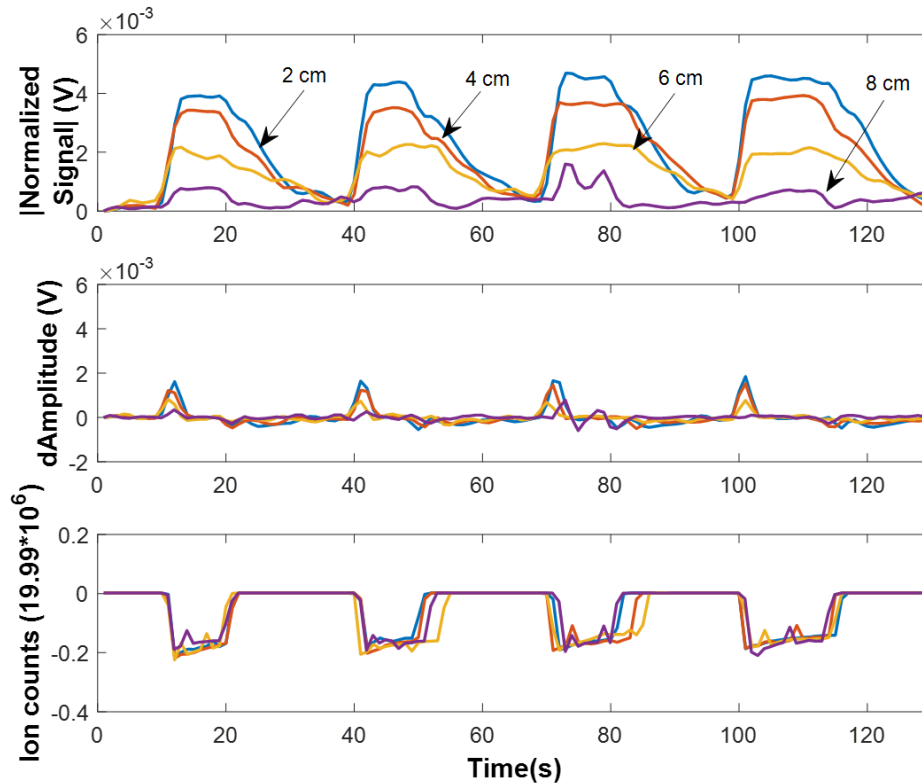


Figure 36: Scattered signal measured as a function of distance from the NIG where no surface charging effect was seen beyond 10 cm of source and sample separation due to very short lifetime of electrons in ambient atmosphere.

is significant reduction of surface defects due to high temperature annealing in an oxygen rich environment which leads to lower EM absorbing characteristics of the surface passivated nanowires. As a result, the nanowires are more transparent. Secondly, when the NIG is turned on, it leads to diffusion charging of the nanowire due to an external source of charges which deposits a layer of surface electrons [21]. This could be due to presence of a well-ordered hydroxylated surface as was confirmed by XPS measurements post thermal annealing treatment. Similar observation has previously been reported by Sami *et al.* [22] and Kar *et al.* [63]. Charging of the nanowire surface increases millimeter wave scattering and decreases absorption which could be due to the presence of extra surface

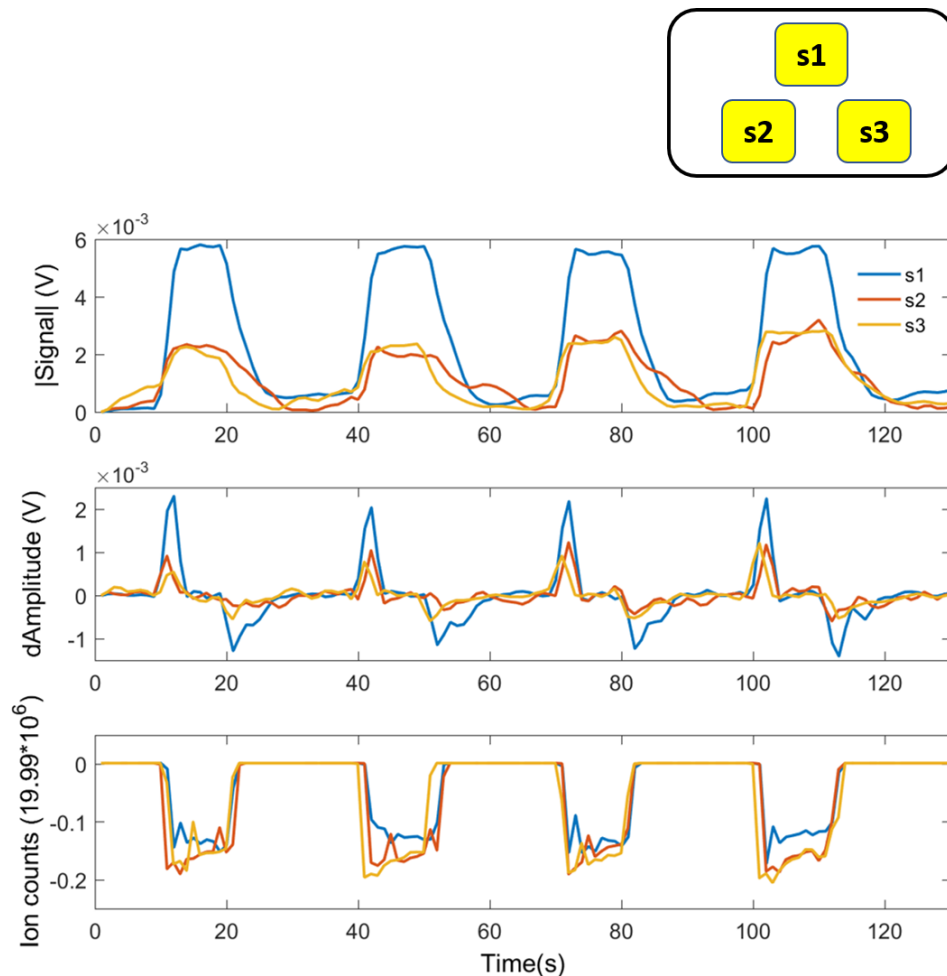


Figure 37: Scattered intensity measured from three different samples spatially separated by 0.5 cm along ‘y-axis’ and 1 cm along ‘x-axis’ as shown in the index showing the ability of the system to perform targeted measurements.

electrons [22]. Adsorption of water in dissociative form, leading to the occurrence of strong surface dipoles which vibrates in response to the applied oscillatory EM field thereby causing energy dissipation. Thus, it can be hypothesized that jamming of surface dipoles due to charging effects may be caused when

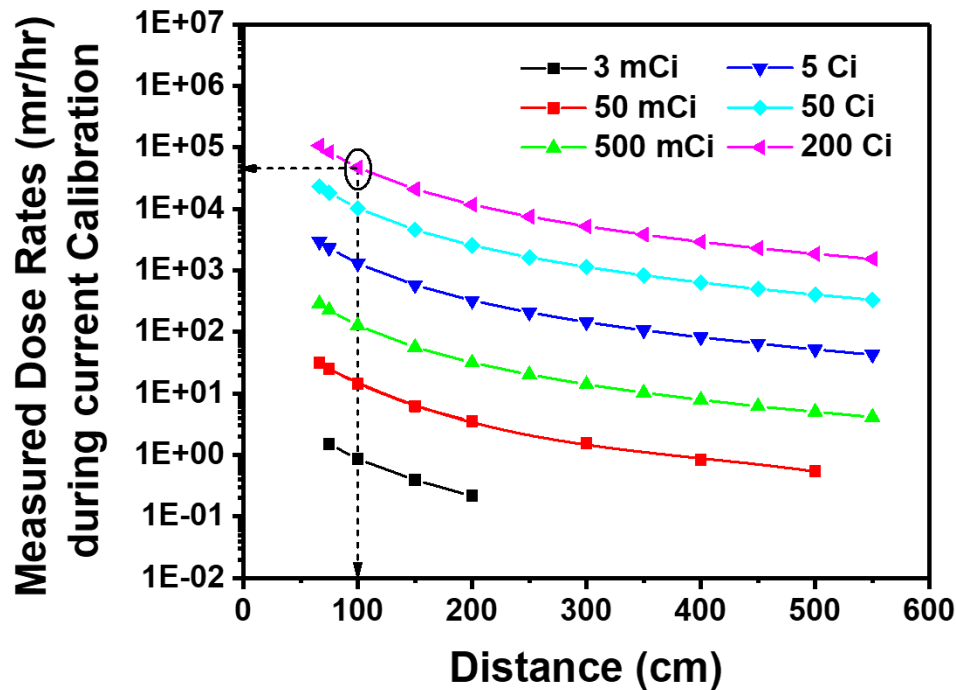


Figure 38: Calibration data showing measured dosage as a function of distance from the source (Hopewell GC-60-A). Dotted arrow line shows for a 200 Ci source, ~40,000 mr/hr dosage being used in our experiment at a distance of 100 cm from the source.

extra surface charges are present [22]. Further, previous literature reports have concluded that no change in the inherent nanowire surface properties takes place while being exposed to an NIG [63] which gives enough confidence to the proposed theory.

Control measurements without any nanowires on a bare polished Si substrate as shown in figure 35 does not show any measurable change in the scattered signal intensity. To get an idea about the sensitivity, distance between the NIG and the sample was varied, and the results are shown in figure 36. It can be observed that the scattered signal intensity falls rapidly as the source is moved away from the samples which is due to the fact that electron lifetime in the atmosphere is ~300 ns [97], before they get captured by molecules in the surrounding atmosphere [21, 22]. This significantly reduces the charging effect

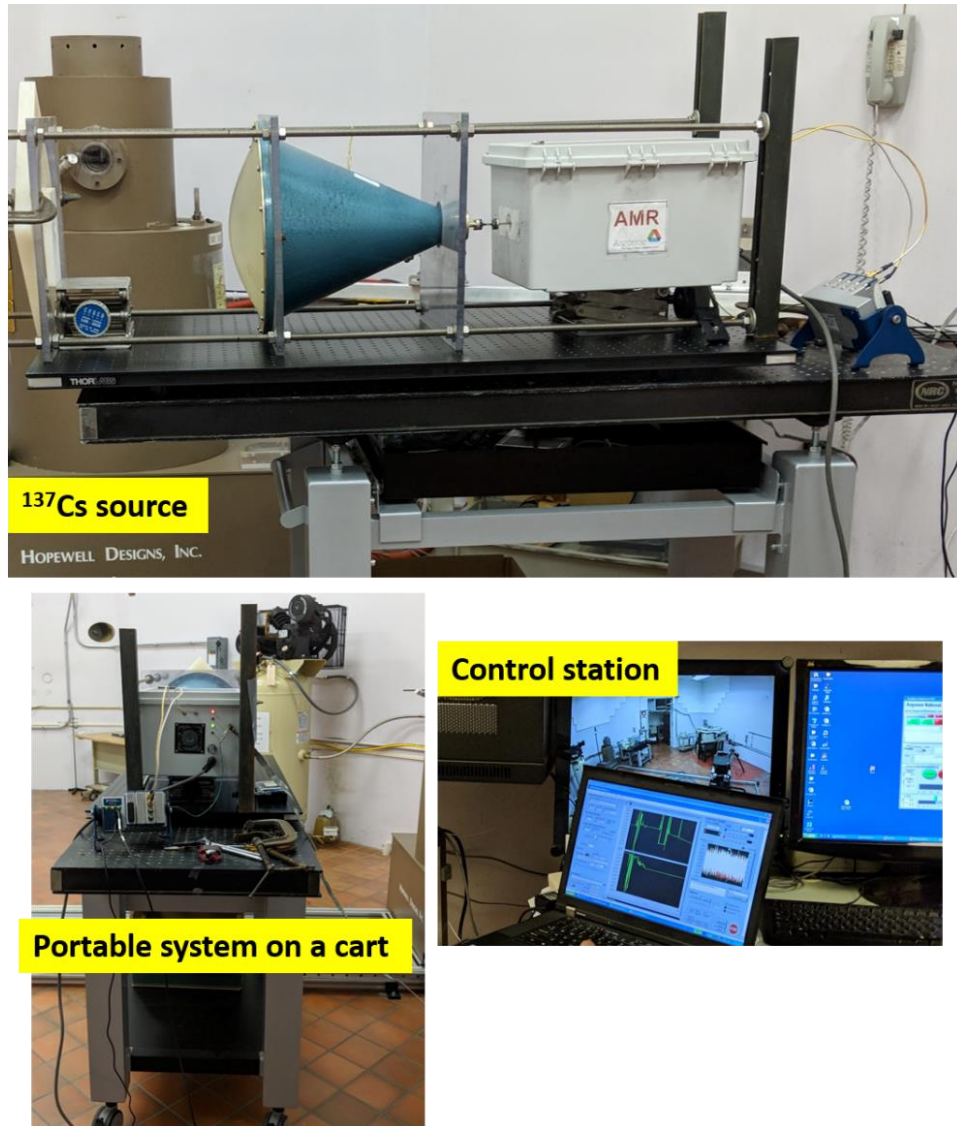


Figure 39: Actual experimental setup for the ^{137}Cs test where (top) image shows the source, (bottom left) image shows the portable 94 GHz system, (bottom right) the control station located outside the testing facility to monitor and record real-time data during irradiation.

on the nanowire surface and hence on the scattered signal intensity. We further experimented with multiple spatially distributed tags where three different nanowire samples mounted at different positions as shown in the inset of figure 37 were probed from a substantial standoff distance of ~ 30 cm. We were able to detect measurable changes in

all three samples as shown in figure 37 where the scattering intensity was found to vary from sample to sample and could be due to non-uniform thickness of the nanowire coating.

4.3.2. Application of In₂O₃ nanowires for stand-off detection of ¹³⁷Cs γ -radiation source

Based on our NIG test, one could envision the usage of the surface passivated In₂O₃ nanowires towards detection of a real nuclear radiation source. For this purpose, we performed standoff measurements while exposing the nanowires to 200 Ci of ¹³⁷Cs γ -radiation with a dosage of ~40,000 mr/hr and photon energy of 667 keV. The dosage vs distance calibration curve for various sources is shown in figure 38. It is well known that depending on the source strength, γ -radiation causes air ionization by knocking off electrons from atmospheric nitrogen and oxygen atoms. Unlike electrons from an NIG source, these electrons have enough energy to get captured by the surface chemisorbed oxygen species thereby modulating the nanowire surface properties. However, it has been recently calculated theoretically that air ionization due to the γ photons generates 10 electrons/cm³ within a few millimeters of the detector [63, 97] and this effectively reduces air ionization contribution to the changes seen here which is discussed next.

Figure 39 shows the actual experimental setup where the nanowire samples were placed at a distance of ~100 cm away from the source. Irradiation of semiconductor devices with high-dosage of γ -photons leads to production of lattice defects and surface traps at the semiconductor surface [87, 98]. The primary interaction for 662 keV γ -rays with the sample is expected to be through Compton scattering [99], in which case the high-energy photons inelastically scatter from both electrons and nuclides. In the first case, electrons are initially ionized, but as the energy is gradually reduced through interactions, electrons are excited

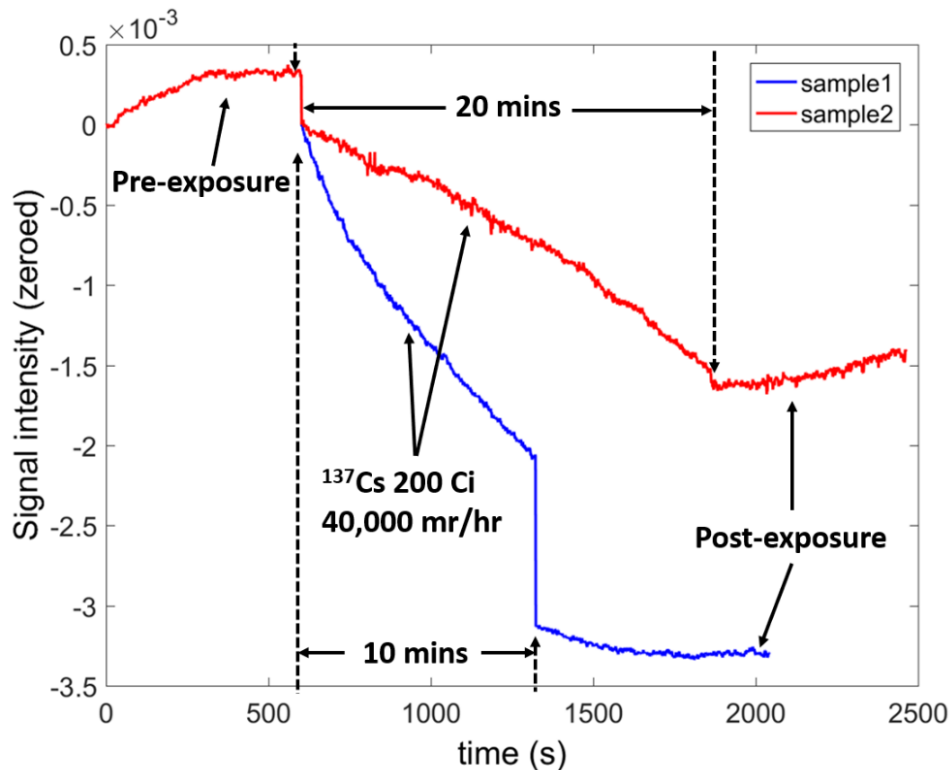


Figure 40: Shows real-time data collected on two surface passivated samples with 10 and 20 mins of ^{137}Cs irradiation. Approximately 10 mins of data was collected before irradiation which shows near constant response whereas during irradiation, scattering intensity decreases progressively with time due to formation of V_O defects in the nanowires thereby becoming more lossy. Under post-irradiation condition, again the scattering intensity does not change.

high into the conduction band. For oxide materials, the 662 keV γ -rays have enough energy to form oxygen vacancies within the lattice [99]. Most of the defects are created on the surface of the nanowires as previously reported by kar *et al.* [63] where significant increase in the defect emissions due to V_O surface states was observed post irradiation.

Figure 40 shows the experimental results where the nanowire samples were exposed to ^{137}Cs γ -radiation. Between each successive measurement, the data was subtracted from the first data point of pre-exposure test to record the relative change with respect to the initial condition. We have presented real-time data acquired for two samples which were exposed for 10 mins

and 20 mins respectively. Before exposure, for both samples background data was collected for ~10 mins which does show an initial increase in the scattered signal intensity and finally becomes constant and could be due to thermal drift of the receiver. The pre-exposure data collected at different time instances for both samples shows similar trend where the blue data points lie in the background and cannot be seen in figure 40 which further shows the overall stability of the system. Consequently, during irradiation, we observed a gradual decrease in the scattering intensity for both samples. However, an uniform trend for both samples could not be ascertained and hence calls for further investigation. Nevertheless, the preliminary results are encouraging as the gradual decrease in the scattering intensity can be directly correlated with more surface defects (V_o) being created while being irradiated. Basically, an increase in the density of point defects on the nanowire surface leads to an increase of the EM absorbing property of the nanowires [87] due to various polarization mechanisms as discussed earlier especially the space charge polarization and rotational direction polarization processes. The imaginary part, ϵ'' , of the complex permittivity, ($\epsilon_r = \epsilon' + j\epsilon''$), increases [19] and hence the nanowires become more lossy due to an increase in the loss tangents ($\frac{\epsilon''}{\epsilon'}$). Post irradiation, the changes in the nanowire properties were found to be permanent [63] and the scattering intensity could be seen to be nearly constant which does not change over a period of ~10 mins. For sample 1, it can be observed that between each successive measurement, there is a drop in the scattering intensity relative to the last data point. This can be attributed to the ground vibration from a nearby operating vacuum pump in the building which might have slightly displaced the sample from its initial position due to the presence of a weak coupling between the sample and the mount. For sample 2, we do not observe such change once we made sure that the sample has been properly mounted.

4.4. Conclusion

To summarize, here we have presented an alternate approach to perform stand-off measurements of ionizing radiation by probing its effect on nearby structures covertly or overtly tagged with a sensor material. One of the advantage of this alternate detection methodology is that it is not dependent on atmospheric turbulence which can significantly reduce the detection range. To perform stand-off measurements, a low power 94 GHz portable transceiver has been designed which coupled to a lens antenna was able to successfully detect changes in the scattered signal intensity from spatially distributed tags upon exposure to a NIG source. No changes in the scattering intensity could be observed while using as-synthesized nanowires which could be due to strong absorption of EM waves in these samples due to high density of surface V_O defects. The surface-passivated samples however showed measurable changes as long as the NIG was within 10 cm from the sample. This behavior was attributed due to a decrease in density of surface states thereby making the nanowires more transparent to EM waves and due to diffusion charging of the nanowire surface while the NIG was turned on due to the presence of an uniform hydroxylated surface. Presence of extra surface charges during charging of the nanowires causes jamming of the surface dipoles which results in increased overall transmission through the sample. The surface passivated nanowires were further tested by exposing to a ^{137}Cs γ -radiation source which emits photons of energy 667 keV resulting in the formation of high density of V_O defects on the surface of the nanowires. This change in the density of the surface states directly correlates with the EM absorbing properties of the nanowires mainly due to space charge polarization and rotational direction polarization process. Overall the change in the EM absorbing property of the nanowires were detected by

probing the samples at 94 GHz millimeter wave frequency. We observed a gradual decrease in the scattering intensity due to increased absorption while the nanowire was being irradiated. Under pre- and post-exposure conditions, the scattering intensity does not change. This results from this preliminary investigation is encouraging to pursue advanced research in this direction. The same nanostructured dielectric material could also be used in a resonator cavity to enhance the sensitivity. One could argue that a plausible drawback of this technique is the deployment of the sensor tags for covert operations. Given that the material is in dispersed form (which can possibly be applied as sensor paints on target surfaces) as well as can be synthesized to be transparent by doping with Sn, which would provide tremendous advantages in terms of the size and applicability for such scenarios. Another major drawback of this system is its inability to classify the nature of the radiation source i.e. the system lacks specificity. Nonetheless, while this area of research is still naive after decades of research, we believe that this alternate approach adds some merit in solving the existing problem of performing true long-range ionizing radiation detection and monitoring in real-time.

5. DEVELOPMENT OF FAST SWEEP CHIRPED-PULSE FOURIER TRANSFORM MILLIMETER WAVE SPECTROMETER FOR BROADBAND CHEMICAL SENSING IN REAL-TIME

(Portion of this chapter is copied from my unpublished manuscript
Mukherjee S, Elmer TW, Bakhtiari S, Gopalsami N, Koehl ER, Strosio MA, Dutta M. Design and
operation of an ultrafast and compact chirped-pulse Fourier transform millimeter wave spectrometer
operating in the 110-140 GHz range for real-time chemical analysis, *under preparation*.)

A small change in molecular mass distribution can significantly affect its rotational inertia, thereby opening the possibility to easily distinguish between its isotopologues, isomers and conformers by resolving corresponding rotational spectra. In this regard, EM waves at microwave and millimeter wave frequencies have evolved to be standard powerful tools for high resolution rotational spectroscopy [32-34, 100]. Of particular interest is the millimeter wave region of the EM spectrum which has found significant applications to study Rydberg-Rydberg transitions at medium-to-high values of the effective principle quantum number (n^*) [101, 102], detection of astronomical molecules [103] and for room temperature detection of molecules with high sensitivity and resolution [104-106]. However, a particular area that has been relatively unexplored is the use of such spectroscopic technique for in-field real-time trace gas analysis for environmental monitoring purposes. Application for in-field real-time measurements would require scaling down of system dimensions and the ability to perform fast broadband sweeps for multi-point identification as well as quantification through library matching due to unknown composition of the sample.

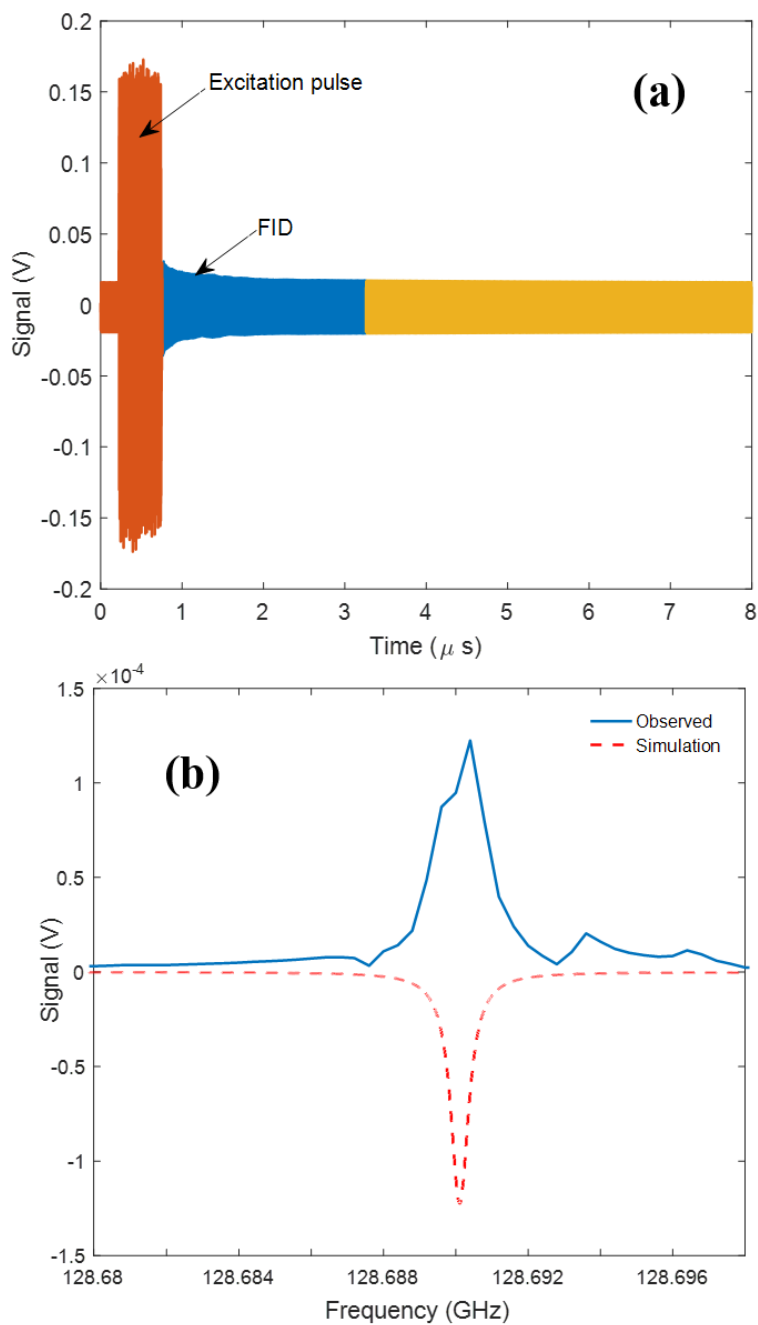


Figure 41: Shows (a) time domain signal averaged 100,000 times and (b) corresponding frequency spectrum.

5.1. Background on the chirped-pulse Fourier transform technique

In recent times, there has been significant development in microwave and millimeter wave gas phase spectroscopy particularly to reduce long acquisition time using fast sweeps in frequency domain [107, 108] and to automate precise tuning of cavity resonance frequency in Fabry–Pérot FTMW [109-113] and FTMMW [105, 113-117] spectroscopy. These efforts have been successful to some extent, however the major breakthrough came with the invention of the CP-FTMW spectroscopy technique [32-34] that provides true broadband capability with relatively shorter acquisition times. The chirp pulse spectrometer takes advantage of the recent advancement in arbitrary waveform generators (AWG) and broadband detectors to perform time domain rotational spectroscopy. In this technique, a short chirp pulse is generated typically of duration $<1 \mu\text{s}$ and produces a broadband linear frequency sweep to polarize all the transitions of the sample that lies within the chirp BW. Following the chirp excitation, the molecules in their excited states, quickly decays to their ground state thereby emitting a broadband free induction decay (FID) signal which is then detected and averaged in time domain by a fast digitizer. Figure 41 shows a typical time domain and frequency domain signal in CP-FTMMW spectroscopy.

One of the key advantages of CPFT technique for high resolution spectroscopy is that each individual spectral line width is determined by the relaxation rate of the corresponding coherent molecular FID which is significantly longer than the inverse of the spectrum BW being measured [118]. The chirp pulse signal scales favorably as BW is increased in contrast to Fourier-transform limited pulse [119] where the duration of the pulse is determined by the full measurement BW for optimal excitation. Recent advancement in the

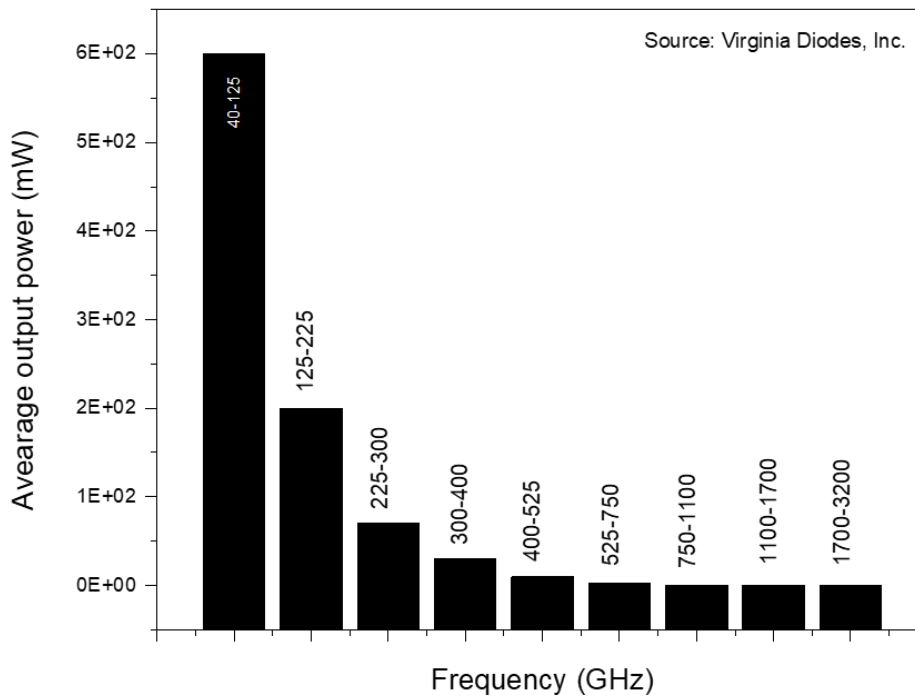


Figure 42: Currently available source power from solid-state components in the millimeter wave and terahertz frequency bands.

area of high-speed digital electronics has made possible to achieve fast sweep rates in AWGs where pulses of 0.01–1 μ s duration with 10–100 GHz of BWs can be produced, which is required for CPFT spectroscopy [118]. Conventional microwave sources are unable to achieve such fast sweep rates, however they have sufficient phase stability and spectral purity for application in targeted millimeter-wave spectroscopy [120] where single frequency excitation is needed. If the target sample is well known, the associated frequencies can be obtained from a standard molecular spectroscopy database. An important aspect of CPFT technique is to perform time domain averaging on the coherent FID signal to increase the sensitivity and the dynamic range. To achieve this, phase reproducible chirp pulses are needed which can be provided by the AWG. Further due to significant advancement in the IC manufacturing, currently very fast digitizers with wide

analog BW and faster sampling rate are available which can perform high-speed waveform digitization and processing [121]. These recent advances in digital electronics has significantly contributed towards the realization of fast sweep CPFT spectrometers for near real-time chemical analysis.

CPFT technique relies on proper synchronization of the AWG and the digitizer which is achieved by using highly stable frequency standard typically a 10 MHz rubidium crystal oscillator. Another important aspect in CPFT millimeter wave spectroscopy is the availability of source power. Currently available solid-state millimeter wave sources can generate output powers up to 200 mW over entire W-band millimeter wave frequencies which is well above the threshold that is required for saturation [122]. Further state-of-the-art AMCs can be used to increase the spectral coverage by efficiently upconverting the AWG chirp BW to millimeter wave frequencies without changing the pulse duration. Figure 42 shows a representative plot of currently available source power over full-band from solid-state sources within the millimeter-sub terahertz (THz) region [123]. Compared to traditional frequency-tuned absorption spectroscopy, where optimization of source power is needed to avoid power saturation for each individual molecule, CPFT technique operates in the weak pulse limit thereby bypassing this need.

Within the last few years there has been successful implementation of high sensitivity and high resolution CP-FTMMW spectrometer in the 70 – 102 GHz [119], 260 – 295 GHz [118] and 530 – 620 GHz range [124]. Here we demonstrate the design and operation of a CP-FTMMW spectrometer which can operate in the WR-08 band having a 30 GHz BW from 110 – 140 GHz and capable of acquiring 13 GHz in a single shot. The spectrometer uses AMCs and medium PAs to produce an average output power of 32 mW. The

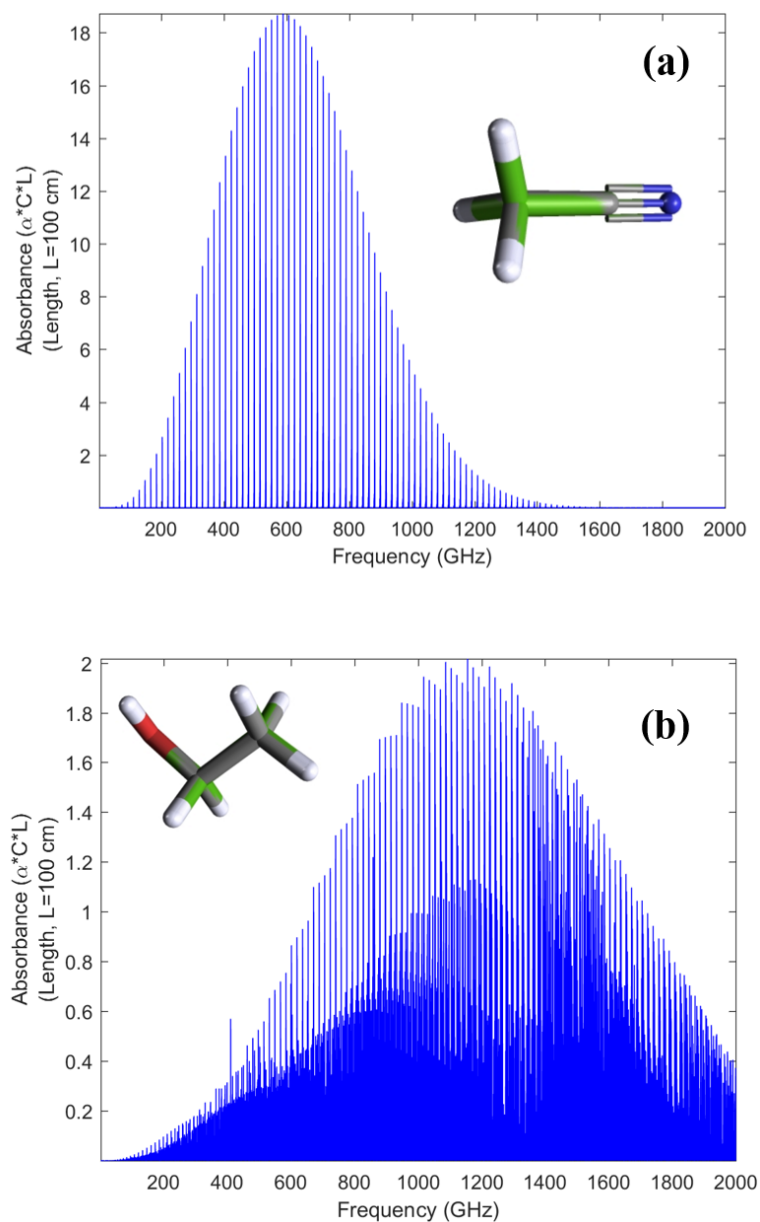


Figure 43: Absorption spectra of 100% (a) acetonitrile and (b) ethanol at 20 mTorr.

spectrometer has been tested with marker chemicals for accuracy and preliminary observation on room temperature detection of various isotopologues of acetonitrile (CH_3CN) is reported.

5.2. Design and operation of a prototype 110-140 GHz broadband spectrometer

It can be observed from figure 42 that there is almost a 60% decrease in the available source power from solid-state sources at higher frequencies above the 125 – 225 GHz range. Further, most of the high frequency sources are not able to provide uniform power over the entire BW. This would require the chirp intensity to be compensated for wideband measurements for accurate quantification during chemical analysis as the relative intensities of the peaks will vary based on the excitation power at each individual frequency point within the chirp. The power of the chirp signal might saturate the detector and as a result, scaling the FID data based on the chirp intensity itself might result in incorrect estimation of relative peak intensities of different transitions. Further, a high-power chirp pulse especially in the WR-10 and lower frequency bands where GaN based PAs and AMCs are available, can burnout the receiver if proper protection is not implemented. To protect the receiver, high-speed PIN diode switches with sub-nanosecond switching speed are used. Sub-nanosecond switching speed is critical to block the tail end of the chirp signal which otherwise would overwhelm the FID signal. The effect of chirp-tailing on the overall signal characteristics will be discussed later under subsection 5.3. The application of high-speed switches at millimeter wave frequencies is limited by their operating BW where a maximum of ~5 GHz around a center frequency can be obtained at present. However, this can be useful for targeted spectroscopy where a narrow BW is required for operation.

One important aspect of detection at higher frequencies is due to increased absorption strength of most molecules of interest as can be observed from the simulated absorption spectra of ethanol (C_2H_5OH) and CH_3CN as shown in figure 43. The intensity of the rotational lines is mainly determined by their corresponding probability of transitions

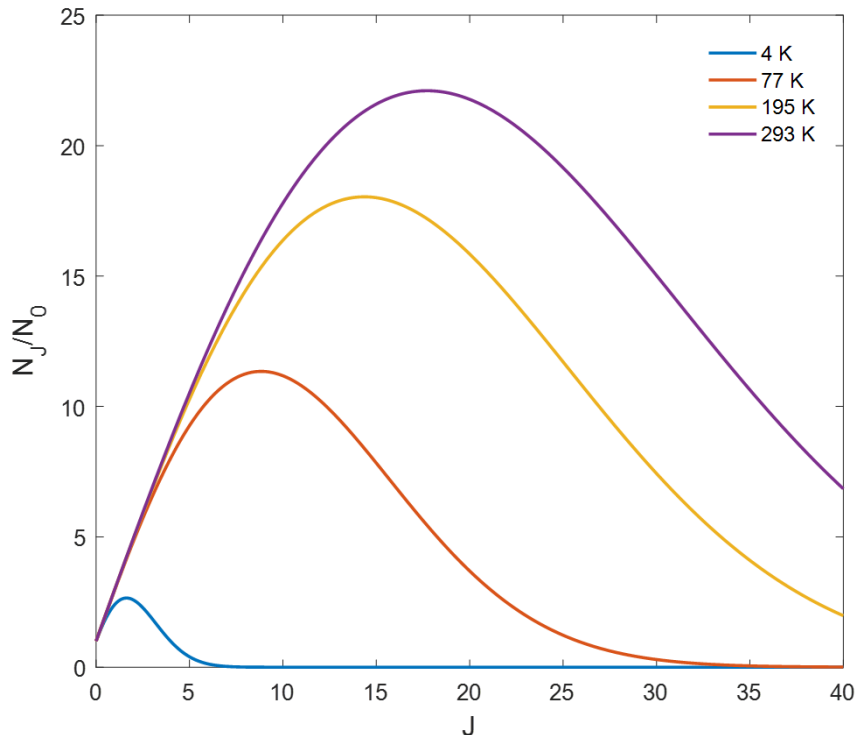


Figure 44: Boltzmann distribution of CH_3CN (room temperature 293K, dry ice 195K, liquid nitrogen 77K and liquid helium 4K).

which in turn is proportional to the population of the initial states involved which is given by the Boltzmann distribution and associated degeneracy as:

$$\frac{N_J}{N_0} = (2J + 1) \exp\left(-\frac{BhcJ(J+1)}{K_B T}\right) \quad (5.1)$$

where N_J is the number of molecules in an excited state with quantum number (J) and N_0 represents the number of molecules in the ground state. Simulating for CH_3CN , with $B = 9.19889816(54)$ GHz [125] being the rotational constant, it can be observed from figure 44 that the maximum line intensity shifts towards lower frequency with decreasing temperature. However, for in-field applications, going down to sub-millitorr pressure or lower temperature is often a challenge due to limitations of the vacuum pump power and availability of cooling components and reagents. As a result, measurements are often

needed to be performed at higher millitorr pressures and room temperature which can result in significant line broadening at higher frequencies particularly for symmetric top molecules with closely packed k-stacks thereby decreasing the spatial resolution of the spectrometer. Based on all these factors, WR-08 band was identified to be an optimal range for room temperature in-field rotational spectroscopy. The schematic of the designed system and description of the spectrometer components has been presented and discussed below.

5.2.1. Chirped pulse excitation source

The chirp is generated by a high-speed (12 GS/s) AWG (Keysight, M8190A) on channel '1' which is then mixed with local oscillator (LO) fixed frequency and upconverted by an active multiplier chain (AMC) to produce the required signal. The 12 GHz fixed LO frequency is generated by mixing a 15 GHz signal from a phase locked synthesizer (PLS) with a 3 GHz continuous wave signal generated on the channel 2 of the AWG. The 12 GHz LO is used to drive a high performance low frequency mixer operating in the 2–18 GHz range which produces the required low frequency chirp (11.25–17.5 GHz). A combination of custom designed band pass and band stop filters are used to block the LO leakage from transmitting as well as to get rid of any spurious signals lying outside the desired band. A (x8) AMC is used to produce the required signal at 90–140 GHz which is then amplified using a medium PA thereby producing an average output power of ~15 dBm (32 mW). A conical horn antenna is used to transmit the millimeter wave which is collimated into the gas cell by using a 3'' diameter teflon plano-convex lens (Thor Labs) having a focal length of 10 cm. The PLS and the AWG derives their clock frequency from a highly stable 10 MHz rubidium crystal oscillator (FS725, Stanford Research Systems).

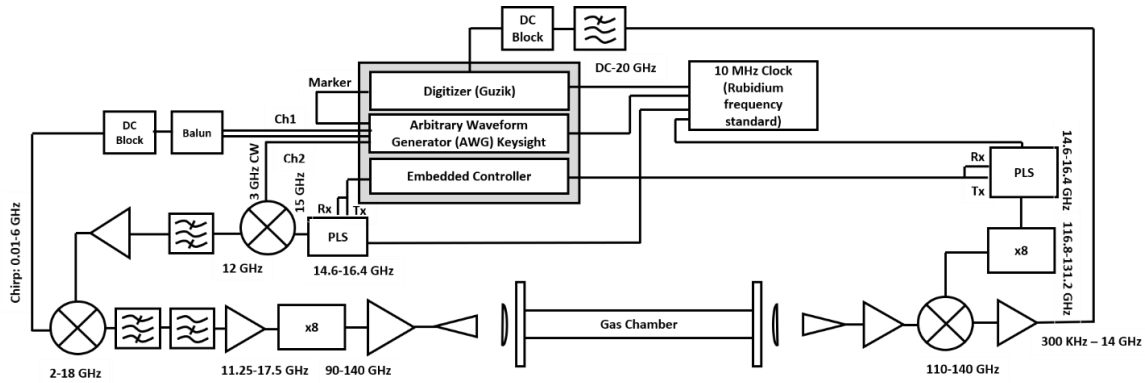


Figure 45: Schematic of a fast-sweep dual channel 110–140 GHz CP-FTMMW spectrometer for broadband trace gas sensing.

5.2.2. Receiver

The transmitted signal is focused by a different set of 3'' diameter Teflon lens on to the receiving antenna. Another set of PLS capable of generating frequencies within 14.6–16.4 GHz is upconverted by a x8 AMC and is used as the LO for down conversion. The LO frequency can be adjusted to down convert the RF within 13 GHz operating BW of the digitizer. The intermediate frequency (IF) signal was amplified and filtered before being fed into a high-speed digitizer (40 GS/s, ADC6131, Guzik Technical Enterprises). The digitizer and the receiver PLS are also locked onto the same 10 MHz reference signal. A marker signal triggered from the AWG is used to initiate the digitization. The overall system BW is limited by the operating range of the high frequency mixer (110–140 GHz) on the receiver. The AWG, digitizer and the embedded controller are integrated together in a single M9505A PXIe Chassis.

5.2.3. Gas Cell

The single pass gas cell is made up of stainless steel with a cylindrical geometry (length ~1 m) having a total volume of 2 L. There is a single inlet port which can be

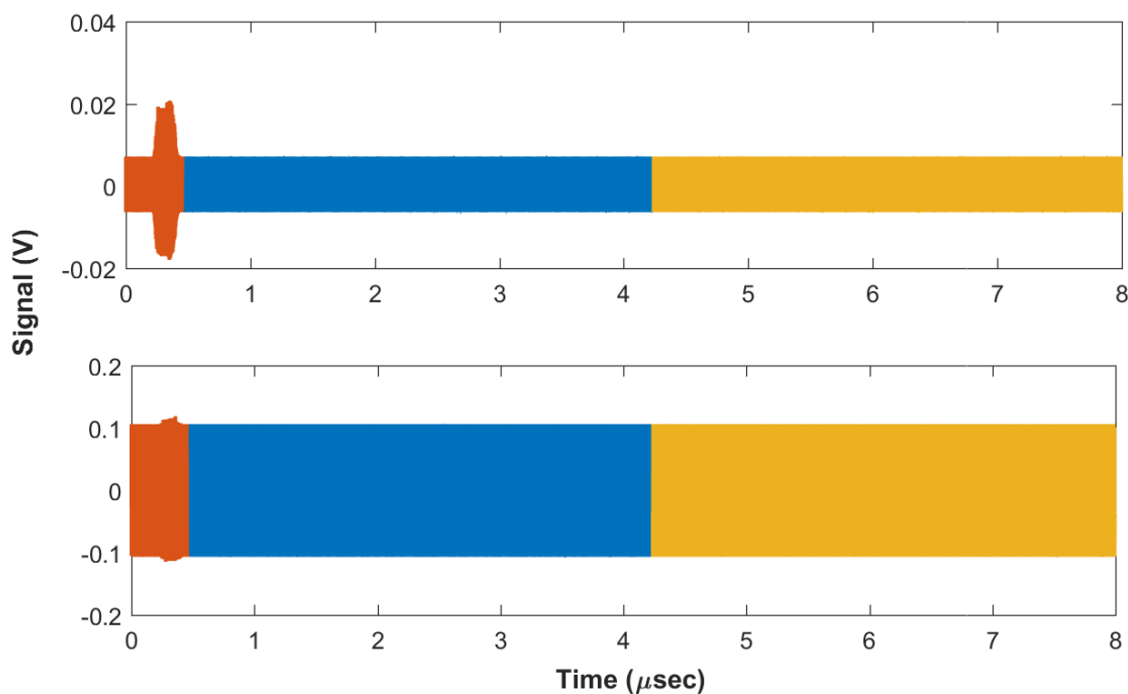


Figure 46: Time domain signal (top) without and (bottom) with LO leakage being transmitted.

configured for both liquid and gaseous sample injection while utilizing a rubber septum for the former. The liquid samples were injected using a microneedle having a total volume of 1 μL . The pressure in the gas cell was monitored using a MKS 900 series digital vacuum transducer and controller unit. Another outlet port on the gas cell is connected to a vacuum pump capable of reaching down to 0.01 mTorr. Both sides of the gas cell were fitted with 0.25'' thick teflon blocks. The cell pressure was found to rise 0.5 mTorr/hr which shows that good sealing was obtained. A representative schematic of the spectrometer is shown in figure 45.

5.3. Preliminary experimental observations

A single shot acquisition is limited by the digitizer range (13 GHz). Since the system has a total BW of ~ 30 GHz, it is necessary to be able to separately control the LO

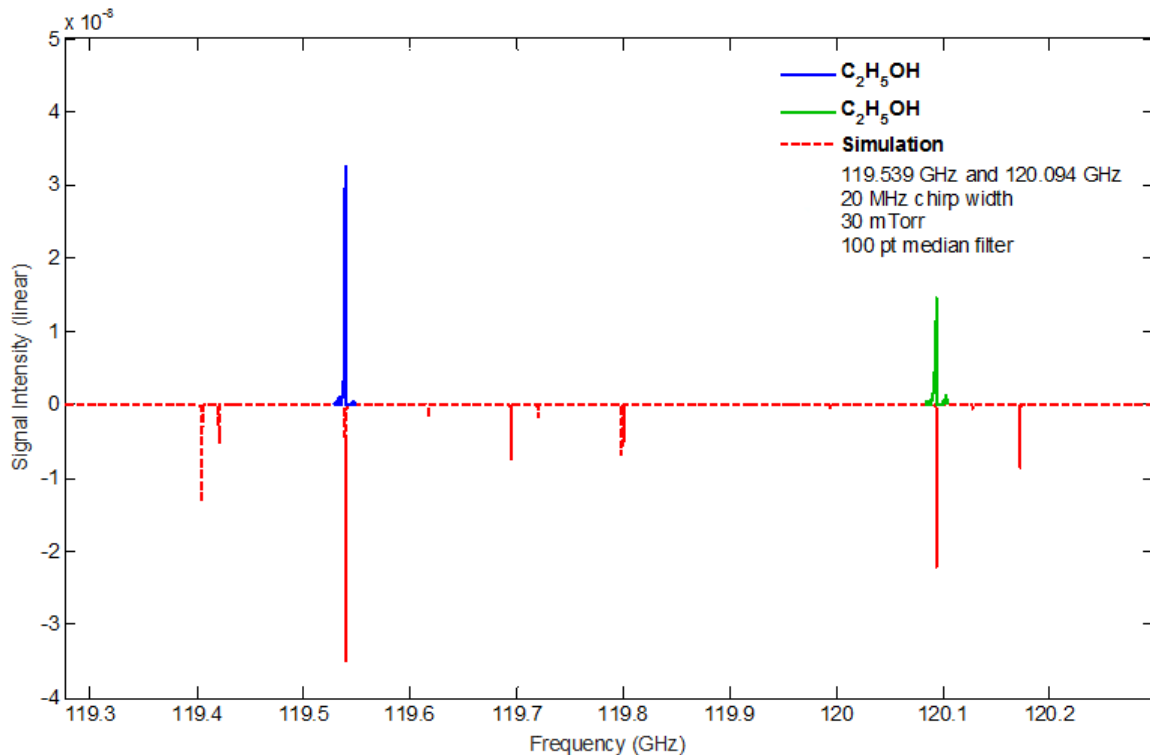


Figure 47: Segmented measurements using a narrow 20 MHz chirp of C_2H_5OH peaks centered at 119.539 GHz and 120.094 GHz.

frequencies on the transmitter and receiver arm. In our initial design as shown in figure 45, we were using two separate PLS on the transmitter and receiver arm to achieve this. However, to reduce the number of components for a compact design, we used a power divider after the transmitter PLS to utilize one of the outputs as a receiver LO. The other output was modulated by the CW frequency on channel ‘2’ of the AWG to produce a fixed 12 GHz LO before being mixed with the chirp on channel ‘1’ to generate the required RF. A fixed LO lying outside the system BW is used for the purpose of efficiently blocking any leakage post mixing from transmitting. This was achieved by using a custom designed 12 GHz notch filter with > 60 dBc stopband rejection. LO leakage can have a significant impact on the system performance as shown in figure 46. This kind of leakage can

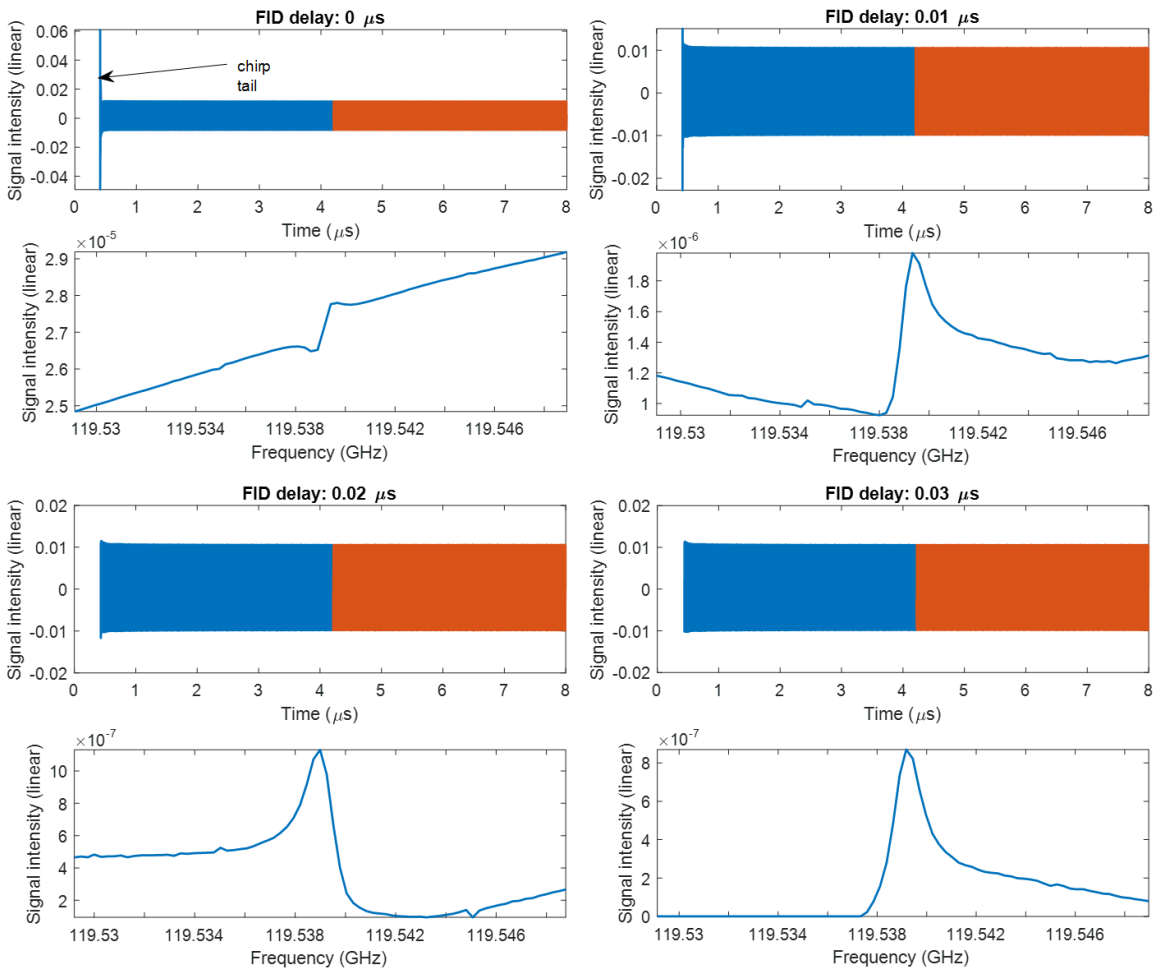


Figure 48: Signal intensity plot at varied FID delay shows the chimp-tailing effect which overwhelms the FID signal.

overwhelm the relatively weak FID signal resulting in poor sensitivity. We also observed that the LO leakage caused the system response to become unstable which resulted in the baseline to drift overtime. As a result, post processing subtraction of baseline from sample data often resulted in removal of weak intensity peaks.

5.3.1. Demonstration of spectrometer accuracy using marker chemical

The spectrometer characteristics is benchmarked using C_2H_5OH . We performed segmented chirp-based measurement for multipoint identification as shown in figure 47. A

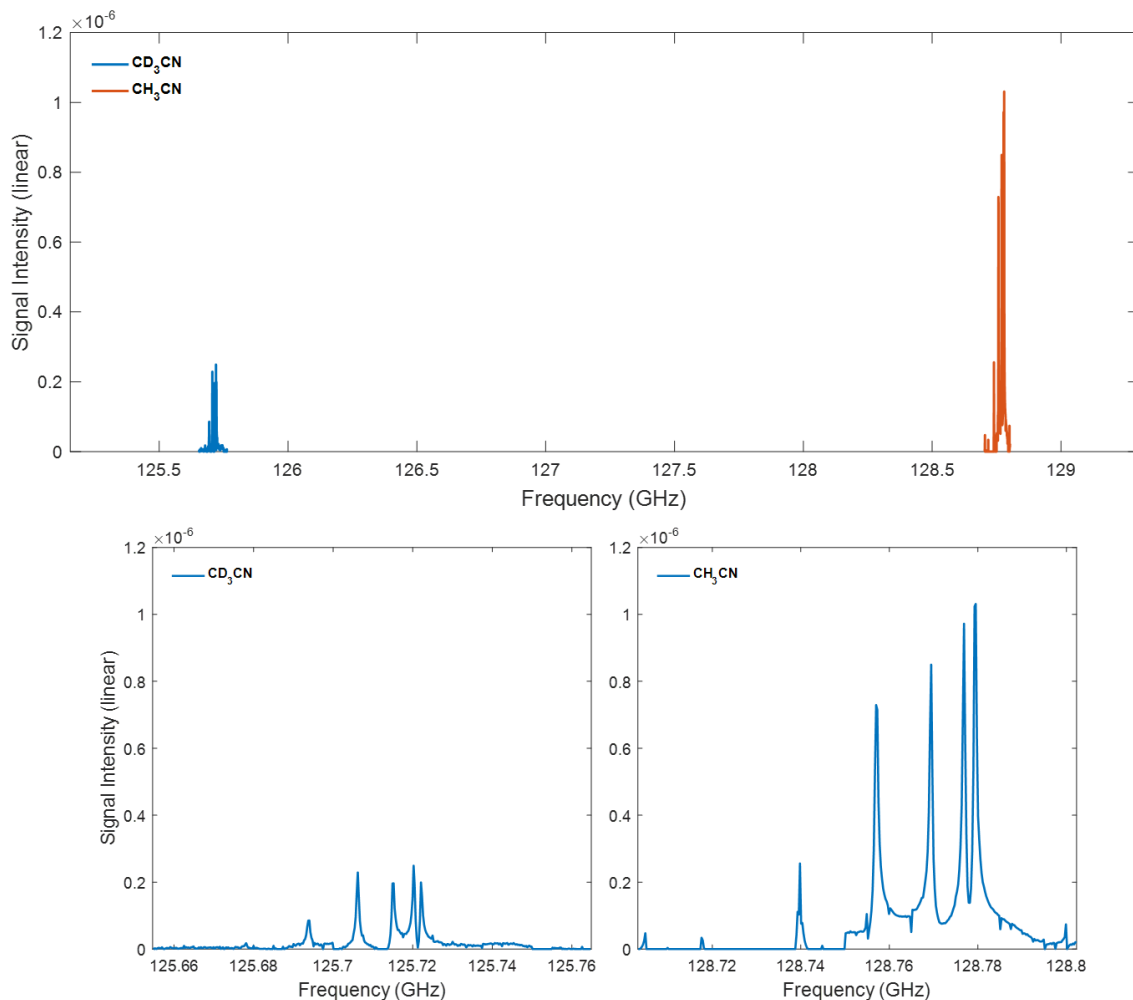


Figure 49: Detection of CD_3CN ($J = 8 \leftarrow 7, k = (7 \leftarrow 0)$) and CH_3CN ($J = 7 \leftarrow 6, k = (6 \leftarrow 0)$) simultaneously present in a mixture ratio 1:1 at 20 mTorr pressure with a 200 MHz chirp excitation.

narrow 20 MHz chirp around the center frequencies of corresponding transitions has been used as the excitation. The spectrum is an average of 100,000 FIDs and was taken at 30 mTorr cell pressure. The NASA Jet Propulsion Laboratory (JPL) simulation [126] has been plotted in red. The targeted peaks clearly match and lies within 100 kHz of the corresponding simulated spectra. Also, we observed a chirp tail that persisted for ~ 30 ns after the pulse. Due to chirp-tailing effect, processing needs to be done on a subset of the

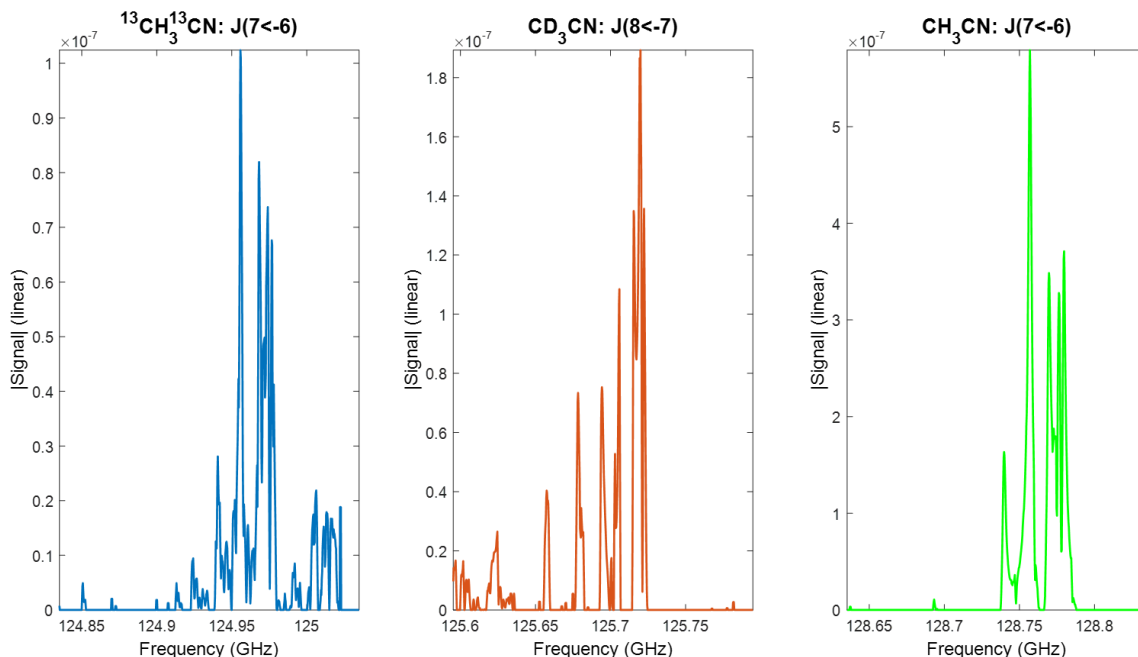


Figure 50: Detection of isotopologues of CH_3CN at 20 mTorr present in a gas mixture with varied concentration where the ratio of the mixture components ($^{13}CH_3^{13}CN/CD_3CN/CH_3CN$) is 1:4:5.

FID data ignoring the initial few points within the 30 ns time window. As it can be observed from figure 48, when the FID delay is reduced below 30 ns, the overall signal strength increases, however the FID peak is not clearly detectable. A 100-point median filter was applied during post processing to filter out any residual baseline components from chirp-tailing.

5.3.2. Analysis of a gaseous mixture – detection of various isotopologues of acetonitrile

CH_3CN and its isotopologues (a) Trideuteroacetonitrile (CD_3CN) and (b) $^{13}CH_3^{13}CN$ belongs to the C_{3v} point group and can be classified as symmetric top molecules. To the best of our knowledge, there are no known reported transition features of CD_3CN in the 110–140 GHz range. Hence, we analytically estimate the transition

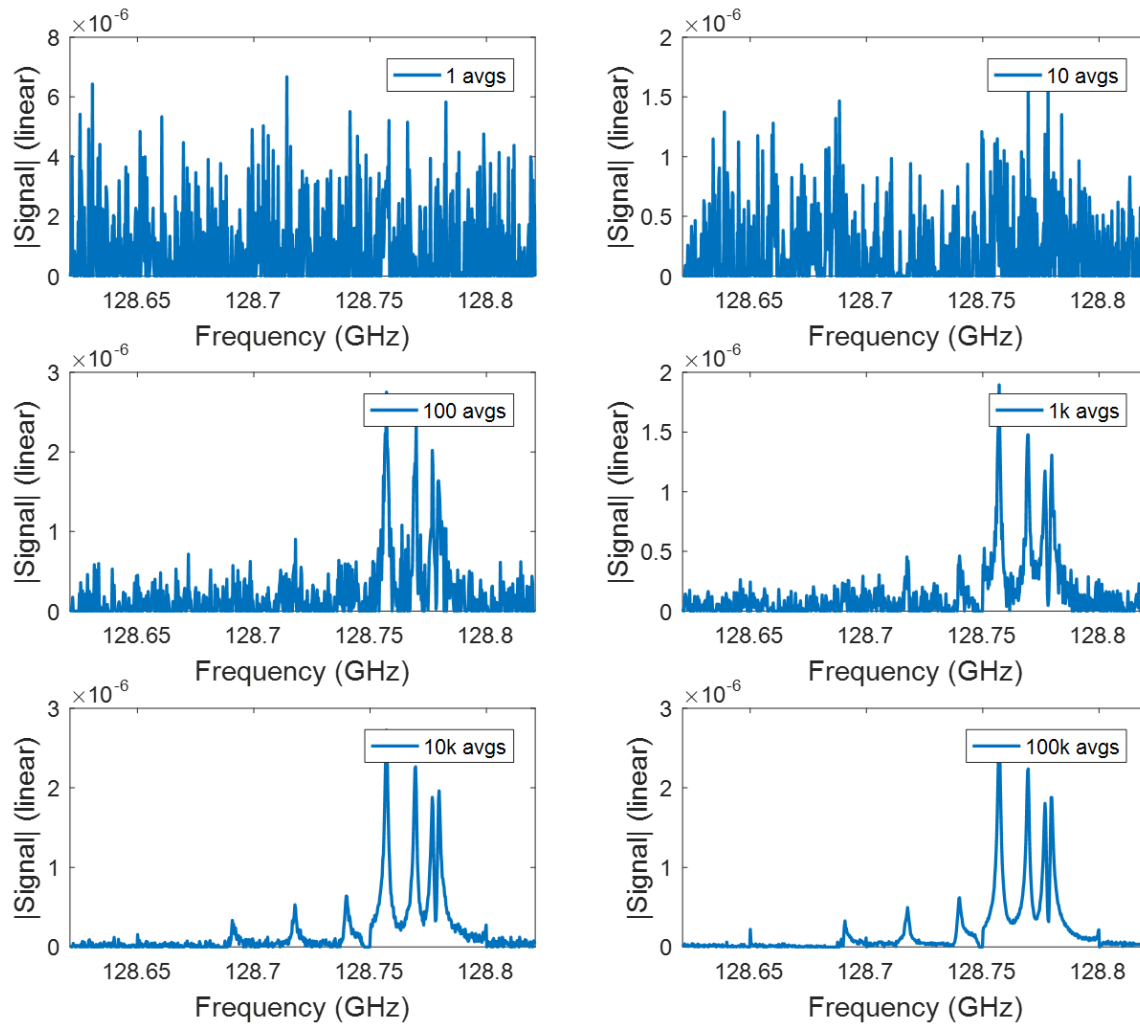


Figure 51: Shows real-time averaging capability of the digitizer to reduce the noise in the signal and increase the dynamic limit.

frequencies. The rotational Hamiltonian for ground state prolate C_{3v} molecule can be written as [125, 127]

$$E(J, k) = BJ(J + 1) + (A - B)k^2 - D_J J^2(J + 1)^2 - D_{JK} J(J + 1)k^2 - D_k k^4 + H_J J^3(J + 1)^3 + H_{JK} J^2(J + 1)^2 k^2 + H_{kJ} J(J + 1)k^4 + H_k k^6 \quad (5. 2)$$

The specific selection rule of symmetric top molecules states that during a transition, the allowed energy changes in the J, k quantum numbers are $\Delta J = \pm 1$ and $\Delta k = 0$. Hence the corresponding transition frequencies are given by

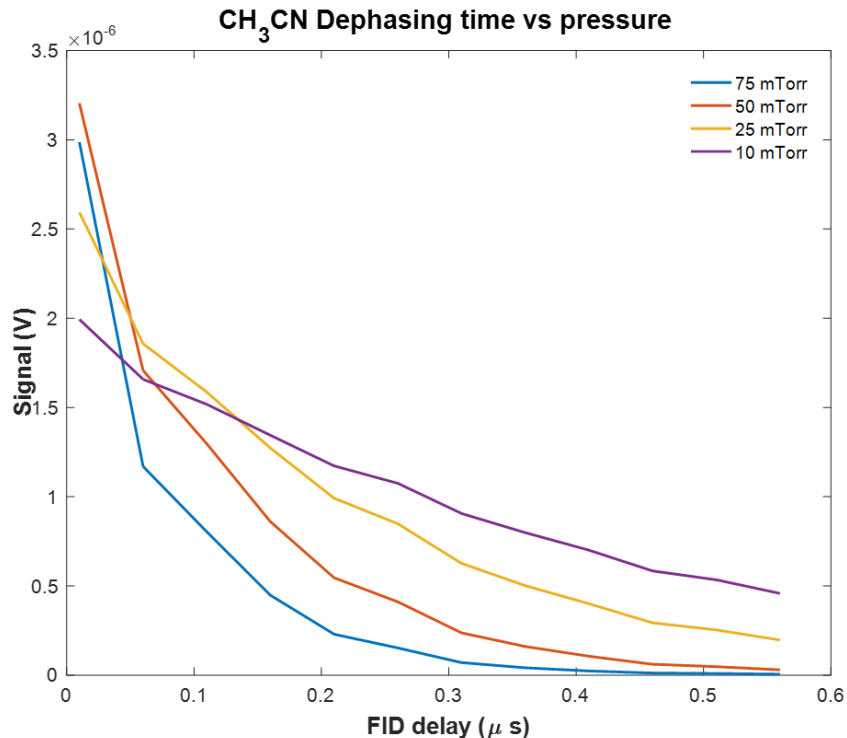


Figure 52: FID of CH_3CN as a function of cell pressure which shows rapid dephasing at higher pressures.

$$\Delta\nu = 2B(J+1) - 4D_J(J+1)^3 - 2D_{Jk}(J+1)k^2 + H_J(J+1)^3[(J+2)^3 - J^3] + 4H_{Jk}(J+1)^3k^2 + 2H_{kJ}(J+1)k^4 \quad (5.3)$$

where (D_J, D_{Jk}, D_k) in kHz and $(H_J, H_{Jk}, H_{kJ}, H_k)$ in Hz represents the quartic and sextic centrifugal distortion terms. Typical value of B is in MHz. Neglecting the centrifugal distortion terms, the lines in the frequency spectrum for different transitions are going to be equally spaced by $\sim 2B$. The reported value of B for CD_3CN is 7857978.7 ± 1 kHz.

With our first mixture measurement, we could observe all the frequencies corresponding to every possible energy transitions for both the chemicals present in the mixture as shown in figure 49. The measurements were done at 20 mTorr and were collected in segments. The acquired data was normalized by the corresponding chirp

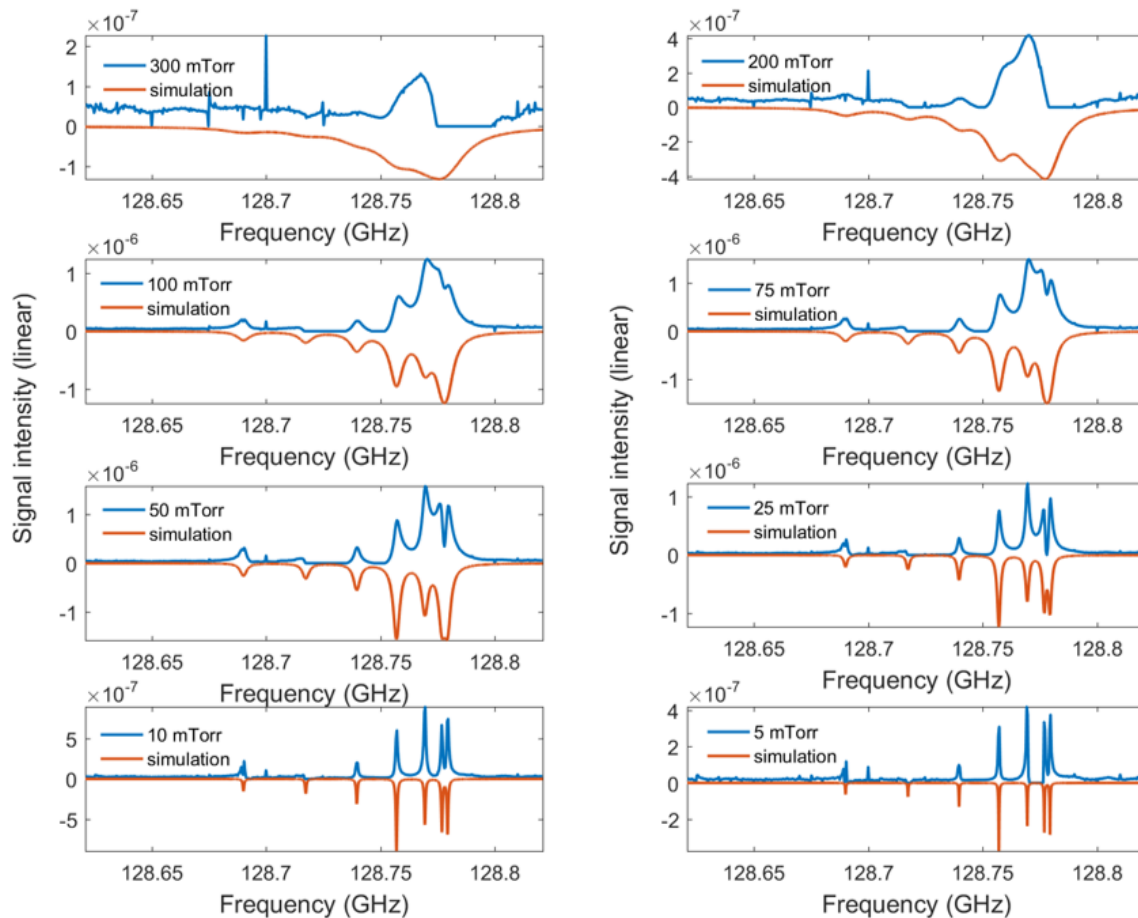


Figure 53: Detection of CH_3CN at varied pressure clearly showing the effect of line broadening.

intensities to do a meaningful comparison of the relative strength in peak intensities. Due to similar nature of the transition dipole moments, the relative peak intensities are similar and agrees with literature reports. The observed frequencies should be multiple of $2B$ and we can verify this by simply multiplying the frequency ($\times 4$) that was observed for CD_3CN ($J = 2 \leftarrow 1, k = (1 \leftarrow 0)$) centered at 31.43 GHz [127-129]. We do see a corresponding peak at 125.72 GHz which further confirms our observation. From figure 50, we could successfully claim simultaneous detection of all three isotopologues present in the mixture through segmented chirp-based measurement of 200 MHz BW. The observed peaks for

CH_3CN and $^{13}CH_3^{13}CN$ completely agrees with the simulated peaks reported in the NASA, Molecular Spectroscopy, JPL database [126] and their relative peak intensities are in accordance with the prepared mixture concentrations.

Now that we have demonstrated the accuracy and mixture analysis capability of the spectrometer, we discuss about the feasibility for real-time infield applications. FPGA-based fast averaging capability of the Guzik digitizer was used for this purpose [130] where 10^6 cycles of 8 μ s duration signal could be acquired and integrated in real-time. This capability was found to drastically reduce the noise in the signal thereby increasing the dynamic range as shown in figure 51. Another important aspect for in-field applications is the ability to perform measurements at higher pressures due to limitation of the pump down capability of portable vacuum pumps which can significantly reduce the dephasing time of FID as shown in figure 52. An estimate of the dephasing time to optimize the minimum inter-pulse interval is required to help speed up acquisition. Figure 53 shows a pressure dependent study of CH_3CN where we could observe transition features at pressure as high as 300 mTorr. However significant line broadening could be observed at higher pressures > 100 mTorr which might call for usage of additional deconvolution and peak fitting algorithms to avoid false identification of closely packed peaks in a gaseous mixture.

5.4. Conclusion

We have demonstrated here the design and operation of a fast-sweep CP-FTMMW spectrometer capable of detecting gaseous molecules in real-time under ambient conditions. The compact design and real-time detection capability clearly provides an advantage for in-field applications particularly for targeted environmental monitoring purposes. The accuracy of the spectrometer has been tested by detecting multiple transition

in C_2H_5OH where observed transition peaks were found to occur within 100 kHz of reported values in the JPL molecular spectroscopy database. Subsequently the spectrometer was successfully able to identify CH_3CN and its isotopologues present in a gaseous mixture at different concentrations. The effect of various design aspects in particular LO leakage and chirp-tailing effect on the spectrometer characteristics has been discussed in detail. To the best of our knowledge, there is no literature data reported so far regarding experimental observation of $(J = 8 \leftarrow 7, k = (7 \leftarrow 0))$ ground state transition in CD_3CN and we believe our observation would be the first known evidence in this regard. Measurements at higher pressure were performed to emulate in-field scenarios where we observed considerable line broadening thereby portraying the need to implement additional data processing functionalities to resolve such complex overlapped spectra. The effect of ultrafast real-time averaging was found to significantly reduce the noise present in the signal thereby increasing the dynamic limit of the system. We are currently working on determining the lower detection limit of the system as well as performing sensitivity analysis, values of which are going to be reported in future publications.

6. CONCLUSIONS AND FUTURE WORK

6.1. Conclusion

The present work investigated the synthesis and development of compact, low-cost and scalable sensors and instrumentations to detect CBRNE signatures in real-time applicable under varied scenarios in the areas of homeland security, environmental monitoring and under various medical and industrial settings. In one embodiment, an alternate detection method by decoupling the sensor material and signal readout electronics has been presented which has the capability to perform long range measurements of ionizing radiation present in the target environment. In_2O_3 nanowires were used as the sensor material and millimeter wave technology was used for stand-off monitoring.

The In_2O_3 nanowires were grown using a carbothermal reduction process following the VLS route using Au as a catalyst. We observed formation of non-uniform diameter In_2O_3 octahedron-like nanoparticles while using indium metal as the source due to high supersaturation ratio of the oxidized indium vapor. An in-depth analysis on our experimental observation of various structural morphologies of nanoparticles instead of nanowires was performed using Wulff shape construction. The nanowires were found to be ~ 100 nm in diameter with evidence of Au nanoparticle at the nanowire tip suggesting growth occurred following the VLS route. HRTEM and SAED characterization revealed nanowire growth along [100] direction and single crystalline properties with cubic crystal structure. Raman scattering investigation showed significant broadening of the phonon mode at 307 cm^{-1} which is associated with the stretching mode in In_2O_3 and is very sensitive to V_O defects. High density of V_O defects was found to be present on the nanowire surface leading to surface stabilization through nanoscale faceting (formation of (111) facets) and

chemisorption of foreign atoms. High resolution XPS and valence band analysis confirmed the presence of chemisorbed oxygen species leading to an upward band bending at the nanowire surface. The VBM to surface Fermi level was determined to 2.15 ± 0.2 eV.

The nature and position of the defect levels due to surface states were further investigated using optical techniques. We observed UV emission from the band-edge and significant NBE PL line width broadening associated with formed V_O^X impurity band at the surface which merges with the conduction band forming a band tail. The optical gap was calculated to be 3.41 eV and activation energies of 6 meV and 75 meV were obtained and related to ionizing energies of donor and acceptor like defects, respectively. An electron concentration of $1.2 \times 10^{20} \text{ cm}^{-3}$ at 10 K was estimated, which is above the degeneracy limit of In_2O_3 , hence positioning the Fermi level 0.05 eV above the CBM. The surface states were found to have a significant influence in carrier trapping mechanism as revealed using ultrafast TA spectroscopy leading to enhanced dielectric properties of In_2O_3 nanowires. Surface passivation treatment by performing high temperature annealing at 700 °C for 2 hrs was further utilized to tune the density of the surface states. Thermal annealing led to significant reduction in the V_O defects as was confirmed by PL and Raman characterization.

Enhanced dielectric behavior of In_2O_3 nanowires and the ability to tune such properties using passivation treatment was further utilized towards stand-off detection of ionizing radiation. A portable low power 94 GHz millimeter wave transceiver was designed for targeted detection. At first, an NIG was used to simulate ionizing radiation conditions and the preliminary test results showed no measurable change in the scattered signal intensity from the as-synthesized samples. This was attributed due to strong EM absorption in these samples due to the presence of high density of surface V_O defects. However, with the

surface passivated samples, we observed detectable change in the scattered signal intensity. Post thermal annealing treatment, due to replenishment of the V_O defects, these samples were more transparent to EM waves. Further, diffusion charging on the nanowire surface resulted in the formation of an electron plasma effectively jamming the surface dipoles and causing enhanced scattering. A fast charging time of ~ 0.5 s and slow discharging time of ~ 10 s was observed. Control measurements without the presence of any In_2O_3 nanowires showed no change in the interrogating signal. Due to short free electron lifetime in air (before they get captured by surrounding molecules), the NIG needed to be placed within 10 cm of the sample for changes to be detected. We further extended our investigation to detect real radioactive source. The In_2O_3 nanowires were exposed to 200 Ci of ^{137}Cs γ -radiation where the dosage was $\sim 40,000$ mr/hr at a distance of 100 cm from the source. We observed in real-time change in the intensity of the scattered signal intensity during irradiation. The signal intensity decreased overtime due to the formation of ionization induced V_O defects in the nanowires leading to higher absorption. Under pre- and post-irradiation conditions, no detectable change in the scattered signal intensity was observed. Thus, in one embodiment, we have successfully demonstrated the use of In_2O_3 nanowires as efficient ionizing radiation sensors which can be used as a part of covertly or overtly deployed tags on target surfaces for stand-off monitoring.

Another important aspect in CBRNE detection is to develop a system for in-field operation which can identify in real-time chemical constituents present in a target atmosphere with high sensitivity and specificity. A prototype fast-sweep WR-08 band CP-FTMMW spectrometer was designed for this purpose having a total BW of 30 GHz (110–140 GHz) and capable of producing ~ 32 mW of average output power over the entire BW.

The system takes advantage of recent progress in the area of solid-state electronics. An AWG was used to produce a low frequency chirp which was then upconverted to the desired BW using AMCs. Various stages of custom designed band pass and band stop filters were used to produce a clean chirp. A pair of 3'' diameter teflon plano-convex lens was used to collimate the transmitted millimeter wave beam inside a 2 L single pass gas cell made from stainless steel having teflon windows and further to focus the outgoing beam onto the receiver. The gas cell has the provision for both liquid and gas sample injection in which the pressure was monitored by a digital vacuum transducer. The receiver was designed to down convert the signal within 13 GHz of the digitizer BW. The high-speed digitizer has the capability to perform real-time averaging which was found to considerably improve the system dynamic range. The accuracy of the spectrometer was tested by performing tests with C_2H_5OH which is known to have rotational lines distributed throughout the entire system BW. The observed transitions were found to lie within 100 kHz of the simulation based on the JPL database. Finally, we report on the analysis of a gaseous mixture containing various isotopologues of CH_3CN present in different concentrations. Thus, in another embodiment of CBRNE detection, a state-of-the-art CP-FTMMW spectrometer is demonstrated which is capable of performing in-field trace gas analysis in real-time.

6.2. Future work

Currently work is under progress to quantify the sensitivity of the spectrometer. Options including double resonance modulation [21], sample pre-concentration [131] and multi-pass cell [25] design are being investigated to improve the system specificity and sensitivity.

The immediate next step is to experimentally demonstrate the feasibility of the proposed ionizing radiation sensing method in long-range detection. Recently demonstrated GaN based PA operating in the 92–96 GHz band having an output power of ~3W from Millitech Inc. can be used at the output of the transmitter to extend the detection range (> 500 m neglecting atmospheric attenuation). A custom designed circulator from Millimeter Wave Products Inc. with high isolation (>30 dB) between port 1 and 3 will be used in conjunction with the PA to protect the receiver. Further, sophisticated detector design based on metal oxide semiconductor nanowires can be envisioned where the sensor material can be integrated into a resonant circuit which acts as the read-out of the ionization induced EM changes [132]. Different mechanisms can then be employed to wirelessly communicate the output of the detector to a remote device such as a central base station.

Another area of interest would be to investigate In_2O_3 nanowires for terahertz applications. Oxide materials possess several terahertz application advantages such as good absorption coefficient, high breakdown voltage and low cost. Very high carrier mobility (> $4000 \text{ cm}^2/\text{Vs}$) can be achieved by careful crystal growth, passivation treatments and device fabrication. V_O defects were found to be most commonly occurring on the surface of the as-synthesized In_2O_3 nanowires. High density of surface states resulted in enhanced carrier trapping thereby reducing the carrier lifetime which is desirable to improve the SNR of the photoconductive terahertz detector fabricated from the same material. However, the carrier mobility also reduces due to increased scattering which negatively affects the current responsivity of the detector. As we have demonstrated here, different surface passivation treatments can be applied to optimize these device parameters for efficient photoconductive detection of terahertz radiation. Time resolved optical pump-terahertz probe spectroscopy

of the In_2O_3 nanowires can be performed for material optimization. This will provide conductivity information from which parameters including peak photoconductivity, lifetime and mobility can be extracted for device characterization which are fabricated from the respective samples. Further, semiconductor nanowires were demonstrated to be efficient terahertz emitters due to the presence of localized surface plasmons [133]. Through surface modification, we have been able to tailor surface resistivity as well as create charge separation in In_2O_3 nanowires which is the key for terahertz emission. Macroscopic time-varying polarization due to separation of photoinduced charge carriers in the nanowires essentially generates the terahertz radiation.

CITED LITERATURE

1. International Technology Roadmap for Semiconductors, available online at <http://public.itrs.net/>.
2. Waldron N, Merckling C, Teugels L, Ong P, Ibrahim SA, Sebaai F, Pourghaderi A, Barla K, Collaert N, Thean AV. InGaAs gate-all-around nanowire devices on 300mm Si substrates. *IEEE Electron Device Letters*. 2014 Nov;35(11):1097-9.
3. Waldron N, Merckling C, Guo W, Ong P, Teugels L, Ansar S, Tsvetanova D, Sebaai F, Van Dorp DH, Milenin A, Lin D. An InGaAs/InP quantum well finfet using the replacement fin process integrated in an RMG flow on 300mm Si substrates. In *VLSI Technology (VLSI-Technology): Digest of Technical Papers, 2014 Symposium on 2014 Jun 9* (pp. 1-2). IEEE.
4. Mertens H, Ritzenthaler R, Hikavyy A, Kim MS, Tao Z, Wostyn K, Chew SA, De Keersgieter A, Mannaert G, Rosseel E, Schram T. Gate-all-around MOSFETs based on vertically stacked horizontal Si nanowires in a replacement metal gate process on bulk Si substrates. In *VLSI Technology, 2016 IEEE Symposium on 2016 Jun 14* (pp. 1-2). IEEE.
5. Nourbakhsh A, Soree B, Heyns M, Agarwal TK, inventors; Katholieke Universiteit Leuven, IMEC vzw, assignee. Bilayer graphene tunneling field effect transistor. United States patent US 9,293,536. 2016 Mar 22.
6. Agarwal T, Yakimets D, Raghavan P, Radu I, Thean A, Heyns M, Dehaene W. Benchmarking of MoS₂ FETs with multigate Si-FET options for 5 nm and beyond. *IEEE Transactions on Electron Devices*. 2015 Dec;62(12):4051-6.
7. Yan R, Gargas D, Yang P. Nanowire photonics. *Nature photonics*. 2009 Oct;3(10):569.
8. Sarkar K, Mukherjee S, Wiederrecht G, Schaller R, Gosztola DJ, Stroschio MA, Dutta M. Ultrafast carrier dynamics and optical pumping of lasing from Ar-plasma treated ZnO nanoribbons. *Nanotechnology*. 2018 Jan 4.
9. Cui Y, Wei Q, Park H, Lieber CM. Nanowire nanosensors for highly sensitive and selective detection of biological and chemical species. *Science*. 2001 Aug 17;293(5533):1289-92.
10. Mukherjee S, Meshik X, Choi M, Farid S, Datta D, Lan Y, Poduri S, Sarkar K, Baterdene U, Huang CE, Wang YY. A graphene and aptamer based liquid gated FET-like electrochemical biosensor to detect adenosine triphosphate. *IEEE transactions on nanobioscience*. 2015 Dec;14(8):967-72.

CITED LITERATURE (continued)

11. Farid S, Meshik X, Choi M, Mukherjee S, Lan Y, Parikh D, Poduri S, Batedene U, Huang CE, Wang YY, Burke P. Detection of Interferon gamma using graphene and aptamer based FET-like electrochemical biosensor. *Biosensors and Bioelectronics*. 2015 Sep 15;71:294-9.
12. Datta D, Meshik X, Mukherjee S, Sarkar K, Choi MS, Mazouchi M, Farid S, Wang YY, Burke PJ, Dutta M, Stroschio MA. Submillimolar Detection of Adenosine Monophosphate Using Graphene-Based Electrochemical Aptasensor. *IEEE Transactions on Nanotechnology*. 2017 Mar;16(2):196-202.
13. Datta D, Sarkar K, Mukherjee S, Meshik X, Stroschio MA, Dutta M. Graphene oxide and DNA aptamer based sub-nanomolar potassium detecting optical nanosensor. *Nanotechnology*. 2017 Jul 18;28(32):325502.
14. Meshik X, Farid S, Choi M, Lan Y, Mukherjee S, Datta D, Dutta M, Stroschio MA. Biomedical Applications of Quantum Dots, Nucleic Acid- Based Aptamers, and Nanostructures in Biosensors. *Critical Reviews™ in Biomedical Engineering*. 2015;43(4).
15. Hochbaum AI, Chen R, Delgado RD, Liang W, Garnett EC, Najarian M, Majumdar A, Yang P. Enhanced thermoelectric performance of rough silicon nanowires. *Nature*. 2008 Jan;451(7175):163.
16. Zhang D, Liu Z, Li C, Tang T, Liu X, Han S, Lei B, Zhou C. Detection of NO₂ down to ppb levels using individual and multiple In₂O₃ nanowire devices. *Nano letters*. 2004 Oct 13;4(10):1919-24.
17. Wan Q, Li QH, Chen YJ, Wang TH, He XL, Li JP, Lin CL. Fabrication and ethanol sensing characteristics of ZnO nanowire gas sensors. *Applied Physics Letters*. 2004 May 3;84(18):3654-6.
18. Kolmakov A, Klenov DO, Lilach Y, Stemmer S, Moskovits M. Enhanced gas sensing by individual SnO₂ nanowires and nanobelts functionalized with Pd catalyst particles. *Nano Letters*. 2005 Apr 13;5(4):667-73.
19. Yan D, Cheng S, Zhuo RF, Chen JT, Feng JJ, Feng HT, Li HJ, Wu ZG, Wang J, Yan PX. Nanoparticles and 3D sponge-like porous networks of manganese oxides and their microwave absorption properties. *Nanotechnology*. 2009 Feb 17;20(10):105706.
20. Wolfbeis OS. Sensor paints. *Advanced Materials*. 2008 Oct 2;20(19):3759-63.

CITED LITERATURE (continued)

21. Gopalsami N, Chien HT, Heifetz A, Koehl ER, Raptis AC. Millimeter wave detection of nuclear radiation: An alternative detection mechanism. *Review of scientific instruments*. 2009 Aug;80(8):084702.
22. Gopalsami N, Heifetz A, Chien HT, Liao S, Koehl ER, Raptis AC, inventors; UChicago Argonne LLC, assignee. Radar detection of radiation-induced ionization in air. United States patent US 9,086,487. 2015 Jul 21.
23. Gopalsami N, Bakhtiari S, Raptis AC, Elmer TW, inventors; UChicago Argonne LLC, assignee. Passive millimeter wave spectrometer for remote detection of chemical plumes. United States patent US 7,495,218. 2009 Feb 24.
24. Bakhtiari S, Elmer TW, Cox NM, Gopalsami N, Raptis AC, Liao S, Mikhelson I, Sahakian AV. Compact millimeter-wave sensor for remote monitoring of vital signs. *IEEE Transactions on Instrumentation and Measurement*. 2012 Mar;61(3):830-41.
25. Barnowski R, Gopalsami N. REMOTE DETECTION OF RADIOACTIVE PLUMES USING MILLIMETER WAVE TECHNOLOGY. *Journal of Undergraduate Research*. 2009 Jan 1;9.
26. Gopalsami N, Raptis AC. Millimeter-wave radar sensing of airborne chemicals. *IEEE Transactions on Microwave Theory and Techniques*. 2001 Apr;49(4):646-53.
27. Sprangle P, Hafizi B, Milchberg H, Nusinovich G, Zigler A. Active remote detection of radioactivity based on electromagnetic signatures. *Physics of Plasmas*. 2014 Jan;21(1):013103.
28. Kim D, Yu D, Sawant A, Choe MS, Lee I, Kim SG, Choi E. Remote detection of radioactive material using high-power pulsed electromagnetic radiation. *Nature communications*. 2017 May 9;8:15394.
29. Christensen SD. Microwave Detection of Chemical Agents: A Review. *CHEMICAL RESEARCH DEVELOPMENT AND ENGINEERING CENTER ABERDEEN PROVING GROUND*; 1986 Jun.
30. Gopalsami N, Bakhtiari S, Raptis AC, Dieckman SL, DeLucia FC. Millimeter-wave measurements of molecular spectra with application to environmental monitoring. *IEEE transactions on instrumentation and measurement*. 1996 Feb;45(1):225-30.
31. Hays BM, McCabe MN, Shipman ST, Widicus Weaver SL. Fast sweep direct absorption (sub) millimeter-wave spectroscopy. *Review of Scientific Instruments*. 2016 Nov;87(11):113109.

CITED LITERATURE (continued)

32. Brown GG, Dian BC, Douglass KO, Geyer SM, Shipman ST, Pate BH. A broadband Fourier transform microwave spectrometer based on chirped pulse excitation. *Review of Scientific Instruments*. 2008 May;79(5):053103.
33. Brown GG, Dian BC, Douglass KO, Geyer SM, Pate BH. The rotational spectrum of epifluorohydrin measured by chirped-pulse Fourier transform microwave spectroscopy. *Journal of Molecular Spectroscopy*. 2006 Aug 1;238(2):200-12.
34. Dian BC, Brown GG, Douglass KO, Pate BH. Measuring picosecond isomerization kinetics via broadband microwave spectroscopy. *Science*. 2008 May 16;320(5878):924-8.
35. Minami T. Transparent conducting oxide semiconductors for transparent electrodes. *Semiconductor science and technology*. 2005 Mar 15;20(4):S35.
36. Phillips JM, Cava RJ, Thomas GA, Carter SA, Kwo J, Siegrist T, Krajewski JJ, Marshall JH, Peck Jr WF, Rapkine DH. Zinc-indium-oxide: a high conductivity transparent conducting oxide. *Applied Physics Letters*. 1995 Oct 9;67(15):2246-8.
37. Farid S, Mukherjee S, Sarkar K, Mazouchi M, Stroschio MA, Dutta M. Enhanced optical properties due to indium incorporation in zinc oxide nanowires. *Applied Physics Letters*. 2016 Jan 11;108(2):021106.
38. Zhang D, Li C, Liu X, Han S, Tang T, Zhou C. Doping dependent NH₃ sensing of indium oxide nanowires. *Applied Physics Letters*. 2003 Sep 1;83(9):1845-7.
39. Cao H, Qiu X, Liang Y, Zhu Q, Zhao M. Room-temperature ultraviolet-emitting In₂O₃ nanowires. *Applied physics letters*. 2003 Jul 28;83(4):761-3.
40. Hafeez M, Zhai T, Bhatti AS, Bando Y, Golberg D. Oxygen vacancy driven modulations in In₂O₃ pyramidal beaded nanowires. *Crystal Growth & Design*. 2012 Sep 11;12(10):4935-43.
41. Ho CH, Chan CH, Tien LC, Huang YS. Direct optical observation of band-edge excitons, band gap, and Fermi level in degenerate semiconducting oxide nanowires In₂O₃. *The Journal of Physical Chemistry C*. 2011 Nov 28;115(50):25088-96.
42. Agoston P, Albe K. Thermodynamic stability, stoichiometry, and electronic structure of bcc-In₂O₃ surfaces. *Physical Review B*. 2011 Jul 15;84(4):045311.
43. King PD, Veal TD, Fuchs F, Wang CY, Payne DJ, Bourlange A, Zhang H, Bell GR, Cimalla V, Ambacher O, Egdell RG. Band gap, electronic structure, and surface electron accumulation of cubic and rhombohedral In₂O₃. *Physical Review B*. 2009 May 29;79(20):205211.

CITED LITERATURE (continued)

44. Walsh A, Da Silva JL, Wei SH, Körber C, Klein A, Piper LF, DeMasi A, Smith KE, Panaccione G, Torelli P, Payne DJ. Nature of the band gap of In₂O₃ revealed by first-principles calculations and X-ray spectroscopy. *Physical Review Letters*. 2008 Apr 25;100(16):167402.
45. Bourlange A, Payne DJ, Egdell RG, Foord JS, Edwards PP, Jones MO, Schertel A, Dobson PJ, Hutchison JL. Growth of In₂O₃ (100) on Y-stabilized ZrO₂ (100) by O-plasma assisted molecular beam epitaxy. *Applied Physics Letters*. 2008 Mar 3;92(9):092117.
46. Bierwagen O. Indium oxide—a transparent, wide-band gap semiconductor for (opto) electronic applications. *Semiconductor Science and Technology*. 2015 Jan 19;30(2):024001.
47. Karazhanov SZ, Ravindran P, Vajeeston P, Ulyashin A, Finstad TG, Fjellvåg H. Phase stability, electronic structure, and optical properties of indium oxide polytypes. *Physical Review B*. 2007 Aug 29;76(7):075129.
48. Hao Y, Meng G, Ye C, Zhang L. Controlled synthesis of In₂O₃ octahedrons and nanowires. *Crystal growth & design*. 2005 Jul 6;5(4):1617-21.
49. Jean ST, Her YC. Growth mechanism and photoluminescence properties of In₂O₃ nanotowers. *Crystal Growth & Design*. 2010 Apr 12;10(5):2104-10.
50. Yan YG, Zhang Y, Zeng HB, Zhang LD. In₂O₃ nanotowers: controlled synthesis and mechanism analysis. *Crystal growth & design*. 2007 May 2;7(5):940-3.
51. Tasker PW. The stability of ionic crystal surfaces. *Journal of Physics C: Solid State Physics*. 1979 Nov 28;12(22):4977.
52. Egdell RG. Dopant and defect induced electronic states at In₂O₃ surfaces. *In: Defects at Oxide Surfaces 2015* (pp. 351-400). Springer, Cham.
53. Kar A, Stroschio MA, Dutta M, Kumari J, Meyyappan M. Observation of ultraviolet emission and effect of surface states on the luminescence from tin oxide nanowires. *Applied Physics Letters*. 2009 Mar 9;94(10):101905.
54. Nguyen P, Vaddiraju S, Meyyappan M. Indium and tin oxide nanowires by vapor-liquid-solid growth technique. *Journal of electronic materials*. 2006 Feb 1;35(2):200-6.
55. Kar A, Stroschio MA, Meyyappan M, Gosztola DJ, Wiederrecht GP, Dutta M. Tailoring the surface properties and carrier dynamics in SnO₂ nanowires. *Nanotechnology*. 2011 Jun 8;22(28):285709.

CITED LITERATURE (continued)

56. Chambers SA, Droubay T, Kaspar TC, Gutowski M. Experimental determination of valence band maxima for SrTiO₃, TiO₂, and SrO and the associated valence band offsets with Si (001). *Journal of Vacuum Science & Technology B: Microelectronics and Nanometer Structures Processing, Measurement, and Phenomena*. 2004 Jul;22(4):2205-15.
57. Harvey SP, Mason TO, Gassenbauer Y, Schafrank R, Klein A. Surface versus bulk electronic/defect structures of transparent conducting oxides: I. Indium oxide and ITO. *Journal of Physics D: Applied Physics*. 2006 Sep 1;39(18):3959.
58. Robert F 2003 Pierret: *Semiconductor device fundamentals* (Reading, MA: Addison-Wesley)
59. Li C, Zhang D, Lei B, Han S, Liu X, Zhou C. Surface treatment and doping dependence of In₂O₃ nanowires as ammonia sensors. *The Journal of Physical Chemistry B*. 2003 Nov 13;107(45):12451-5.
60. Karazhanov SZ, Ravindran P, Vajeeston P, Ulyashin A, Finstad TG, Fjellvåg H. Phase stability, electronic structure, and optical properties of indium oxide polytypes. *Physical Review B*. 2007 Aug 29;76(7):075129.
61. Reunchan P, Zhou X, Limpijumngong S, Janotti A, Van de Walle CG. Vacancy defects in indium oxide: An ab-initio study. *Current Applied Physics*. 2011 May 1;11(3):S296-300.
62. Liu J, Liu T, Liu F, Li H. Thermodynamics of native defects in In₂O₃ crystals using a first-principles method. *RSC Advances*. 2014;4(70):36983-9.
63. Kar A. *Defect Passivation in Nanowires and Demonstration of Nanowire Devices for use in Sensing Applications* (Doctoral dissertation, University of Illinois at Chicago).
64. Vanheusden K, Warren WL, Seager CH, Tallant DR, Voigt JA, Gnade BE. Mechanisms behind green photoluminescence in ZnO phosphor powders. *Journal of Applied Physics*. 1996 May 15;79(10):7983-90.
65. Walsh A. Surface oxygen vacancy origin of electron accumulation in indium oxide. *Applied Physics Letters*. 2011 Jun 27;98(26):261910.
66. Dagotto E. Condensed-matter physics: The conducting face of an insulator. *Nature*. 2011 Jan;469(7329):167.
67. Mukherjee S, Sarkar K, Wiederrecht GP, Schaller RD, Gosztola DJ, Stroschio MA, Dutta M. Defect induced structural inhomogeneity, ultraviolet light emission and

CITED LITERATURE (continued)

- near-band-edge photoluminescence broadening in degenerate In₂O₃ nanowires. *Nanotechnology*. 2018 Mar 1;29(17):175201.
68. Wei ZP, Guo DL, Liu B, Chen R, Wong LM, Yang WF, Wang SJ, Sun HD, Wu T. Ultraviolet light emission and excitonic fine structures in ultrathin single-crystalline indium oxide nanowires. *Applied Physics Letters*. 2010 Jan 18;96(3):031902.
 69. Varshni YP. Temperature dependence of the energy gap in semiconductors. *physica*. 1967 Jan 1;34(1):149-54.
 70. Baranskii PI, Elizarov AI. The Carrier Concentration Dependence of the Debye Temperature θ in Heavily Doped n-Ge. *physica status solidi (b)*. 1972 Sep 1;53(1).
 71. He HP, Wang Z, Duan HF, Ye ZZ. Band tail-induced photoluminescence broadening in heavily In-doped n-type ZnO nanowires. *Physical Chemistry Chemical Physics*. 2015;17(27):17552-6.
 72. Yoshikawa M, Kunzer M, Wagner J, Obloh H, Schlotter P, Schmidt R, Herres N, Kaufmann U. Band-gap renormalization and band filling in Si-doped GaN films studied by photoluminescence spectroscopy. *Journal of applied physics*. 1999 Oct 15;86(8):4400-2.
 73. Morgan TN. Broadening of impurity bands in heavily doped semiconductors. *Physical Review*. 1965 Jul 5;139(1A):A343.
 74. Zhu Q, Xie C, Li H, Yang C, Zhang S, Zeng D. Selectively enhanced UV and NIR photoluminescence from a degenerate ZnO nanorod array film. *Journal of Materials Chemistry C*. 2014;2(23):4566-80.
 75. Iliopoulos E, Doppalapudi D, Ng HM, Moustakas TD. Broadening of near-band-gap photoluminescence in n-GaN films. *Applied physics letters*. 1998 Jul 20;73(3):375-7.
 76. Prasankumar RP, Upadhy PC, Taylor AJ. Ultrafast carrier dynamics in semiconductor nanowires. *physica status solidi (b)*. 2009 Sep 1;246(9):1973-95.
 77. Othonos A, Zervos M, Tsokkou D. Femtosecond carrier dynamics in In₂O₃ nanocrystals. *Nanoscale research letters*. 2009 Jun 1;4(6):526.
 78. Tsokkou D, Othonos A, Zervos M. Ultrafast time-resolved spectroscopy of In₂O₃ nanowires. *Journal of Applied Physics*. 2009 Oct 15;106(8):084307.

CITED LITERATURE (continued)

79. Othonos A, Zervos M, Tsokkou D. Tin oxide nanowires: the influence of trap states on ultrafast carrier relaxation. *Nanoscale research letters*. 2009 Aug 1;4(8):828.
80. Zhang P, Tevaarwerk E, Park BN, Savage DE, Celler GK, Knezevic I, Evans PG, Eriksson MA, Lagally MG. Electronic transport in nanometre-scale silicon-on-insulator membranes. *Nature*. 2006 Feb;439(7077):703.
81. Li M, Xing G, Qune LF, Xing G, Wu T, Huan CH, Zhang X, Sum TC. Tailoring the charge carrier dynamics in ZnO nanowires: the role of surface hole/electron traps. *Physical Chemistry Chemical Physics*. 2012;14(9):3075-82.
82. Kar A, Yang J, Dutta M, Stroschio MA, Kumari J, Meyyappan M. Rapid thermal annealing effects on tin oxide nanowires prepared by vapor-liquid-solid technique. *Nanotechnology*. 2009 Jan 15;20(6):065704.
83. Donley C, Dunphy D, Paine D, Carter C, Nebesny K, Lee P, Alloway D, Armstrong NR. Characterization of Indium-Tin oxide interfaces using X-ray photoelectron spectroscopy and redox processes of a chemisorbed probe molecule: effect of surface pretreatment conditions. *Langmuir*. 2002 Jan 22;18(2):450-7.
84. Barsan N, Weimar U. Understanding the fundamental principles of metal oxide based gas sensors; the example of CO sensing with SnO₂ sensors in the presence of humidity. *Journal of Physics: Condensed Matter*. 2003 May 12;15(20):R813.
85. Knoll GF. *Radiation detection and measurement*. John Wiley & Sons; 2010 Aug 16.
86. Brooks FD. A scintillation counter with neutron and gamma-ray discriminators. *Nuclear Instruments and Methods*. 1959 Apr 1;4(3):151-63.
87. Kar A, Ahern R, Gopalsami N, Raptis AC, Stroschio MA, Dutta M. Preliminary investigation on the modification of electronic properties in surface passivated SnO₂ nanowires with Schottky contacts on being exposed to ¹³⁷Cs γ -radiation. *Journal of Applied Physics*. 2012 Apr 15;111(8):084319.
88. Elokhin AP, Kononov EN. Application of radar stations for detecting radioactive emissions at nuclear power plants. *Atomic Energy*. 1996 Feb 1;80(2):135-42.
89. K. A. Boyarchuk, E. N. Kononov, and G. A. Lyakhov, "Radar detection of regions of local ionization in layers of the atmosphere near the ground," *Pis'ma Zh. Tekh. Fiz.*, 19, No. 6, 67-73 (1993)
90. T. W. Elmer, S. Bakhtiari, N. Gopalsami private communication Oct 2016.

CITED LITERATURE (continued)

91. McCloy JS, Jones AM, Kelly JF, Riley BJ, Jiang W, McMakin D. Exploiting Novel Radiation-Induced Electromagnetic Material Changes for Remote Detection and Monitoring: Final Progress Report. Pacific Northwest National Laboratory Richland United States; 2016 Apr 1.
92. McCloy JS, Jordan DV, Kelly JF, McMakin DL, Johnson BR, Campbell LW. Electromagnetic material changes for remote detection and monitoring: a feasibility study: Progress report. Pacific Northwest National Laboratory (PNNL), Richland, WA (US); 2009 Sep 1.
93. http://en.wikipedia.org/wiki/Ionizing_radiation
94. Tepper T, Berger S. Correlation between microstructure, particle size, dielectric constant, and electrical resistivity of nano-size amorphous SiO₂ powder. Nanostructured materials. 1999 Nov 1;11(8):1081-9.
95. Mo CM, Zhang L, Wang G. Characteristics of dielectric behavior in nanostructured materials. Nanostructured Materials. 1995 Jan 1;6(5-8):823-6.
96. Nalwa H S 2004 Encyclopedia of Nanoscience and Nanotechnology vol 2 (Stevenson Ranch, CA: American Scientific Publishers) pp 371–87
97. N. Gopalsami private communication Sept 2016.
98. Arshak K, Korostynska O. Thin film pn-junctions based on oxide materials as γ -radiation sensors. Sensors and Actuators A: Physical. 2004 Aug 16;113(3):307-11..
99. Mayo DC, Nolen JR, Cook A, Mu RR, Haglund RF. Zinc oxide nanowire gamma ray detector with high spatiotemporal resolution. In Synthesis and Photonics of Nanoscale Materials XIII 2016 Mar 9 (Vol. 9737, p. 97370I). International Society for Optics and Photonics.
100. Park GB, Field RW. Perspective: The first ten years of broadband chirped pulse Fourier transform microwave spectroscopy. The Journal of chemical physics. 2016 May 28;144(20):200901.
101. Colombo AP. Chirped-pulse millimeter-wave spectroscopy, dynamics, and manipulation of Rydberg-Rydberg Transitions (Doctoral dissertation, Massachusetts Institute of Technology).
102. Prozument K, Colombo AP, Zhou Y, Park GB, Petrović VS, Coy SL, Field RW. Chirped-pulse millimeter-wave spectroscopy of Rydberg-Rydberg transitions. Physical review letters. 2011 Sep 26;107(14):143001.

CITED LITERATURE (continued)

103. Spectroscopy From Space, NATO Science Series: II. Mathematics, Physics and Chemistry, Vol. 20, edited by J. Demaisen, K. Sarka, E. A. Cohen (Kluwer Academic, Dordrecht, The Netherlands, 2000).
104. Leskovar B, Kolbe WF. Detection and measurements of air pollutants and constituents by millimeter-wave microwave spectroscopy. *IEEE Transactions on Nuclear Science*. 1979 Feb;26(1):780-90.
105. Kolbe WF, Leskovar B. 140 GHz microwave spectrometer for the detection of gaseous chemical species. *International journal of infrared and millimeter waves*. 1983 Sep 1;4(5):733-49.
106. Dumesh BS, Gorbatenkov VD, Koloshnikov VG, Panfilov VA, Surin LA. Application of highly sensitive millimeter-wave cavity spectrometer based on orotron for gas analysis. *Spectrochimica Acta Part A: Molecular and Biomolecular Spectroscopy*. 1997 Jun 1;53(6):835-43.
107. Medvedev IR, Behnke M, De Lucia FC. Fast analysis of gases in the submillimeter/terahertz with "absolute" specificity. *Applied physics letters*. 2005 Apr 11;86(15):154105.
108. Medvedev I, Winnewisser M, De Lucia FC, Herbst E, Białkowska-Jaworska E, Pszczółkowski L, Kisiel Z. The millimeter-and submillimeter-wave spectrum of the trans-gauche conformer of diethyl ether. *Journal of Molecular Spectroscopy*. 2004 Dec 1;228(2):314-28.
109. Somers RM, Poehler TO, Wagner PE. Microwave time domain Fabry-Perot emission spectrometer. *Review of Scientific Instruments*. 1975 Jun;46(6):719-25.
110. Balle TJ, Campbell EJ, Keenan MR, Flygare WH. A new method for observing the rotational spectra of weak molecular complexes: KrHCl. *The Journal of Chemical Physics*. 1980 Jan 15;72(2):922-32.
111. Balle TJ, Flygare WH. Fabry-Perot cavity pulsed Fourier transform microwave spectrometer with a pulsed nozzle particle source. *Review of Scientific Instruments*. 1981 Jan;52(1):33-45.
112. Campbell EJ, Buxton LW, Balle TJ, Flygare WH. The theory of pulsed Fourier transform microwave spectroscopy carried out in a Fabry-Perot cavity: Static gas. *The Journal of Chemical Physics*. 1981 Jan 15;74(2):813-28.
113. Grabow JU, Palmer ES, McCarthy MC, Thaddeus P. Supersonic-jet cryogenic-resonator coaxially oriented beam-resonator arrangement Fourier transform

CITED LITERATURE (continued)

- microwave spectrometer. Review of scientific instruments. 2005 Sep;76(9):093106.
114. Kolbe WF, Leskovar B. Pulsed millimeter wave fourier transform microwave spectrometer. International journal of infrared and millimeter waves. 1986 Sep 1;7(9):1329-38.
 115. Boucher D, Bocquet R, Petitprez D, Aime L. Molecular beam millimeter sidebands Fourier transform spectrometer (MB-MMSBFT). International journal of infrared and millimeter waves. 1994 Sep 1;15(9):1481-96.
 116. Yamamoto S, Habara H, Kim E, Nagasaka H. Fourier transform millimeter-wave spectroscopy of chlorocarbene (HCCl). The Journal of Chemical Physics. 2001 Oct 1;115(13):6007-11.
 117. Habara H, Yamamoto S, Ochsenfeld C, Head-Gordon M, Kaiser RI, Lee YT. Fourier transform millimeter-wave spectroscopy of the HCS radical in the 2 A' ground electronic state. The Journal of chemical physics. 1998 Jun 1;108(21):8859-63.
 118. Steber AL, Harris BJ, Neill JL, Pate BH. An arbitrary waveform generator based chirped pulse Fourier transform spectrometer operating from 260 to 295 GHz. Journal of Molecular Spectroscopy. 2012 Oct 1;280:3-10.
 119. Park GB, Steeves AH, Kuyanov-Prozument K, Neill JL, Field RW. Design and evaluation of a pulsed-jet chirped-pulse millimeter-wave spectrometer for the 70–102 GHz region. The Journal of chemical physics. 2011 Jul 14;135(2):024202.
 120. Harris BJ, Pulliam RL, Neill JL, Muckle MT, Reynolds R, Pate BH. Fourier transform molecular rotational resonance spectroscopy for reprogrammable chemical sensing. In Terahertz, RF, Millimeter, and Submillimeter-Wave Technology and Applications VIII 2015 Mar 14 (Vol. 9362, p. 936215). International Society for Optics and Photonics.
 121. <https://www.guzik.com/products/general-purpose-and-specialized-solutions/digitizers>
 122. Medvedev IR, Neese CF, Plummer GM, De Lucia FC. Submillimeter spectroscopy for chemical analysis with absolute specificity. Optics letters. 2010 May 15;35(10):1533-5.
 123. <https://www.vadiodes.com/en/>

CITED LITERATURE (continued)

124. Gerecht E, Douglass KO, Plusquellic DF. Chirped-pulse terahertz spectroscopy for broadband trace gas sensing. *Optics Express*. 2011 Apr 25;19(9):8973-84.
125. Motamedi M, Moradi P. Determination of Rotational Parameters of CH₃CN, CD₃CN and their Different Isotopic Species in the Ground and $v_4=1$ States. *Journal of Chemistry*. 2009;6(2):577-93.
126. <https://spec.jpl.nasa.gov>
127. Masoud M, Parinaz M. Theoretical Study of Rotational Spectroscopy of Acetonitrile-d₃ in the Ground and Different Excited Vibrational States. *Journal of Chemistry*. 2008;5(2):201-18.
128. Murray AM, Kukolich SG. Beam maser spectroscopy on CD₃CN. *The Journal of Chemical Physics*. 1983 Mar 15;78(6):3557-9.
129. Masri FN, Duncan JL, Speirs GK. Vibration-rotation spectra of CD₃CN. *Journal of Molecular Spectroscopy*. 1973 Jul 1;47(1):163-78.
130. Stein A, Volfbeyn SP, inventors; Guzik Technical Enterprises, assignee. Digital equalization of multiple interleaved analog-to-digital converters. United States patent US 7,408,495. 2008 Aug 5.
131. Neese CF, Medvedev IR, Plummer GM, Frank AJ, Ball CD, De Lucia FC. Compact submillimeter/terahertz gas sensor with efficient gas collection, preconcentration, and ppt sensitivity. *IEEE Sensors Journal*. 2012 Aug;12(8):2565-74.
132. Burger R, Nuspl S, Spitzer R, Wuori E, Zieber F, inventors; Integrated Magnetolectronics Corp, assignee. Radiation detector having all-metal circuitry operation of which is based on electron spin. United States patent US 7,220,968. 2007 May 22.
133. Jung GB, Cho YJ, Myung Y, Kim HS, Seo YS, Park J, Kang C. Geometry-dependent terahertz emission of silicon nanowires. *Optics express*. 2010 Aug 2;18(16):16353-9.

APPENDICES

APPENDIX: A

4/1/2018

Rightslink® by Copyright Clearance Center



RightsLink®

[Home](#)
[Create Account](#)
[Help](#)


Title: A Graphene and Aptamer Based Liquid Gated FET-Like Electrochemical Biosensor to Detect Adenosine Triphosphate

Author: Souvik Mukherjee

Publication: NanoBioscience, IEEE Transactions on

Publisher: IEEE

Date: Dec. 2015

Copyright © 2015, IEEE

LOGIN

If you're a **copyright.com user**, you can login to RightsLink using your copyright.com credentials.

Already a **RightsLink user** or want to [learn more?](#)

Thesis / Dissertation Reuse

The IEEE does not require individuals working on a thesis to obtain a formal reuse license, however, you may print out this statement to be used as a permission grant:

Requirements to be followed when using any portion (e.g., figure, graph, table, or textual material) of an IEEE copyrighted paper in a thesis:

- 1) In the case of textual material (e.g., using short quotes or referring to the work within these papers) users must give full credit to the original source (author, paper, publication) followed by the IEEE copyright line © 2011 IEEE.
- 2) In the case of illustrations or tabular material, we require that the copyright line © [Year of original publication] IEEE appear prominently with each reprinted figure and/or table.
- 3) If a substantial portion of the original paper is to be used, and if you are not the senior author, also obtain the senior author's approval.

Requirements to be followed when using an entire IEEE copyrighted paper in a thesis:

- 1) The following IEEE copyright/ credit notice should be placed prominently in the references: © [year of original publication] IEEE. Reprinted, with permission, from [author names, paper title, IEEE publication title, and month/year of publication]
- 2) Only the accepted version of an IEEE copyrighted paper can be used when posting the paper or your thesis on-line.
- 3) In placing the thesis on the author's university website, please display the following message in a prominent place on the website: In reference to IEEE copyrighted material which is used with permission in this thesis, the IEEE does not endorse any of [university/educational entity's name goes here]'s products or services. Internal or personal use of this material is permitted. If interested in reprinting/republishing IEEE copyrighted material for advertising or promotional purposes or for creating new collective works for resale or redistribution, please go to http://www.ieee.org/publications_standards/publications/rights/rights_link.html to learn how to obtain a License from RightsLink.

If applicable, University Microfilms and/or ProQuest Library, or the Archives of Canada may supply single copies of the dissertation.

APPENDIX: BIOP Publishing LICENSE
TERMS AND CONDITIONS

Apr 19, 2018

This is a License Agreement between Souvik Mukherjee ("You") and IOP Publishing ("IOP Publishing") provided by Copyright Clearance Center ("CCC"). The license consists of your order details, the terms and conditions provided by IOP Publishing, and the payment terms and conditions.

All payments must be made in full to CCC. For payment instructions, please see information listed at the bottom of this form.

License Number	4332530249670
License date	Apr 04, 2018
Licensed content publisher	IOP Publishing
Licensed content title	Nanotechnology
Licensed content date	Jan 1, 1990
Type of Use	Thesis/Dissertation
Requestor type	Author of requested content
Format	Electronic
Portion	chapter/article

The requesting Souvik Mukherjee person/organization is:

Title or numeric reference of Entire article
the portion(s)

Title of the article or chapter the portion is from Defect induced structural inhomogeneity, ultraviolet light emission and near-band-edge photoluminescence broadening in degenerate In₂O₃ nanowires

Editor of portion(s)	N/A
Author of portion(s)	Self
Volume of serial or monograph.	29
Issue, if republishing an article from a serial	17
Page range of the portion	
Publication date of portion	2018/3/1
Rights for	Main product
Duration of use	Life of current and all future editions

APPENDIX: B (continued)

Creation of copies for the disabled no

With minor editing privileges yes

For distribution to Worldwide

In the following language(s) Original language of publication

With incidental promotional
no use

The lifetime unit quantity of Up to 499
new product

Title Sensors and instrumentations for real-time detection and monitoring
of chemical signatures: from the macroscopic to nanoscale

Instructor name Mitra Dutta

Institution name University of Illinois at Chicago

Expected presentation date Apr 2018

Billing Type Invoice

Billing Address Souvik Mukherjee
851 S Morgan St
MC 154

Chicago, IL 60607
United States
Attn: Souvik Mukherjee

Total (may include CCC user 0.00 USD fee)

Terms and Conditions

TERMS AND CONDITIONS

The following terms are individual to this publisher:

These special terms and conditions are in addition to the standard terms and conditions for CCC's Republication Service and, together with those standard terms and conditions, govern the use of the Works.

As the "User" you will make all reasonable efforts to contact the author(s) of the article which the Work is to be reused from, to seek consent for your intended use. Contacting one author who is acting expressly as authorised agent for their co-author(s) is acceptable. User will reproduce the following wording prominently alongside the Work:

- the source of the Work, including author, article title, title of journal, volume number, issue number (if relevant), page range (or first page if this is the only information available) and date of first publication. This information can be contained in a footnote or reference note; and a link back to the article (via DOI);
- and
-

APPENDIX: B (continued)

if practicable, and IN ALL CASES for new works published under any of the Creative Commons licences, the words “© IOP Publishing. Reproduced with permission. All rights reserved”

Without the express permission of the author(s) and the Rightsholder of the article from which the Work is to be reused, User shall not use it in any way which, in the opinion of the Rightsholder, could: (i) distort or alter the author(s)' original intention(s) and meaning; (ii) be prejudicial to the honour or reputation of the author(s); and/or (iii) imply endorsement by the author(s) and/or the Rightsholder.

This licence does not apply to any article which is credited to another source and which does not have the copyright line ‘© IOP Publishing Ltd’. User must check the copyright line of the article from which the Work is to be reused to check that IOP Publishing Ltd has all the necessary rights to be able to grant permission. User is solely responsible for identifying and obtaining separate licences and permissions from the copyright owner for reuse of any such third party material/figures which the Rightsholder is not the copyright owner of. The Rightsholder shall not reimburse any fees which User pays for a republication license for such third party content.

This licence does not apply to any material/figure which is credited to another source in the

Rightsholder's publication or has been obtained from a third party. User must check the Version of Record of the article from which the Work is to be reused, to check whether any of the material in the Work is third party material. Third party citations and/or copyright notices and/or permissions statements may not be included in any other version of the article from which the Work is to be reused and so cannot be relied upon by the User. User is solely responsible for identifying and obtaining separate licences and permissions from the copyright owner for reuse of any such third party material/figures where the Rightsholder is not the copyright owner. The Rightsholder shall not reimburse any fees which User pays for a republication license for such third party content.

User and CCC acknowledge that the Rightsholder may, from time to time, make changes or additions to these special terms and conditions without express notification, provided that these shall not apply to permissions already secured and paid for by User prior to such change or addition.

User acknowledges that the Rightsholder (which includes companies within its group and third parties for whom it publishes its titles) may make use of personal data collected through the service in the course of their business.

If User is the author of the Work, User may automatically have the right to reuse it under the rights granted back when User transferred the copyright in the article to the Rightsholder. User should check the copyright form and the relevant author rights policy to check whether permission is required. If User is the author of the Work and does require permission for proposed reuse of the Work, User should select ‘Author of requested content’ as the Requestor Type. The Rightsholder shall not reimburse any fees which User pays for a republication license.

If User is the author of the article which User wishes to reuse in User's thesis or dissertation, the republication licence covers the right to include the Accepted Manuscript

APPENDIX: B (continued)

version (not the Version of Record) of the article. User must include citation details and, for online use, a link to the Version of Record of the article on the Rightsholder's website. User may need to obtain separate permission for any third party content included within the article. User must check this with the copyright owner of such third party content. User may not include the article in a thesis or dissertation which is published by ProQuest. Any other commercial use of User's thesis or dissertation containing the article would also need to be expressly notified in writing to the Rightsholder at the time of request and would require separate written permission from the Rightsholder.

User does not need to request permission for Work which has been published under a CC BY licence. User must check the Version of Record of the CC BY article from which the Work is to be reused, to check whether any of the material in the Work is third party material and so not published under the CC BY licence. User is solely responsible for identifying and obtaining separate licences and permissions from the copyright owner for reuse of any such third party material/figures. The Rightsholder shall not reimburse any fees which User pays for such licences and permissions.

As well as CCC, the Rightsholder shall have the right to bring any legal action that it deems necessary to enforce its rights should it consider that the Work infringes those rights in any way.

For STM Signatories ONLY (as agreed as part of the STM Guidelines)

Any licence granted for a particular edition of a Work will apply also to subsequent editions of it and for editions in other languages, provided such editions are for the Work as a whole in situ and do not involve the separate exploitation of the permitted illustrations or excerpts.

Other Terms and Conditions:

STANDARD TERMS AND CONDITIONS

1. Description of Service; Defined Terms. This Republication License enables the User to obtain licenses for republication of one or more copyrighted works as described in detail on the relevant Order Confirmation (the "Work(s)"). Copyright Clearance Center, Inc. ("CCC") grants licenses through the Service on behalf of the rightsholder identified on the Order Confirmation (the "Rightsholder"). "Republication", as used herein, generally means the inclusion of a Work, in whole or in part, in a new work or works, also as described on the Order Confirmation. "User", as used herein, means the person or entity making such republication.
2. The terms set forth in the relevant Order Confirmation, and any terms set by the Rightsholder with respect to a particular Work, govern the terms of use of Works in connection with the Service. By using the Service, the person transacting for a republication license on behalf of the User represents and warrants that he/she/it (a) has been duly authorized by the User to accept, and hereby does accept, all such terms and conditions on behalf of User, and (b) shall inform User of all such terms and conditions. In the event such person is a "freelancer" or other third party independent of User and CCC, such party shall be deemed jointly a "User" for purposes of these terms and conditions. In any event, User shall be deemed to have accepted and agreed to all such terms and conditions if User republishes the Work in any fashion.
3. Scope of License; Limitations and Obligations.

APPENDIX: B (continued)

3.1 All Works and all rights therein, including copyright rights, remain the sole and exclusive property of the Rightsholder. The license created by the exchange of an Order Confirmation (and/or any invoice) and payment by User of the full amount set forth on that document includes only those rights expressly set forth in the Order Confirmation and in these terms and conditions, and conveys no other rights in the Work(s) to User. All rights not expressly granted are hereby reserved.

3.2 General Payment Terms: You may pay by credit card or through an account with us payable at the end of the month. If you and we agree that you may establish a standing account with CCC, then the following terms apply: Remit Payment to: Copyright Clearance Center, 29118 Network Place, Chicago, IL 60673-1291. Payments Due: Invoices are payable upon their delivery to you (or upon our notice to you that they are available to you for downloading). After 30 days, outstanding amounts will be subject to a service charge of 1 1/2% per month or, if less, the maximum rate allowed by applicable law. Unless otherwise specifically set forth in the Order Confirmation or in a separate written agreement signed by CCC, invoices are due and payable on "net 30" terms. While User may exercise the rights licensed immediately upon issuance of the Order Confirmation, the license is automatically revoked and is null and void, as if it had never been issued, if complete payment for the license is not received on a timely basis either from User directly or through a payment agent, such as a credit card company.

3.3 Unless otherwise provided in the Order Confirmation, any grant of rights to User (i) is "one-time" (including the editions and product family specified in the license), (ii) is nonexclusive and non-transferable and (iii) is subject to any and all limitations and restrictions (such as, but not limited to, limitations on duration of use or circulation) included in the Order Confirmation or invoice and/or in these terms and conditions. Upon completion of the licensed use, User shall either secure a new permission for further use of the Work(s) or immediately cease any new use of the Work(s) and shall render inaccessible (such as by deleting or by removing or severing links or other locators) any further copies of the Work (except for copies printed on paper in accordance with this license and still in User's stock at the end of such period).

3.4 In the event that the material for which a republication license is sought includes third party materials (such as photographs, illustrations, graphs, inserts and similar materials) which are identified in such material as having been used by permission, User is responsible for identifying, and seeking separate licenses (under this Service or otherwise) for, any of such third party materials; without a separate license, such third party materials may not be used.

3.5 Use of proper copyright notice for a Work is required as a condition of any license granted under the Service. Unless otherwise provided in the Order Confirmation, a proper copyright notice will read substantially as follows:

APPENDIX: B (continued)

4. “Republished with permission of [Rightsholder’s name], from [Work’s title, author, volume, edition number and year of copyright]; permission conveyed through Copyright Clearance Center, Inc. ” Such notice must be provided in a reasonably legible font size and must be placed either immediately adjacent to the Work as used (for example, as part of a by-line or footnote but not as a separate electronic link) or in the place where substantially all other credits or notices for the new work containing the republished Work are located. Failure to include the required notice results in loss to the Rightsholder and CCC, and the User shall be liable to pay liquidated damages for each such failure equal to twice the use fee specified in the Order Confirmation, in addition to the use fee itself and any other fees and charges specified.

4.1 User may only make alterations to the Work if and as expressly set forth in the OrderConfirmation. No Work may be used in any way that is defamatory, violates the rights of third parties (including such third parties' rights of copyright, privacy, publicity, or other tangible or intangible property), or is otherwise illegal, sexually explicit or obscene. In addition, User may not conjoin a Work with any other material that may result in damage to the reputation of the Rightsholder. User agrees to inform CCC if it becomes aware of any infringement of any rights in a Work and to cooperate with any reasonable request of CCC or the Rightsholder in connection therewith.

5. Indemnity. User hereby indemnifies and agrees to defend the Rightsholder and CCC, and their respective employees and directors, against all claims, liability, damages, costs and expenses, including legal fees and expenses, arising out of any use of a Work beyond the scope of the rights granted herein, or any use of a Work which has been altered in any unauthorized way by User, including claims of defamation or infringement of rights of copyright, publicity, privacy or other tangible or intangible property.

6. Limitation of Liability. UNDER NO CIRCUMSTANCES WILL CCC OR THE RIGHTSHOLDER BE LIABLE FOR ANY DIRECT, INDIRECT, CONSEQUENTIAL OR

INCIDENTAL DAMAGES (INCLUDING WITHOUT LIMITATION DAMAGES FOR LOSS OF BUSINESS PROFITS OR INFORMATION, OR FOR BUSINESS INTERRUPTION) ARISING OUT OF THE USE OR INABILITY TO USE A WORK, EVEN IF ONE OF THEM HAS BEEN ADVISED OF THE POSSIBILITY OF SUCH DAMAGES. In any event, the total liability of the Rightsholder and CCC (including their respective employees and directors) shall not exceed the total amount actually paid by User for this license. User assumes full liability for the actions and omissions of its principals, employees, agents, affiliates, successors and assigns.

7. Limited Warranties. THE WORK(S) AND RIGHT(S) ARE PROVIDED “AS IS”. CCC HAS THE RIGHT TO GRANT TO USER THE RIGHTS GRANTED IN THE ORDER CONFIRMATION DOCUMENT. CCC AND THE RIGHTSHOLDER DISCLAIM ALL OTHER WARRANTIES RELATING TO THE WORK(S) AND RIGHT(S), EITHER EXPRESS OR IMPLIED, INCLUDING WITHOUT LIMITATION IMPLIED WARRANTIES OF MERCHANTABILITY OR FITNESS FOR A PARTICULAR

APPENDIX: B (continued)

PURPOSE. ADDITIONAL RIGHTS MAY BE REQUIRED TO USE ILLUSTRATIONS, GRAPHS, PHOTOGRAPHS, ABSTRACTS, INSERTS OR OTHER PORTIONS OF THE

WORK (AS OPPOSED TO THE ENTIRE WORK) IN A MANNER CONTEMPLATED BY USER; USER UNDERSTANDS AND AGREES THAT NEITHER CCC NOR THE RIGHTSHOLDER MAY HAVE SUCH ADDITIONAL RIGHTS TO GRANT.

8. Effect of Breach. Any failure by User to pay any amount when due, or any use by User of a Work beyond the scope of the license set forth in the Order Confirmation and/or these terms and conditions, shall be a material breach of the license created by the Order Confirmation and these terms and conditions. Any breach not cured within 30 days of written notice thereof shall result in immediate termination of such license without further notice. Any unauthorized (but licensable) use of a Work that is terminated immediately upon notice thereof may be liquidated by payment of the Rightsholder's ordinary license price therefor; any unauthorized (and unlicensable) use that is not terminated immediately for any reason (including, for example, because materials containing the Work cannot reasonably be recalled) will be subject to all remedies available at law or in equity, but in no event to a payment of less than three times the Rightsholder's ordinary license price for the most closely analogous licensable use plus Rightsholder's and/or CCC's costs and expenses incurred in collecting such payment.

9. Miscellaneous.

9.1 User acknowledges that CCC may, from time to time, make changes or additions to the service or to these terms and conditions, and CCC reserves the right to send notice to the User by electronic mail or otherwise for the purposes of notifying User of such changes or additions; provided that any such changes or additions shall not apply to permissions already secured and paid for.

9.2 Use of User-related information collected through the Service is governed by CCC's privacy policy, available online here: <http://www.copyright.com/content/cc3/en/tools/footer/privacypolicy.html>.

9.3 The licensing transaction described in the Order Confirmation is personal to User. Therefore, User may not assign or transfer to any other person (whether a natural person or an organization of any kind) the license created by the Order Confirmation and these terms and conditions or any rights granted hereunder; provided, however, that User may assign such license in its entirety on written notice to CCC in the event of a transfer of all or substantially all of User's rights in the new material which includes the Work(s) licensed under this Service.

9.4 No amendment or waiver of any terms is binding unless set forth in writing and signed by the parties. The Rightsholder and CCC hereby object to any terms contained in any writing prepared by the User or its principals, employees, agents or affiliates and purporting to govern or otherwise relate to the licensing transaction described in the Order Confirmation, which terms are in any way inconsistent with any terms set forth in the Order Confirmation and/or in these terms and conditions or CCC's standard operating procedures, whether such writing is prepared prior to, simultaneously with or subsequent to the Order Confirmation, and whether such writing appears on a copy of the Order Confirmation or in a separate instrument.

APPENDIX: B (continued)

9.5 The licensing transaction described in the Order Confirmation document shall be governed by and construed under the law of the State of New York, USA, without regard to the principles thereof of conflicts of law. Any case, controversy, suit, action, or proceeding arising out of, in connection with, or related to such licensing transaction shall be brought, at CCC's sole discretion, in any federal or state court located in the County of New York, State of New York, USA, or in any federal or state court whose geographical jurisdiction covers the location of the Rightsholder set forth in the Order Confirmation. The parties expressly submit to the personal jurisdiction and venue of each such federal or state court. If you have any comments or questions about the Service or Copyright Clearance Center, please contact us at 978-750-8400 or send an e-mail to info@copyright.com. v 1.1

Questions? customer@copyright.com or +1-855-239-3415 (toll free in the US) or +1-978-646-2777.

VITA

NAME SOUVIK MUKHERJEE

EDUCATION PhD, University of Illinois at Chicago, Chicago, IL, USA, 2018
B.Tech, West Bengal University of Technology, Kolkata, India
2012

EXPERIENCE Research Assistant in Electrical and Computer Engineering
Department 2014-2018
Graduate Technical Research Aide, PhD in NE Division, Argonne
National Laboratory, Lemont, IL, USA.
May- Aug '16 & May-Aug '17
Teaching Assistant in Electrical and Computer Engineering
Department 2013-2014
Programmer Analyst Trainee at Cognizant Technology Solutions,
Kolkata, WB, India Apr-Aug '13
Summer Intern at Indian Institute of Technology, Roorkee,
Uttarakhand, India Jun-Jul '11

HONORS Graduate Student Presenter's Award, University of Illinois at
Chicago 2015
University Merit Scholarship, West Bengal University of
Technology 2012
National Merit Scholarship Award (Govt. of India) 2007

PUBLICATIONS **Journal Publications**
Mukherjee S, Sarkar K, Wiederrecht GP, Schaller RD, Gosztola DJ,
Stroschio MA, Dutta M. Defect induced structural inhomogeneity,
ultraviolet light emission and near-band-edge photoluminescence
broadening in degenerate In₂O₃ nanowires. Nanotechnology. 2018
Mar 1;29(17):17520.
Sarkar K, Mukherjee S, Wiederrecht G, Schaller R, Gosztola DJ,
Stroschio MA, Dutta M. Ultrafast carrier dynamics and optical

VITA (continued)

pumping of lasing from Ar-plasma treated ZnO nanoribbons. *Nanotechnology*. 2018 Jan 24;29(9): 095701

Datta D, Sarkar K, Mukherjee S, Meshik X, Stroschio MA, Dutta M. Graphene oxide and DNA aptamer based sub-nanomolar potassium detecting optical nanosensor. *Nanotechnology*. 2017 Jul 18;28(32):325502.

Sarkar K, Mukherjee S, Farid S, Nicholls A, Stroschio MA, Dutta M. Characterization of Co-existing In₂O₃-ZnO Nanostructures. *Journal of Electronic Materials*. 2017 Oct;46:5848-54.

Meshik X, Choi M, Baker A, Malchow RP, Covnot L, Doan S, Mukherjee S, Farid S, Dutta M, Stroschio MA. Modulation of voltage-gated conductances of retinal horizontal cells by UV-excited TiO₂ nanoparticles. *Nanomedicine: nanotechnology, biology, and medicine*. 2017 Apr;13(3):1031-40.

Datta D, Meshik X, Mukherjee S, Sarkar K, Choi MS, Mazouchi M, Farid S, Wang YY, Burke PJ, Dutta M, Stroschio MA. Submillimolar Detection of Adenosine Monophosphate Using Graphene-Based Electrochemical Aptasensor. *IEEE Transactions on Nanotechnology*. 2017 Mar;16(2):196-202.

Farid S, Mukherjee S, Sarkar K, Mazouchi M, Stroschio MA, Dutta M. Enhanced optical properties due to indium incorporation in zinc oxide nanowires. *Applied Physics Letters*. 2016 Jan 11;108(2):021106.

Mukherjee S, Meshik X, Choi M, Farid S, Datta D, Lan Y, Poduri S, Sarkar K, Baterdene U, Huang CE, Wang YY. A graphene and aptamer based liquid gated FET-like electrochemical biosensor to detect adenosine triphosphate. *IEEE transactions on nanobioscience*. 2015 Dec;14(8):967-72.

(Featured in the IEEE Engineering in Medicine and Biology Society (EMBS) as well as Transactions on NanoBioscience homepage)

Choi MS, Meshik X, Mukherjee S, Farid S, Doan S, Covnot L, Dutta M, Stroschio MA. Electrostatic force analysis, optical measurements, and structural characterization of zinc oxide colloidal quantum dots synthesized by sol-gel method. *Journal of Applied Physics*. 2015 Nov 21;118(19):194304.

VITA (continued)

Farid S, Meshik X, Choi M, Mukherjee S, Lan Y, Parikh D, Poduri S, Baterdene U, Huang CE, Wang YY, Burke P. Detection of Interferon gamma using graphene and aptamer based FET-like electrochemical biosensor. *Biosensors and Bioelectronics*. 2015 Sep 15;71:294-9.

Farid S, Mukherjee S, Jung H, Strosio MA, Dutta M. Analysis on the structural, vibrational and defect states of chlorine treated polycrystalline cadmium telluride structures grown by e-beam evaporation. *Materials Research Express*. 2015 Feb 5;2(2):025007.

Meshik X, Farid S, Choi M, Lan Y, Mukherjee S, Datta D, Dutta M, Strosio MA. Biomedical Applications of Quantum Dots, Nucleic Acid- Based Aptamers, and Nanostructures in Biosensors. *Critical Reviews™ in Biomedical Engineering*. 2015;43(4).

Karmakar R, Biswas A, Mukherjee S, Deyasi A. Calculating Transmission Coefficient of Double Quantum Well Triple Barrier Structure having Parabolic Geometry using Propagation Matrix Method. *International Journal of Engineering and Advanced Technology (IJEAT) ISSN*. 2011:2249-8958.

Mukherjee S, Karmakar R, Deyasi A. Theoretical computation of transmission coefficient of double quantum well triple barrier structure in presence of electric field. *International Journal of Soft Computing and Engineering*. 2011;1:41-4.

Mukherjee S, Sarkar K, Wiederrecht GP, Gosztola DJ, Strosio MA, Dutta M. Influence of surface states and passivation treatment on the carrier dynamics of In₂O₃ nanowires, *under preparation*.

Mukherjee S, Sarkar K, Wiederrecht GP, Gosztola DJ, Strosio MA, Dutta M. Morphology dependent carrier dynamics in In₂O₃ nanostructures, *under preparation*.

Mukherjee S, Sarkar K, Elmer TW, Bakhtiari S, Gopalsami N, Koehl ER, Strosio MA, Dutta M. Stand-off detection of ¹³⁷Cs γ -radiation using In₂O₃ nanowires based on a millimeter wave technique, *under preparation*.

Mukherjee S, Elmer TW, Bakhtiari S, Gopalsami N, Koehl ER, Strosio MA, Dutta M. Design and operation of an ultrafast and compact chirped-pulse Fourier transform millimeter wave

VITA (continued)

spectrometer operating in the 110-140 GHz range for real-time chemical analysis, *under preparation*.

Conference Publications:

Heifetz A, Bakhtiari S, Gopalsami N, Elmer TW, Mukherjee S. Long-range monostatic remote sensing of geomaterial structure weak vibrations. AIP Conference Proceedings, 1949(1):030004, Apr 2018.

Stroscio MA, Dutta M, Meshik X, Farid S, Lan Yi, Mukherjee S, Choi M, Bat-Erdene U, Parikh D, Ranginwala S, Datta D, Xu K, Pratap P, Wu TC. Nanotechnology-based Tools for the Study of the Affinity and Selectivity of Antigens for Small Molecular Targets Underlying Drug Discovery and Therapeutics. Drug Discovery and Therapy World Congress, p. 119, July 22-25, 2015.

Mukherjee S, Farid S, Sarkar K, Stroscio MA, Dutta M. Synthesis, characterization and application of oxide semiconductor nanowires as nuclear radiation sensors. APS/CNM Users Meeting, Argonne National Laboratory, May 2016.

Mukherjee S, Farid S, Stroscio MA, Dutta M. Modeling polycrystalline effects on the device characteristics of cdte based solar cells. In Computational Electronics (IWCE), 2015 International Workshop on 2015 Sep 2 (pp. 1-4). IEEE.

Mukherjee S, Karmakar R, Deyasi A. Nonparabolicity Effect on Transmission Coefficient of Double Quantum Well Triple Barrier Structure under Electric Field, International Conference on Theoretical and Applied Physics, Indian Institute of Technology Kharagpur, p. 70, Dec 2011.

Karmakar R, Mukherjee S, Deyasi A. Numerical Analysis of Transmission Coefficient of Double Quantum Well Triple Barrier Structure for Variable Effective Mass using Transfer Matrix. IEEE EDS Student Paper Conference, Jadavpur University, pp. 66-70, Apr 2011.